Cost Optimization and Liquid-Air Interface Stability Analysis of a Liquid Piston Compressor/Expander

A THESIS
SUBMITTED TO THE FACULTY OF
UNIVERSITY OF MINNESOTA
BY

Aleksander Gust

IN PARTIAL FULFILLMENT OF THE REQUIREMENTS
FOR THE DEGREE OF
MASTER OF SCIENCE

Advisor: James Van de Ven
Co-advisor: Perry Y. Li

May 2020

Acknowledgements

I would like to thank NSF (grant PFI-TT #1827517) for funding this project, the MEPS lab for providing the proper facilities for experimentation, and the University of Minnesota campus for providing an encouraging atmosphere for thoughtful and determined innovation.

My experience in the Master's program in the UMN Mechanical Engineering Department was full of learning opportunities and helpful guidance. I especially would like to thank Prof. James Van de Ven for all of the wonderful guidance, caring support, and shared knowledge that helped make my tenure at the University of Minnesota an immensely positive experience.

I would also like to thank Prof. Perry Li and Prof. Terrence Simon for sharing their expert knowledge and experience. I have gained much insight into how successful engineers think critically and seek solutions by engaging in thoughtful discussion with them during our team meetings. The constructive feedback received has taught me the importance of maintaining attention to detail and perseverance.

The comradery shared with the other students in the Mechanical Energy and Power Systems (MEPS) lab and Fluid Power Research (FPR) lab has played a large role in providing an engaging and helpful academic environment. I would also like to acknowledge my project partner Brian Carrier for his excellent contributions and collaboration. Lastly, I would like to thank my parents for their continued love and support and my brother Christian for always encouraging me to better myself.

Dedication

I dedicate this thesis to my loving family who provided unwavering support and encouragement throughout my academic career.

Abstract

The present research focuses on the optimal cost driven design and liquid-air interfacial stability analysis of a Compressed Air Energy Storage (CAES) system. CAES technology can be paired with renewable energy harvesting devices in order to overcome the mismatch between power availability and power demanded by the electrical grid. The proposed novel approach to CAES utilizes a liquid piston to compress air during periods of excess power availability to be stored for later use. As liquid (water) is pumped into the compression chamber, the air is compressed as the liquid-air interface rises. Using liquid as the compression piston allows for heat transfer media to be distributed throughout the compression chamber to facilitate greater heat transfer.

Heat transfer is fundamentally important to the compression/expansion efficiency of the CAES system. As the air is compressed, the internal energy of the air will rise resulting in a rise in temperature. If the air is stored in this state, the air will eventually cool to ambient temperatures and this energy will be lost. It is therefore paramount to minimize the rise in air temperature during compression. A near isothermal compression/expansion can be accomplished through high amounts of heat transfer during the process. Many increases in heat transfer capability can be realized through the use of a liquid piston as the means to compress/expand air due to the liquids ability to flow through a tortuous path of heat exchanger material. The high thermal efficiencies achievable by this CAES system design make commercialization viable if the overall system cost can be reduced.

A relationship between system performance and cost has been developed with the goal to find the optimal system parameters that yield the minimal cost per power of the system. System parameters include compression trajectory, compression chamber shape, and heat transfer media distribution, which define system performance through a one-dimensional model of the air compression. These same parameters are also used to calculate the cost of the system which includes both the hydraulic pump cost (determined by compression trajectory) and compression/expansion chamber cost. Furthermore, a flow intensifier concept was introduced to further reduce hydraulic pump size/cost by

amplifying the available flow. A comparison is then made between the previous power density optimized design and the cost optimized design presented in this research. The addition of the flow intensifier resulted in a cost reduction of 75% while increasing power density by 234% when comparing the cost optimal flow intensifier design to the previous power density optimized design.

Using a liquid piston for air compression offers many benefits in terms of heat transfer, but raises concerns pertaining to the stability of the liquid-air interface. Interfacial instability results in undesirable mixing of the liquid and air, which results in wasted effort as the air is compressed, yet is unable to be ejected out of the chamber into the storage vessel. Due to the cross-plate heat exchanger design, the torturous path the liquid flows through creates many flow boundaries that can lead to instabilities in the interface. To determine how the cross-plate heat exchanger geometry disrupts the interface, a simplified 2-D CFD model of the liquid interface was developed utilizing a Marker and Cell (MAC) approach. The research presented shows a relationship between cross-plate separation distances, liquid piston operation frequencies, and the resulting maximum wave amplitude of the liquid-air interface. Experimentation was completed using highspeed footage and edge tracking software to experimentally validate the model.

Table of Contents

List of Tables

List of Figures

Nomenclature

P_0	initial air pressure	[Pa]
P	air pressure	[Pa]
V_0	initial air volume	$[m^3]$
V	air volume	$[m^3]$
W_{in}	input work for compression	[J]
t_c	compression time	[sec]
W_f	friction power	[J/sec]
r	compression ratio	-
E_{st}	stored energy	[J]
η_c	compression efficiency	-
PD_c	power density for compression	$[W/m^3]$
$V_{chamber}$	volume of compression chamber	$[m^3]$
HT	heat transfer rate	[j/sec]
E_{tot}	total internal energy of air	[J]
T	gas temperature	[K]
m	air mass	[Kg]
e	specific energy of air	[J/Kg]
ρ	air density	$[Kg/m^3]$
h	heat transfer coefficient	$[W/m^2K]$
Nu	Nusselt number	-
D_H	hydraulic diameter	[m]
k	thermal conductivity of air	$[W/m \cdot K]$
Re	Reynold's number	-
Pr	Prandtl number	-
u	Darcian air velocity	[m/sec]
Φ	chamber cross sectional area	$[m^2]$
T_s	heat transfer material temperature	[K]
Q	liquid piston flow rate	$[m^3/sec]$

Ω	heat transfer area density	$[m^2/m^3]$
Λ	effective chamber cross sectional area	$[m^2]$
Ψ	porosity	-
$\overline{\Upsilon}$	maximum allowable porosity	-
η^*	desired compression efficiency	-
l_{min}	minimum chamber length	[m]
l_{max}	maximum chamber length	[m]
J	system cost per power	[$/W]
S_V	chamber cost density	$[\$/m^3]$
S_Q	pump cost per maximum flowrate	$[\$/(m^3/sec)]$
σ_1	hoop stress of chamber	[Pa]
σ_2	axial stress of chamber	[Pa]
σ_y	yield stress	[Pa]
t	chamber wall thickness	[m]
r_c	chamber radius	[m]
h_c	chamber height	[m]
A_{FI}	flow intensifier cross sectional area	$[m^2]$
γ	flow intensifier area ratio	-
P_{switch}	switching pressure of flow intensifier	[Pa]
ν	kinematic viscosity	$[m^2/sec]$
r_{cr}	crank radius	[m]
l_{cr}	connecting rod length	[m]
σ_w	surface tension of water	[N/m]
ω	angular frequency	[rad/sec]

1. Introduction

1.1 Renewable Energy Storage Background

The demand for energy in the United States has been steadily increasing over the past half a century. During this time, the majority of U.S. energy consumption relied most heavily on petroleum, natural gas and coal (see Figure 1.1). These energy sources are non-renewable and produce atmospheric warming “greenhouse” gas emissions. Greenhouse gas pollution has aided in the development of climate change, which manifests itself in the form of decimating wildfires, powerful tornadoes, and persistent droughts. The U.S. is a large contributor of global warming emissions. Of the total U.S. emissions, those produced by gas-fired and coal-fired electricity plants accumulate to about 28% [1]. In an effort to confront this global problem, most world leaders are developing initiatives to reduce their carbon footprint. One initiative is to place a tax on how much greenhouse gases are being produced. Increasing the carbon tax will add cost to the production of electricity that requires the burning of non-renewable fuels. Since electricity produced in this way is relatively inexpensive, compared to electricity produced from renewable sources, the carbon tax will act to even out the market cost, allowing renewable energy to compete in the market. Achieving a competitive market is beneficial, as it will drive innovation within the renewable energy marketplace while producing more efficient and cost effective system designs. Reducing the barrier to entry for the employment of renewable energy sources will increase their share of the total U.S. energy consumption, which, in turn, reduces the harmful carbon footprint [2].

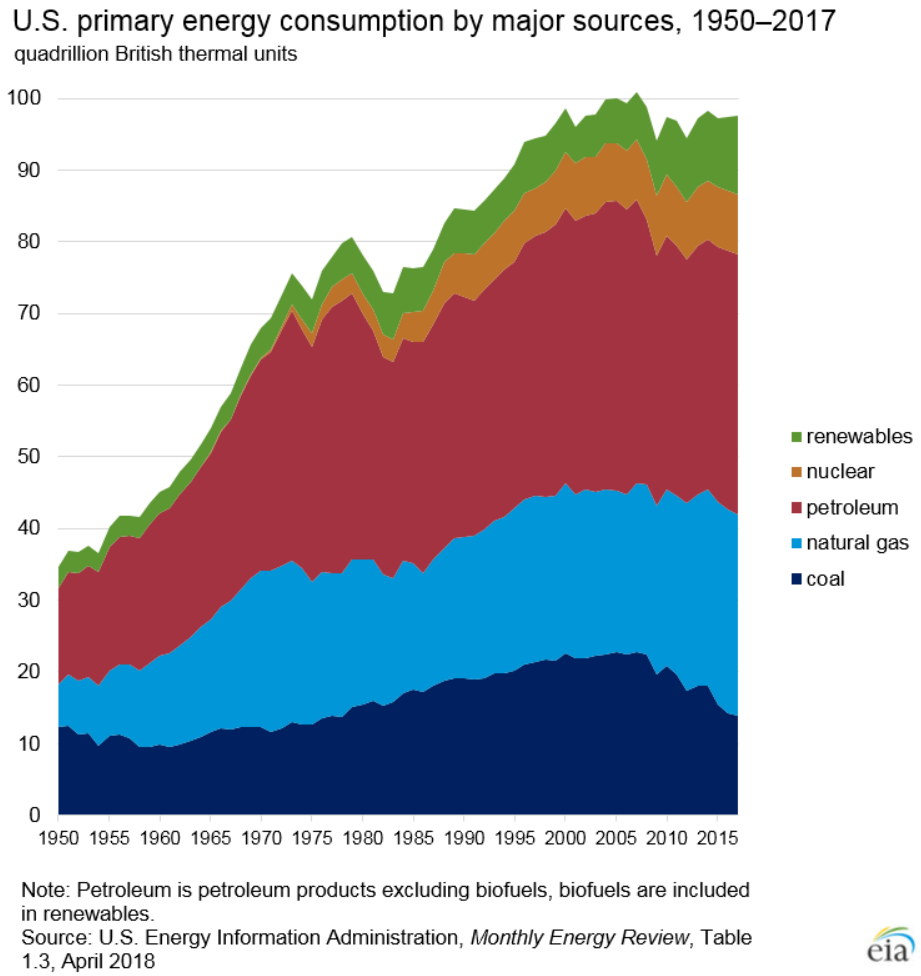

Figure 1.1: United States energy consumption by major sources (1950-2015). (Source: U.S. Energy Information Administration)

However, in order to close this cost gap, many technical challenges must be overcome to integrate an increasing number of renewable energy sources into the electrical grid. Renewable energy sources are often intermittent and unpredictable, making their integration into the electric grid difficult. For example, the sun shines for a set time interval during the day, with cloud interruptions, and with most intensity during the summer season (intermittent). The intensity of wind can vary by the hour, making prediction of available wind energy at any given time difficult. In contrast, fossil fuels inherently reside in a near perfect state of stored energy. This natural state of energy storage is relatively safe, portable, and can be converted to electricity at any time through

chemical reaction. Herein lies the main challenge with the integration of renewable energy sources. Often times, their intermittency and unpredictability make the conversion process to electricity not coincide with the demand for power. Therefore, there tends to be either an abundance or scarcity of available energy to be converted to electricity. The peak power demand occurs in the evening (typically around 5-8PM), whereas daily available solar energy occurs throughout mid-day (maximum intensity occurs at noon). The wind blows most heavy during the night, when the average consumer is asleep and the power demand is at its lowest. This relationship between available renewable power sources and power demand can be seen in Figure 1.2.

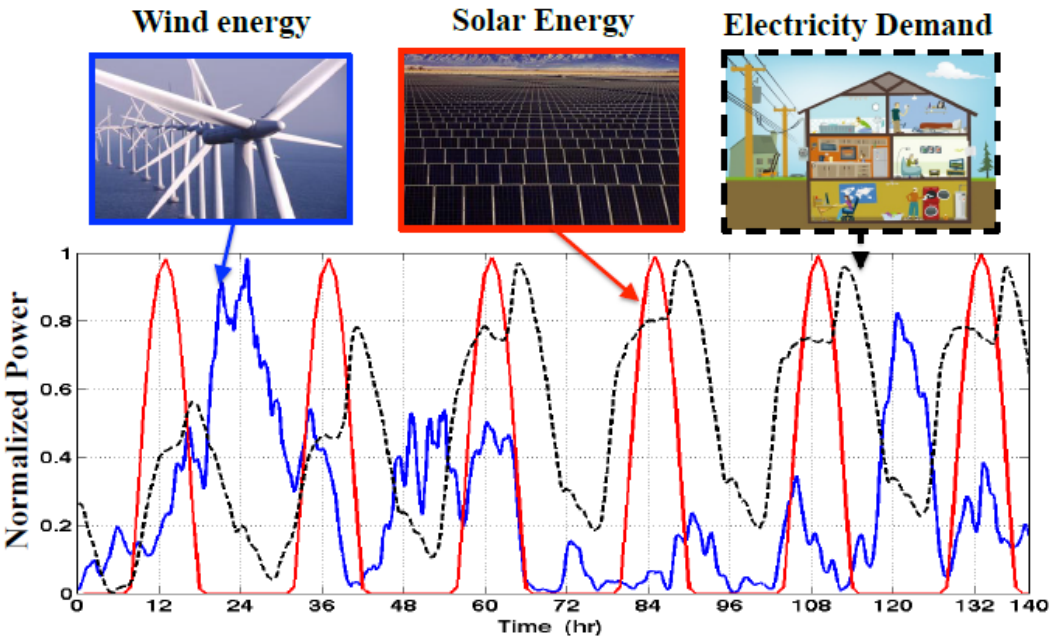

Figure 1.2: Normalized power demand in contrast to available wind and solar power supplies [9]

Energy production and consumption must be in balance in order for the electric grid to be stable. Both of these vary significantly in time and in the event of a mismatch, gas-fired peaker plants make up the difference in energy production. These peaker plants are expensive to manufacture and burn fossil fuels, which is counterproductive to

reducing emissions. In order to omit the use of peaker plants, alternate approaches to gather and store renewable energy when the supply exceeds the demand are being introduced. Stored energy can then be regenerated when demand exceeds supply, thus removing the need for fossil fuels while utilizing more of the available renewable energy resources [3]. These benefits have drawn significant attention to cost effective, large-scale energy storage technologies. Investigations into which energy storage technologies are the appropriate fits to mitigate fluctuations in wind energy are explored in [4]. Among the various methods of energy storage technologies, pumped-hydro, battery, and compressed air energy storage systems have promises of higher installed capacity.

Of all these storage methods, pumped hydro is the largest and most mature storage method available today. When power demand is low, water is pumped from a low elevation reservoir to a higher elevation reservoir. The energy captured is stored as gravitational potential energy in the elevated water. During regeneration, the water is allowed to descend in elevation. Essentially, the high elevation reservoir acts like a dammed river for hydroelectric power generation [14[15]. Since this technology relies on the volume of water displaced, the power density of this system is not very high (10J/lit per meter of elevation). Therefore, in order to store much energy, a large volume of water must be displaced to a higher elevation. This leads to this technology being dependent on geological sites in order to be a viable large-scale energy storage system. These systems offer between 70% and 85% round trip efficiency, but their confinement to specific geological locations or expensive human-made reservoirs is a hindrance.

An alternative technology is Compressed Air Energy Storage (CAES). An example, seen in Figure 1.3 is the conventional approach to a CAES system which also achieves large scale energy storage capability. These systems rely on large underground salt caverns that provide sealed chambers to store pressurized air. The pressurized air is then used to burn pre-compressed natural gas at surface level to regenerate the stored energy [5[6]. The caverns usually cannot support storing air at high pressures and are also lower limited to around 0.5 MPa providing a constrained pressurization range [*[5*]; therefore, these systems have relatively low energy capacity. Additionally, as the air inside the chamber is used for power regeneration, the pressure inside the cavern reduces

with use. This causes the power density to decrease as stored energy is depleted from the cavern. Plant capacities for conventional CAES systems are typically within the region of 50 MW to 300 MW in size. Conventional CAES systems suffer from many drawbacks including the requirement of a combustion engine with fuel, additional steps (combustion) in the energy conversion process, and the inefficiency of the compression cycle (~50%). Furthermore, this system also relies on particular geographical locations in order to produce large scale energy storage. Even with all of these disadvantages, CAES still remains one of the cheapest forms of energy storage and a good candidate for potential commercialization. Improvements made to the traditional CAES system in the form of air compression/expansion efficiency improvements, higher power density storage capabilities, and disassociation of required geological locations would potentially push CAES to the forefront of renewable energy storage solutions.

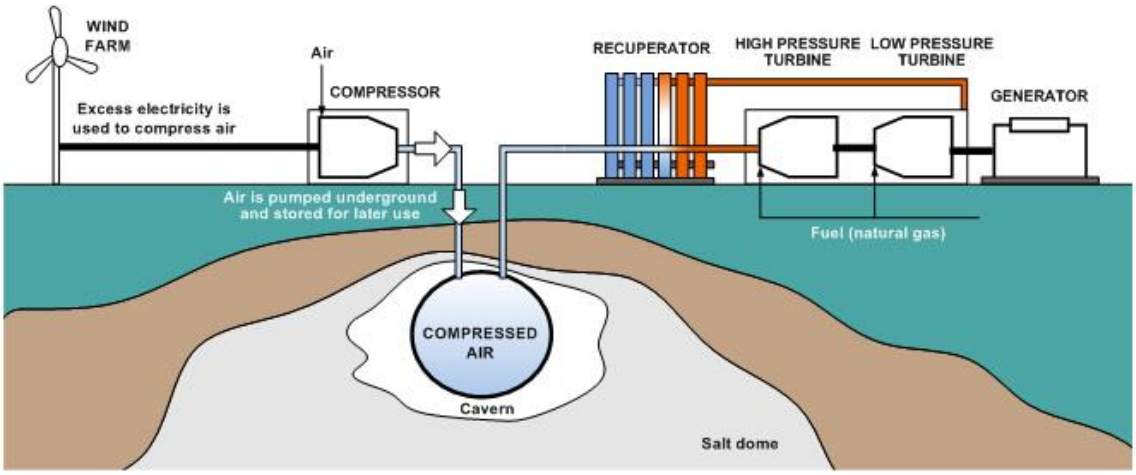

Figure 1.3: Conventional CAES system utilizing underground cavern for compressed air storage to be used with a natural gas power plant.

1.2 Literature Review

Previous research relevant to the work conducted under this thesis is summarized in this section. This information includes general gas compression/expansion processes, the history of liquid piston gas compression/expansion and its applications, augmentation of heat transfer during the liquid piston compression/expansion process, and liquid-air interface stability.

A given process of compressing or expanding a volume of gas can be bounded by the two extremes of an isothermal process or an adiabatic process. An isothermal process occurs when the temperature of the gas remains constant during the entire compression/expansion process [17]. Isothermal processes are achieved when the rate at which heat is generated within the gas during the process is equal to the rate at which heat is transferred out of the gas. An adiabatic process occurs when the gas is compressed so quickly that no heat transfer can occur during the process, producing a large increase in gas temperature. The adiabatic process produces a compressed volume of gas that contains a high amount of internal energy. When the gas is stored in this state, the gas will eventually cool to ambient temperature and the amount of stored energy in the gas will decrease [18]. This process causes a reduction in thermal efficiency, whereas a completely isothermal process will yield the highest efficiency possible. A large amount of prior research on the topic of gas compression has targeted internal combustion engines as the platform of study. Empirical heat transfer correlations based on bulk flow variables within the cylinder were characterized by the Hohenberg equation in early studies [19]. As more computationally heavy methods such as CFD became prominent in recent years, analysis was conducted to calculate heat transfer coefficients of a four-stroke engine and compared with experimentally obtain data [20]. As model complexity increased, further studies incorporating droplet spray combustion coupled with heat conduction through the engine wall were completed in [21]. Furthermore, investigation of the entire compression and expansion cycle of a gas spring following a sinusoidal trajectory using the CFD code ANSYS CFX was completed in [22]. The foundation of literature for gas compression/expansion is extensive in the area of internal combustion engine applications. This prior research is built upon by extending the application to compression/expansion processes using a liquid piston approach.

The liquid piston compression process, used in the present study, was first employed by Herbert Humphrey [23]. The Humphrey pump operated by introducing a combustion mixture into a cylinder inside which a water column resided. The combustion mixture was then compressed and ignited, building pressure inside the cylinder and forcing the water downward. When the pressure inside the chamber dropped to below the

atmospheric pressure, a water valve would open introducing more liquid into the cylinder. The returning water would force the exhaust gas out of the cylinder to prepare for combustible gas intake. The process was then repeated after combustible gas was compressed and ignited. This early pump achieved 10% efficiency and flow rate of 24 cubic meters per hour. The concept of using liquid as a piston for gas compression/expansion as opposed to a mechanical piston was further explored in [11]. This study found that utilizing a liquid piston for gas compression would provide many benefits which result in increased efficiency. The liquid piston compressor operates by using a hydraulic pump to fill a chamber with liquid from the bottom. The rising liquid-air interface then compresses the gas above it. Since liquid can conform to irregular chamber shapes, the surface area to volume ratio in the gas chamber can be increased which improves heat transfer. Additional surface area can be introduced to the gas by the introduction of a porous medium inside the compression chamber, through which the liquid can flow around unobstructed. Additionally, a liquid piston eliminates gas leakage and replaces sliding seal friction with viscous friction, greatly improving volumetric and mechanical efficiency. In contrast, a mechanical piston must have its sealing surfaces in contact with the chamber walls during the entire compression process and cannot be physically obstructed, thus limiting the available geometries of the chamber. It has been shown that liquid piston compressors have an advantage over traditional mechanical piston compressors in terms of efficiency and work consumption of the pump [11].

Applications of the liquid piston compressor/expander are abundant as this technology produces an efficient way to compress or expand gas. However, the introduction of an open accumulator concept [10] enabled the development of a novel CAES design. Accumulators are generally used in fluid power applications as a means to store energy through the compression of gas. Conventional accumulators operate by allowing fluid volume to enter the single inlet/outlet valve when the system pressure is above a certain charge pressure on the accumulator. For a bladder accumulator, the charge pressure is the pressure level of a bladder of gas inside the accumulator. Once the system pressure surpasses the charge pressure, the bladder of gas will compress, allowing the volume previously occupied by the bladder to instead be filled by the system fluid.

However, as the bladder compresses, the pressure inside the bladder builds, thus increasing the system pressure necessary to continue filling the accumulator with fluid. There are various conventional accumulator designs (such as a spring accumulator), but all of the conventional accumulators change pressure levels depending on the amount of stored energy they contain. The energy density of the conventional gas accumulator is restricted by the volume of the expanded gas within. An open accumulator architecture uses two inlet/outlet ports to instead keep the pressure level the same regardless of the stored energy contained. Exhausting the expanded air as the energy level of the accumulator depletes allows the open accumulator to not have to hold the large expanded gas volume. This is accomplished by depleting the volume of charge fluid as the accumulator fills with system fluid, thus keeping the pressure inside the accumulator constant. For the CAES application, allowing the stored gas to remain at peak pressure while the gas is entering/leaving the accumulator during compression/expansion cycles results in an improved energy density by an order of magnitude [10].

A key component to any CAES system is the air compressor/expander. In order to quantify the performance of a compressor/expander design, accurate modeling of the compressing/expanding gas is required. For a compression/expansion process, the gas experiences rapid changes in density, temperature, and pressure all of which affect the heat transfer. Early heat transfer studies focused on analytically solving a boundary layer flow. One such study calculated heat transfer by analytically solving a boundary layer flow of a compression produced by the pulse movement of a piston and showed good agreement with experiments [24[25]. A sinusoidal compression trajectory found similar agreement with an analytical solution [26]. However, when the same boundary layer analysis was conducted on shock waves produced by the piston, a discrepancy between experiments and analytical results was observed [27]. The present study focuses on compression/expansion processes that utilize a liquid piston approach. This type of compression can be simulated using multiphase flow modeling techniques. Two of these approaches using the Eulerian multiphase flow technique study a Volume of Fluid (VOF) model [28] and a mixture model [29]. These two models use volume fraction variables to

spatially represent different fluid phases numerically, and solve the energy and momentum equations for the flow mixture based on average properties.

A main benefit of using the liquid piston approach for gas compression/expansion is the ability to augment heat transfer by placing a porous media inside the compression/expansion chamber. The addition of a porous media allows for increased heat transfer capabilities due to an increase in surface area within the chamber. Previous studies have performed CFD experiments on various porous media inserts in order to calculate variations in local heat transfer coefficients and were shown to have good agreement with experiments [12]. Further CFD experiments were conducted on an interrupted plate heat exchanger geometry to quantify pressure drop across the material as well as heat transfer capabilities. This was accomplished using a representative elementary volume (REV) representing a unit cell of the heat exchanger. Twenty-seven heat exchanger geometries were produced via rapid prototyping and tested experimentally to show good agreement with the model [31]. A one-dimensional model used to calculate transient temperature distributions was developed and used to optimize the distribution of porous material within the chamber in order to maximize heat transfer. The one-dimensional model was verified against full CFD two-dimensional models of the same problem, good agreement was found [32].

Other methods of increasing heat transfer during the compression/expansion process besides using solid heat exchanger material were also investigated. One study simulated a liquid droplet spray injected into the compression/expansion chamber during operation to augment heat transfer. The simulation used a three stage compression process with compression ratios of 10:1, 7:1, and 5:1 in succession. Simulations showed an overall three stage compression efficiency of 89%, greatly improving upon the 27% efficient adiabatic compression of the same ratio [52]. This led to the investigation of how moisture content in the air affects the compression/expansion efficiency. A study developed a 0-D and 1-D thermodynamic model which takes into account the water evaporation/condensation and water droplets assuming equilibrium phase change. It was found that moisture content minimally improves system power density at high cycle efficiencies while more significant power density improvements are seen at low cycle

efficiencies [51]. Additional media inserts inside the compression chamber were tested in [58], including copper mini-tubes and aluminum mesh. This study found agreement with the proposed thermodynamic model with respect to the aluminum mesh, however large temperature variations within the copper mini-tubes were not adequately represented in the averaged model. However, experiments utilizing the copper mini-tube inserts found a thermal efficiency improvement of 30% during air compression experiments. High pressure (210 bar) air compression/expansion experiments were conducted in [59], across a wide range of compression/expansion times with a uniform distribution of porous media inside the compression chamber. This study found that as power density increases, efficiency decreases. However, at 90% efficiency, the power density of compression can be increased by a factor of 10 with the addition of the porous media. A North Carolina State University experimental study of liquid piston air compression introduced an aqueous foam into the compression chamber to augment heat transfer. It was found that a compression chamber completely full of aqueous foam produced a compression efficiency improvement of 4-8% in laboratory experiments [55]

Efficiency and power density are important traits of an effective CAES system. To increase the performance of the CAES system, one study investigated optimal compression trajectories [30]. This study found that at a compression efficiency of 90%, power gains in the range of 500%-1500% were achievable over ad hoc linear and sinusoidal profiles. Further efforts explored optimizing the shape of the chamber, porosity distribution of heat transfer material and finding the optimal compression trajectory for the proposed CAES system [9]. A lumped parameter heat transfer model was developed to incorporate porosity distribution, chamber cross sectional area, and compression trajectory to maximize the power density of the compression chamber. A dynamic programming approach was utilized to calculate the optimal compression trajectory while simultaneous optimization of chamber shape and porosity distribution was achieved for a given desired thermal efficiency. The optimal compression trajectory was experimentally validated on a low pressure system [9] as well as a high pressure system [57].

When using a liquid piston, the stability of the liquid-gas interface becomes important as instabilities of the two fluids can cause undesirable mixing. Mixing is undesirable as it entrains gas inside of the liquid when compressing, which allows the gas to be compressed but not ejected into the accumulator as usable compressed gas. A surface is created when two fluids of different densities form two separate volumes. This paper focuses on water and air as the two fluids, therefore the more dense water will reside in the bottom portion of the chamber while the less dense air remains on top of the water. The interface is stable when the coherent structure of the interface does not change during accelerations of the fluids. Fluid interface stability is a deeply researched topic. Early investigations of this topic were performed by Taylor and Lewis [33[34] after which researches defined criteria for interface stability. Taylor noted that when a fluid interface is accelerated perpendicular to the interface, the surface stability depends on the densities of the two fluids and the acceleration. It was discovered through mathematical analysis that if the acceleration of the denser fluid is greater than that of gravity, the interface would become unstable. Valha and Kubie [35] conducted experiments to determine how interface stability was affected by oscillating accelerations. At lower operating frequencies the interface remained stable, however as the frequency increased the interface became unstable. The instability was determined to be caused by air bubbles penetrating the liquid and by liquid drops ejecting into the air. The interface stability was most affected when the more dense fluid is decelerated (i.e. the denser fluid is moving upward and then reduces velocity) at a rate greater than that of gravity. CFD was conducted on the liquid piston compressor design and found stability problems to arise when the fluid interface acceleration was greater than 0.5g [45].

1.3 Motivation of Thesis

Conventional CAES systems use excess electricity produced to drive an air compressor to compress and store air in underground salt caverns. The stored energy is retrieved by using the pre-compressed air to improve the efficiency of natural gas combustion in a gas-fired turbine [5[6]. This process reintroduces the use of hydrocarbon

fuel, depends on geological salt caverns (restricted geologically), and results in a relatively low efficiency (<< 55%). An alternative novel approach for a CAES system utilizing wind energy is introduced in [7]. This approach compressed the air to a high pressure (200-350 bar), increasing the compression ratio and power density. For example, storing 170MJ of energy with pumped hydro requires 170m^3 of water at 100m of elevation whereas compressing air at a compression ratio of 350 can store the same amount of energy in only 1m^3 of volume. Furthermore, if the air is compressed/expanded nearly isothermally, a very good efficiency (>90%) is feasible. This is much more efficient than the conventional CAES system where the average efficiency is about 55% [8]. The near isothermal CAES system is the focus of this thesis. The CAES approach has numerous benefits despite its current limitations, and has received significant consideration for industrial scale energy storage. Some of these benefits include:

1. **Relatively High Energy Density:** When comparing CAES to pumped hydro, one sees that a CAES system storing ~3MW×8hr of energy in compressed air at 350 bar would require ~$500m^3$ of air volume. Storing the same energy in a pumped hydro system would require ~$144{,}000m^3$ of water at an elevation of $100m$ [56].
2. **No Toxic Chemicals:** Compressing and storing air does not require the use of hydrocarbon fuels or dangerous chemical batteries. The use of dangerous and difficult to recycle chemicals is a significant problem for the future of battery storage systems.
3. **Economically Scalable:** The energy capacity scales well with storage vessel volume and cost.

These benefits attribute to the viability of commercialization of CAES on the industrial scale. However, currently, CAES are limited to only 2% of the total U.S. energy storage capacity and all existing CAES systems are of the conventional architecture. Pumped hydro is by far the most implemented energy storage system, making up 95%, while the remainder is made up of thermal storage (2%) and electromechanical energy storage (1%)

[16]. There is expectation, however, for increased use of CAES in systems that do not rely on caverns for storage. Though all of the energy storage systems mentioned can be used for the wind energy market, the more appealing energy storage system for wind farm owners would obtain the following attributes:

1. **Capturing More Power from Wind:** Decoupling the power generation (from the wind turbine) and power demand (from the generator) would make the system able to capture as much energy from the wind as can be generated, no matter how much power is demanded from the electric generator. This is achieved by allowing the turbine to maintain the optimal tip speed for maximum power capture while the shaft turning the electric generator can maintain the speed necessary to accommodate the power demand. An added possible benefit of the CAES feature allows locating some components (such as the hydraulic pump) at the base of the wind turbine tower instead of up in the nacelle. This reduces installation and maintenance costs, especially in offshore wind turbines.
2. **Ramp Rate:** Primary sources of power generation, such as coal and nuclear, usually do not facilitate a fast response to a rapid change in power demand due to their energy conversion processes. The ability to both capture rapid increases in available wind energy and to quickly extract large amounts of power from stored energy would offer a pronounced advantage toward regulating power demand fluctuations. A quick-response energy storage system (such as the CAES system to be discussed) can help balance the power demand and supplement the primary sources of power when the need arises.
3. **No Power Converting System:** Allowing the wind turbine shaft and the generator shaft to spin independently of one another can provide the opportunity to remove the complicated electric power conversion unit. The energy in the storage vessel can provide the generator with the voltage and frequency demanded by the electric grid.

Figure 1.4 shows the novel CAES system approach. Wind energy is captured by the turbine (A) which drives a variable-displacement pump (B) located in the wind turbine nacelle. At the base of the wind turbine tower, a variable displacement pump/motor (C) is connected to a nearly-isothermal liquid piston compressor/expander (F), and a fixed-speed induction generator (G) in tandem on a common shaft. The pump (B) supplies power that then communicates with the storage vessel (E) by means of the compressor/expander (F). An open accumulator, the architecture of which is described in [10], allows the stored compressed air to remain at a constant pressure regardless of the level of the air/water interface position in the storage vessel. This storage method allows energy to either be stored in, or extracted from, (E) through hydraulic means (as in a conventional hydraulic accumulator) or pneumatic means (as a conventional air receiver). Whichever energy extraction method is chosen, the energy is stored in the compressed air.

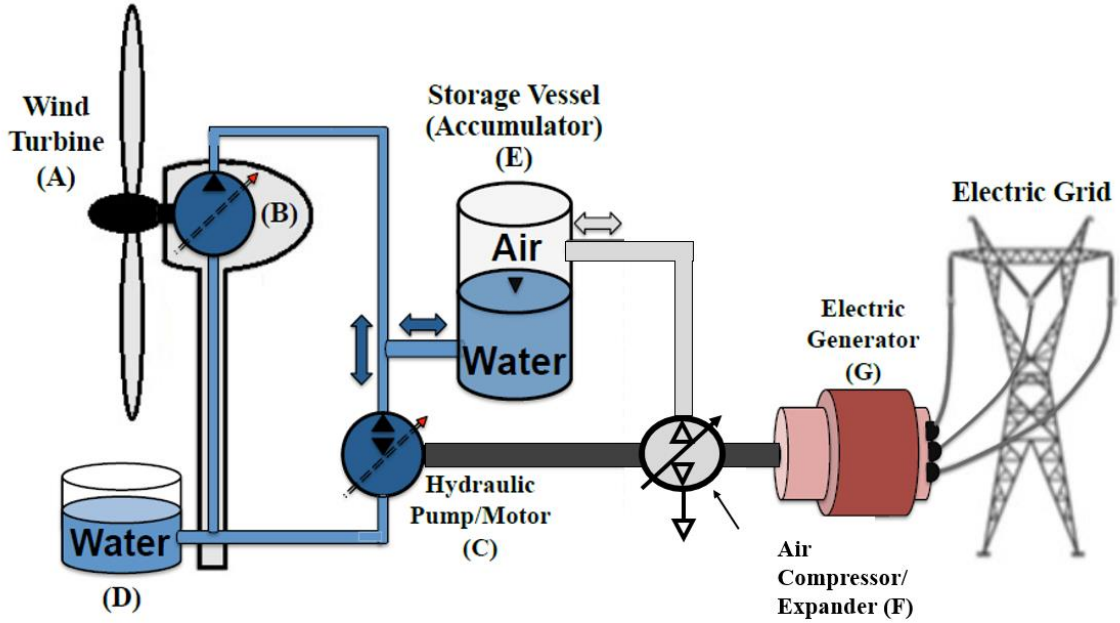

Figure 1.4: Novel CAES using near isothermal liquid piston compressor and open accumulator architecture for compressed air storage [57].

Traditional air compressor designs have relied on multiple compression stages with intercooling between each stage in order to reach high final pressures with

reasonable temperatures. Increasing the number of intermediate compression stages increases the overall heat transfer of the process, therefore increasing efficiency. However, each individual compression stage increases the overall volume of the compression system, affecting the power density. Therefore, adding more intermediate compression stages increases cycle efficiency while at the expense of power density [36]. For a given number of compression stages, the maximum power density of the entire process was found to occur when each stage was at the same compression ratio [37]. To further increase cycle efficiency, the compression cycle will be split into two stages (see Figure 1.5).

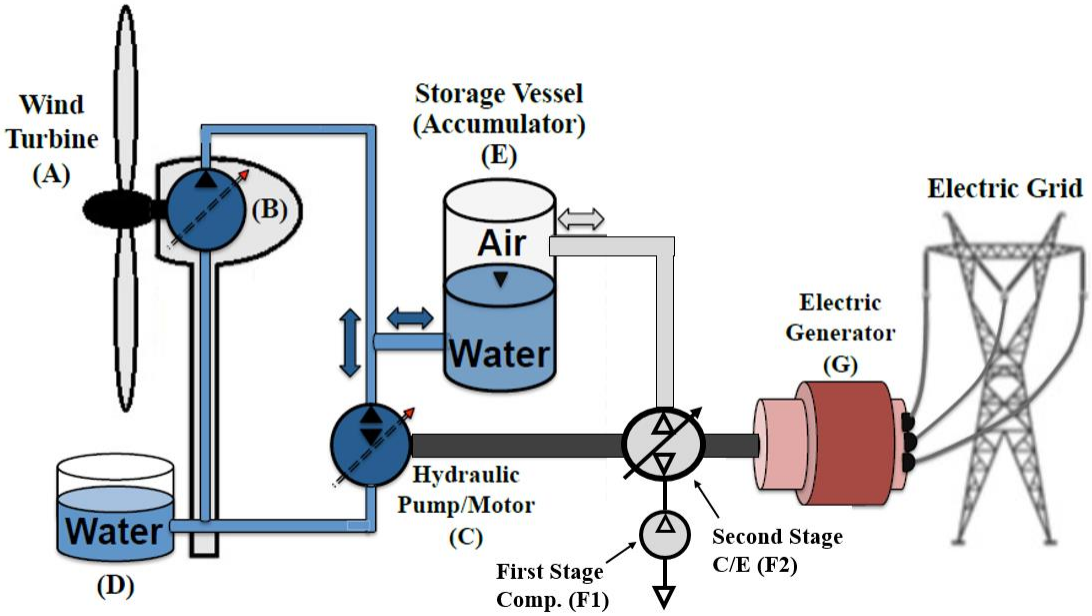

Figure 1.5: Novel CAES system with addition of first stage compressor.

Figure 1.5 shows the proposed CAES system with the addition of the first stage compressor along with the second stage compressor/expander. Initially, the air is taken at atmospheric pressure and compressed via the first stage compressor (F1) and stored in a low pressure reservoir (not shown). This low pressure air is then used for the energy storage process through compressing to high pressure with the second stage compressor (F2). During energy recovery, the expander will only expand the gas until the first stage

pressure is reached. Keeping a buffer of pre-compressed air will allow for fast compression/expansion of the air while remaining at a high energy level. Compressing the atmospheric air to the low pressure level does not require as much power when compared to the second stage compression. But in order to provide a large enough buffer of low pressure air, this process needs to happen quickly. This poses a problem since a liquid-air interface experiencing large accelerations can result in undesirable mixing. The stability of the interface relies most heavily on the acceleration of the more dense fluid. Therefore, inverting the liquid piston process can allow for the more dense fluid (water) to remain stationary while the gas is compressed.

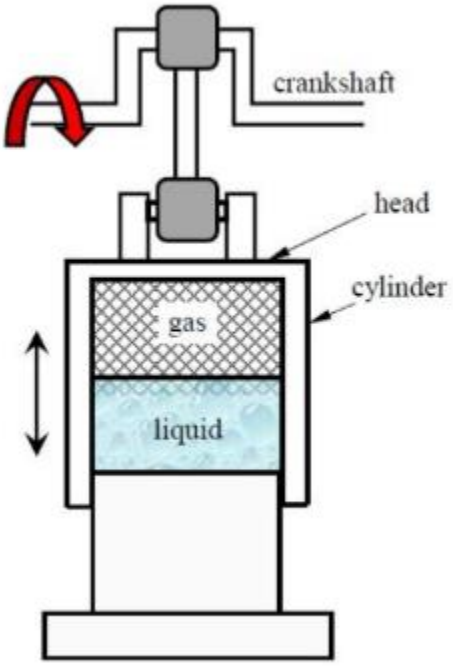

Figure 1.6: Inverted liquid piston compressor conceptual diagram.

Figure 1.6 shows the inverted liquid piston compressor (ILPC) used for the first stage compression of the air. The ILPC compresses the gas by keeping the liquid piston stationary while moving the chamber down towards the interface. This will compress the gas above the interface while keeping the denser fluid stationary thus increasing interface stability at high operating frequencies. The ILPC can still benefit from the superior liquid

gas seal and the addition of a porous media insert to improve heat transfer capabilities. Inverting the liquid piston compressor allows a crank shaft to drive the chamber up and down at a high frequency, quickly compressing large volumes of gas. The challenge with this method still resides within the stability of the liquid-air interface. This approach is expected to increase the allowable operating frequency to avoid interface stability [38]. Keeping the more dense fluid stationary greatly improves this, however now the interface is subject to many oscillating no slip boundary conditions during operation. Along with the oscillating chamber walls, the porous media now dips in and out of the liquid creating interface stability problems. Work conducted under this thesis studies the effect various porous media geometries have on interface stability during ILPC operation.

In summary, the typical CAES system has some inherent design challenges to overcome. In general, air compressors/expanders can be either powerful or efficient due to an inherent tradeoff between compressor/expander efficiency and power density. Being powerful and efficient is a design challenge. The other challenge is that the pressure inside of the storage vessel reduces as water or compressed air is removed, making maintenance of its pressure level at all energy levels difficult.

These challenges can be overcome by the development of a near isothermal liquid piston air compressor/expander and the use of an open accumulator for the compressed air storage vessel. Near-isothermal liquid piston compressor development displaying reduced leakage [11], inherent with the liquid piston, was augmented with the introduction of heat transfer porous media [12[13] through which the liquid piston flows. The heat transfer medium has a large surface area-to-volume ratio, providing many surfaces to facilitate heat transfer as the air being compressed increases in temperature. The liquid piston provides an excellent seal for the air while greatly reducing friction when compared to a traditional mechanical piston. As the air compresses and heats up, energy will transfer to the heat transfer medium and eventually into the water, creating a near-isothermal compression. The compressed air is ejected out of the chamber and stored in the storage vessel (E) once the chamber pressure exceeds the storage vessel pressure. To prepare for the next cycle, the water is driven from the chamber with pre-compressed (~7 bar) air filling the chamber. Retrieving energy from the compressed air

stored in the accumulator is essentially the reverse of this process. Air from the storage vessel is introduced into the chamber and allowed to expand, sourcing heat from the heat transfer medium as it expands so as to not decrease appreciably in temperature. During this expansion, the liquid piston retreats and drives the pump/motor, producing work.

The open accumulator is a device for maintaining compressor/expander efficiency and power levels at various storage vessel energy levels. This configuration uses a dual energy storage concept that can store/retrieve energy both hydraulically and pneumatically [10]. The pressure inside of (E) can be maintained through the coordination of the hydraulic and pneumatic power paths, regardless of energy content. Conventional hydraulic accumulators only have one inlet/outlet, which results in the pressure varying with the amount of fluid inside the accumulator. The open accumulator configuration allows liquid to enter the storage vessel (E) when compressed air is being extracted, allowing the pressure to remain the same. This keeps the storage vessel at the same pressure regardless of how much stored compressed air is inside. Pneumatically stored energy makes better use of the storage vessel (E) volume when compared to hydraulically stored energy (compressed air stores 20 times more energy than a hydraulic accumulator at the same peak pressure and total volume [10]). However, hydraulic pump/motors are more power dense than the pneumatic compressor/expanders. Utilizing the open accumulator architecture can take advantage of both by using the hydraulic power path to accommodate high power events such as gusts of wind or sudden power demands, while reserving the pneumatic power path for steady power requirements.

The primary component of the proposed CAES system is the near-isothermal liquid piston compressor/expander. Previous work has modeled and determined how certain design variables affect the power density of the compressor/expander. These design variables include the chamber geometry, distribution of porous material, and liquid piston compression trajectory. Results of this study have shown a compressor/expander design capable of reaching a power density increase of two orders of magnitude while maintaining a thermal efficiency of 92% [9]. These results have only been demonstrated through simulations and in limited experiments with single compression or expansion strokes. In order to showcase a commercially viable design, a

reciprocating, continuously operating scaled prototype is to be developed that both meets performance requirements and is cost effective.

1.4 Thesis Outline and Description of Chapters

The present thesis aims to develop a compressor/expander system cost function and determine how key design variables are varied when comparing a cost optimal design approach or a power density optimal design approach. Design tools developed in [9] are utilized in the calculations of system performance metrics, such as power density and thermal efficiency, combined with a developed system cost model to optimize the relevant design variables for overall cost. Cost optimal design parameters will then be used to build a functional scaled compressor/expander model that can be used to verify system performance. Good system power scalability will allow the laboratory experiments on a functional prototype to closely represent full-scale system performance. However, building the physical functional prototype is out of the scope of this thesis.

The main body of this thesis contains five chapters. Chapter 1 briefly introduces the need for integrating renewable energy resources and the problems that arise when attempting to introduce them to the electrical grid. Energy storage is necessary to make this integration of renewable energy to the electric grid viable. Current energy storage technologies, including CAES, are explored and compared. Chapter 1 also includes a review of relevant literature in the field, providing background information to the work presented in this thesis. Thesis goals and objectives are presented in this chapter.

The inherent tradeoff between compressor/expander efficiency and power density are introduced in Chapter 2. The concept of a liquid piston compressor/expander and relevant thermodynamic implications are presented. A one-dimensional air dynamic model is developed and used to study how design parameters affect efficiency. This model is used in Chapter 3 to verify a lumped parameter air model for use in cost optimization.

A cost model for the proposed compressor/expander as a function of specific design parameters is developed in Chapter 3. Previous optimal compression trajectory

techniques developed in [9] are used to determine optimal flow trajectories and performance results for each system iteration. The cost model is optimized on the basis of cost per power. A flow intensifier concept is developed in this chapter to aid in reducing system cost while increasing power density. A comparison of different optimization techniques is presented.

Chapter 4 explores the first-stage compression process necessary to the CAES system. This process takes air at atmospheric pressure and compresses it to the required first stage pressure (~7 bar) for use in the main CAES near-isothermal compressor/expander. The inverted liquid piston compressor is introduced in this chapter with a description of its operation. A two-dimensional liquid-air interface model is developed to simulate various operating conditions. Experimental data of the liquid-air interface motion is obtained for various porous media geometries and operating frequencies. The data is compared to the model and the results that describe the relationship between porous media geometry and liquid-air interface stability is presented.

A summary of the significant findings and contributions are provided in Chapter 5. This conclusion chapter will also summarize future work goals, including fabrication of the compressor/expander developed in chapter 3.

2. Thermodynamic Model of a Liquid Piston Compressor/Expander

2.1 Introduction

One of the most important components of the proposed CAES system design is the compressor/expander subsystem. For every cycle, the recoverable energy is subject to both the compression and expansion efficiencies. Therefore, a high efficiency air compressor/expander is required in order to make this method of energy storage viable. In order to achieve a high efficiency at a specified power level, the air compression/expansion must take place near isothermally. An isothermal compression/expansion is important because attempting to store gas at high temperatures, and thus high internal energy, will result in that energy being lost over time when stored. Achieving an isothermal compression/expansion in a short enough time to maintain the specified power level requires adequate heat transfer to take place during compression/expansion. Facilitating enough heat transfer during the compression will allow the air to reach high pressure without increasing in temperature, thus increasing efficiency. This becomes a challenge when compressing/expanding the air to 200 times atmospheric pressure, which will greatly heat/cool the air. A high efficiency can be achieved at demanding operating conditions such as this but due to the limited heat transfer available, it comes at the cost of compression/expansion time. Therefore, there is a natural tradeoff between efficiency and power density. A compressor/expander subsystem with high power density helps with both performance and system cost per power level. In order for the proposed CAES system to be commercially viable, an important design challenge is the creation of a highly efficient, power dense, and cost effective compressor/expander subsystem.

The proposed liquid piston compressor/expander concept is advantageous in many ways for achieving these difficult design requirements. Some of these advantages include:

1. **High heat transfer rate**: Because the liquid piston can deform and traverse around objects, the heat transfer in the compression chamber can be augmented by the inclusion of porous media inside the compression chamber and varying the shape of the chamber.
2. **Liquid recirculation**: During each cycle, the liquid compresses/expands the gas, during which heat can be transferred to/from the liquid. The liquid acts as a heat source/sink which aids in keeping the air temperature from rising/falling. An added benefit occurs when the liquid used as the piston can be recirculated back to tank, further dispelling any lingering captured heat to the atmosphere.
3. **Improved Sealing:** Since air has a relatively low viscosity, leakage can occur easily, decreasing efficiency. Traditional mechanical gas seals for high pressure applications require very tight tolerances and therefore add cost/friction. Liquid creates an excellent sealing surface, reducing friction and improving volumetric efficiency.
4. **Infinitely variable compression/expansion rate versus time:** The ability to control the rate at which the gas is compressed/expanded allows for an optimal flow rate trajectory to be found. Optimizing the rate of compression/expansion can augment heat transfer, improving efficiency and power density.

The advantages of this system with respect to heat transfer capabilities are the focus of this chapter. An accurate one-dimensional model of the air dynamics within the compression chamber is introduced and used to highlight the differences between the one-dimensional model and the lumped parameter model. This will serve as justification for the lumped parameter model being used in the optimization due to its accurate results and fast computation speed.

2.2 Thermal Efficiency versus Power Density Tradeoff

When it comes to compression, it is desired to compress a certain amount of air at initial state P_0, T_0 to a final state $T_f,\ P_f = rP_0$ where r is the compression ratio, within an amount of time t_c. As for expansion the reverse is true but the cycle begins at a high energy gas state $T_0,\ P_f = rP_0$ and expand the gas to lower pressure P_0 in a given expansion time t_e. This cycle is summarized in Figure 2.1. For compression, the total work required to bring the gas to the final state is described as:

$$W_{in} = -\int_{V_0}^{V_c} (P - P_0)\, dV + P_0(r-1)V_c + \int_0^{t_c} W_f dt \tag{2.1}$$

the first right-hand side term in (2.1) represents the work needed to compress the air from the initial pressure P_0 to the final pressure rP_0. The second right-hand side term represents all of the work attributing to the isobaric cooling of the air as its temperature drops back to ambient and the ejection work needed to expel the pressurized air into the storage vessel. The last term is the summation of mechanical and viscous losses accumulated during the compression cycle and lumped together as friction power W_f.

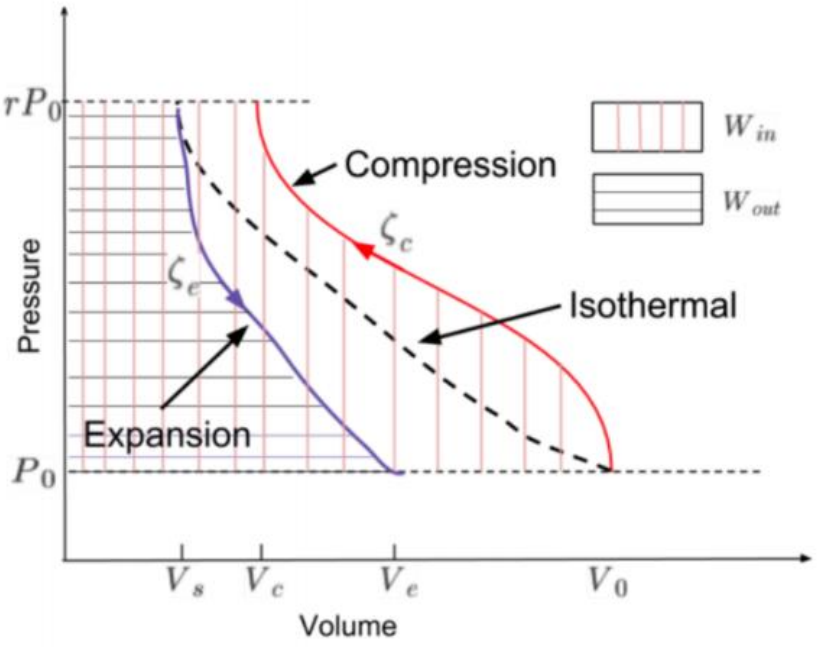

Figure 2.1: Compression/Expansion process of air (pressure vs. volume) [9].

The total stored energy E_{st} in the air after compressing to final pressure rP_0 and after cooling to ambient temperature T_0 in the storage vessel can be defined as the maximum obtainable work via an isothermal expansion:

$$E_{st} = P_0 V_0 \ln(r) \tag{2.2}$$

where V_0 is the air volume after compressing air to final pressure rP_0. This assumes that the gas is ideal. Furthermore, the work done by the atmosphere is subtracted in (2.2) while the ejection work is included. Compression efficiency and power density are then defined as:

$$\eta_c = \frac{E_{st}}{W_{in}} \times 100\% \tag{2.3}$$

$$PD_c = \frac{E_{st}}{V_{chamber} t_c} = \frac{P_0 V_0 \ln(r)}{V_{chamber} t_c} \tag{2.4}$$

where $V_{chamber}$ is the volume of the compression chamber and t_c is the compression time. From (2.4) shows that as compression time increases, the power density decreases.

2.3 1-D Model of Liquid Piston Gas Compression

In order to effectively predict how a liquid piston compressor/expander design will perform, an accurate thermodynamic model of the system must be developed. Previous studies have developed a two-dimensional model [39[40] of the heat transfer correlation between different heat transfer material insert geometries. However, two dimensional models are quite computationally expensive and are not suited for the multiple design iterations required for design optimization. On the other hand, a one-dimensional lumped air properties model does not completely incorporate the influence of chamber geometry and heat transfer material distribution. Therefore, a one-dimensional model of the air dynamics inside the compression/expansion chamber has been developed to further verify the quickly computed zero-dimensional model used for optimization in chapter 3. The one-dimensional model used in this thesis is similar to the model first derived in the moisture content study which investigated the effects air moisture content had on the liquid piston compressor/expander performance [51]. However, this model assumes dry air and therefore does not include the water content terms. Beginning with the first law of thermodynamics:

$$\dot{E}_{tot} = -\dot{W} - HT = -P\dot{V} - HT \tag{2.5}$$

where $\dot{E}_{tot}$ is the rate of change of internal energy for the air, $-P\dot{V}$ is the work done by the liquid piston (such that $-\dot{V} = Q$, the pump/motor flow rate), and HT is the rate of

heat transfer out of the system. Changes in temperature will give rise to changes in air internal energy:

$$\dot{E}_{tot} = m\left(\frac{\partial e}{\partial T}\dot{T} - \frac{\partial e}{\partial \rho}\dot{\rho}\right) = m\left(\frac{\partial e}{\partial T}\dot{T} - \frac{\partial e}{\partial \rho}\frac{\rho}{V}\dot{V}\right) \tag{2.6}$$

where e is the specific energy of air. Combining (2.6) into (2.5) and simplifying yields:

$$m\frac{\partial e}{\partial T}\dot{T} + \left(P - \frac{\partial e}{\partial \rho}\rho^2\right)\dot{V} + HT = 0 \tag{2.7}$$

which can be further simplified to:

$$A(T,\rho)\dot{T} = -B(P,T)\dot{V} - HT \tag{2.8}$$

where,

$$A(T,\rho) = m\frac{\partial e}{\partial T} \tag{2.9}$$

$$B(P,T) = \left(P - \frac{\partial e}{\partial \rho}\rho^2\right) \tag{2.10}$$

The final term in (2.8) accumulates the heat transfer which occurs during the simulation which is given by:

$$HT = h(t)a(t)(T(t) - T_0) \tag{2.11}$$

where $h(t)a(t)$ is the product of heat transfer coefficient and heat transfer surface area that varies with time. The temperature of the chamber walls and heat transfer material T_0 is assumed constant. To provide an accurate representation for the term governing heat transfer $h(t)a(t)$, a correlation of the heat transfer coefficient h between the air and heat transfer material must be derived. A specific correlation between h and the Nusselt number (Nu) has been found for the cross plate heat exchanger geometry used in this study, given by [31]:

$$Nu = \frac{hD_H(v)}{k(T)} = c_1 + c_2 Re^{c_3} Pr^{c_4} \tag{2.12}$$

where h is the convective heat transfer coefficient, D_H is the hydraulic diameter of the porous insert at air volume v, and $k(T)$ is the air conductivity as a function of temperature. The constants c_1, c_2, c_3, and c_4 where determined by the study to be ($c_1 = 9.7, c_2 = 0.0876, c_3 = 0.792, and\ c_4 = 0.33$). Lastly, the Prandtl number $Pr = 0.7$ and Reynolds number of air at volume v is defined as:

$$Re = \frac{\rho D_H(v)|u(v)|}{\mu(T)} \tag{2.13}$$

This correlation given by (2.12) is valid for $Re < 5000$ according to [31]. In the Reynolds number calculation (2.13), $\mu(T)$ is the dynamic viscosity of air at temperature T, and $u(v)$ is the Darcian air velocity at volume v:

$$u = \frac{v}{V(t)\Phi(t)} Q(t) \tag{2.14}$$

here $Q(t)$ is the flow rate into the chamber, $V(t)$ is the gas volume, and $\Phi(t)$ is the chamber cross sectional area all at time t. This calculation of Darcian air velocity is made under the assumption that the air flow rate at a given cross sectional area is linear to the

volume of air above that section. Therefore, the air flow rate is equal to the liquid-air interface at the interface while it is zero at the top cap.

The one-dimensional model partitions the chamber volume into separate sections, each with their own density ρ_i, temperature T_i, and mass m_i. Each partition boundary changes elevation as a function of time such that the position of partition i at time t is represented by the $X_i(t)$ (top boundary) and $X_{i-1}(t)$ (bottom boundary). Here the boundary at $i = 0$ is the top cap of the chamber and the boundary at $i = n$ is the liquid-air interface between the compressible volume of air and the liquid piston (see Figure 2.2). Allowing the volume partitions to move throughout the simulation in a deformable mesh type of approach permits further simplification of the governing equations. The partition boundaries $X_i(t)$ move in a manner which provides a uniform pressure throughout the simulation, assuming the mass m_i is constant in each partition. With there being no pressure gradient across partition boundaries, the inertial effects of the air can be ignored in the governing Navier-Stokes equation. Note that this assumption is valid since the pressure dynamics response is orders of magnitude faster than air density and temperature. This simplification greatly improves computational efficiency.

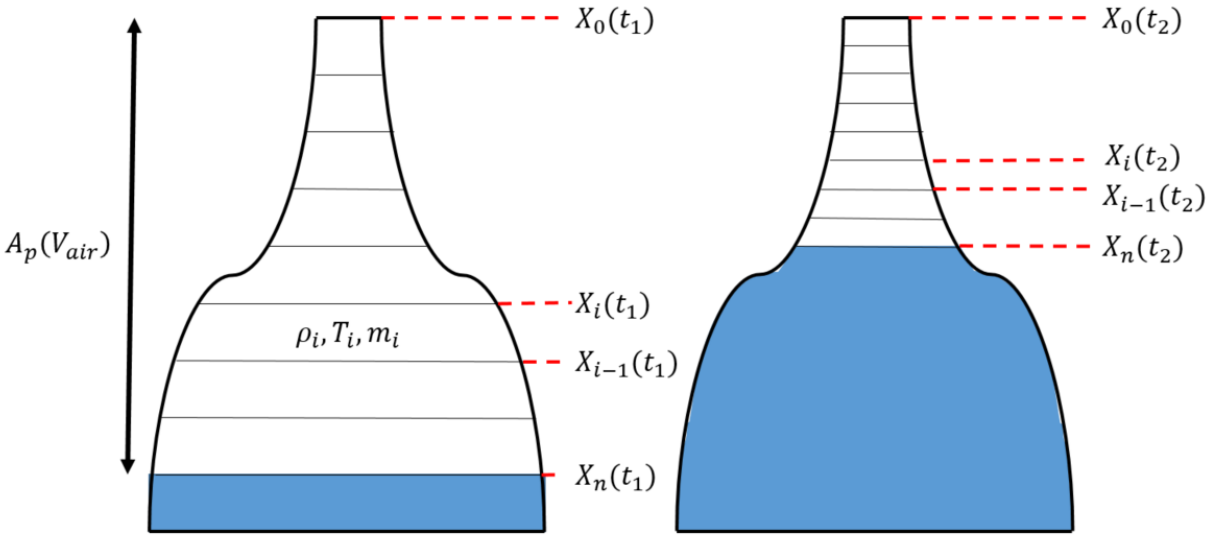

Figure 2.2: One-dimensional deformable partition boundaries at initial time t_1 and later time t_2 used in thermodynamic model.

Each partition is modeled to allow for convective heat transfer between the walls and the heat transfer material (if present). In this model, it is assumed that no heat transfer occurs between air and the top cap of the chamber or the liquid. This assumption was made to match the zero-dimensional assumptions to ensure an accurate comparison of the two methods. Including these two surfaces for heat transfer would only aid in the compression/expansion efficiency, therefore this assumption creates a more conservative model. As for conduction, the model includes heat transfer between the center points of two successive partitions:

$$HT_{i,conduct} = \frac{2A_p \cdot k(T_i)}{(X_i - X_{i-2})}(T_i - X_{i-1}) + \frac{2A_p \cdot k(T_i)}{(X_{i+1} - X_{i-1})}(T_i - X_{i+1}) \tag{2.15}$$

where A_p is the cross sectional area of the partition and k is the thermal conductivity of air. The pressure with each partition is a function of temperature and density:

$$P_i = P(T_i, \rho_i) \tag{2.16}$$

the rate of change of pressure can be calculated as:

$$\dot{P}_i = -\underbrace{\left(\left(\frac{\partial P}{\partial T}\right)\frac{B_i}{A_i} + \frac{\partial P}{\partial \rho}\frac{\rho}{V}\right)}_{\beta_i}\dot{V}_i - \underbrace{\left(\frac{\partial P}{\partial T}\right)\frac{1}{A_i}HT_i}_{\alpha_i} \tag{2.17}$$

here HT_i represents the total heat transfer for partition i. To ensure uniform pressure throughout all partitions, the deformation of partitions $\dot{V}_i$ is defined such that $P_1(t) = P_2(t) = \cdots = P_n(t)$. This is achieved by the implementation of stable dynamics:

$$\Delta\dot{P}_i = -\lambda\Delta P_i \tag{2.18}$$

where $\lambda > 0$ is a sufficiently small number and $\Delta P_i \equiv P_{i+1} - P_i$. Ensuring λ is a small number will provide desired pressure dynamics, allowing for (2.17) to be written in matrix form:

$$\begin{bmatrix} \alpha_2 - \alpha_1 \\ \alpha_3 - \alpha_2 \\ \vdots \\ \alpha_n - \alpha_{n-1} \\ Q \end{bmatrix} + \lambda \begin{bmatrix} \Delta P_1 \\ \Delta P_2 \\ \vdots \\ \Delta P_n \\ 0 \end{bmatrix} = \begin{bmatrix} \beta_1 & -\beta_2 & 0 & \cdots & 0 \\ 0 & \beta_2 & -\beta_3 & 0 & \cdots \\ 0 & 0 & \ddots & \ddots & 0 \\ 0 & \cdots & 0 & \beta_{n-1} & -\beta_n \\ -1 & -1 & \cdots & -1 & -1 \end{bmatrix} \begin{bmatrix} \dot{V}_1 \\ \dot{V}_2 \\ \vdots \\ \dot{V}_l \\ \dot{V}_n \end{bmatrix} \tag{2.19}$$

where α_i and β_i are defined above in (2.17) and Q is the liquid piston flow rate. The matrix equation can then be solved for the change in partition volumes $\dot{V}_i$. The partition boundaries will move at velocity $\dot{X}_i$ and are calculated by:

$$\dot{X}_i = \frac{1}{A_p} \sum_{k=1}^{i} \dot{V}_i \tag{2.20}$$

where A_p can be varying with respect to air volume (i.e. varying cross sectional diameter of chamber and porosity of heat transfer material insert). The partition boundary velocity is used for the heat transfer coefficient calculation using the relationship described in (2.12). When calculating the heat transfer coefficient, the mean partition velocity is used for the Darcian air velocity for calculating the Reynolds number (Re):

$$u = \frac{\left(\dot{X}_i + \dot{X}_{i-1}\right)}{2} \tag{2.21}$$

This corresponds to generally a high velocity at the liquid air interface and decreases upwards to the top cap of the chamber.

2.4 Comparison of 1-D and 0-D Model

The one-dimensional model described in section 1.2 and the zero-dimensional model described in section 2.2 were computed for the same compressor design and compared. Various nodes along the height of the 1D model were plotted to show the variation of temperature throughout the chamber. For this test case, the cross sectional area of the chamber and the porosity were assumed constant. The chamber geometry was that of a cylinder with a constant diameter of 4.7cm. The entire chamber was filled with heat transfer material with a constant porosity of 80% (where 100% would mean there is no heat transfer material). Heat transfer material was assumed to be ABS plastic in a cross plate heat exchanger geometry with a plate thickness of 0.8mm. This heat exchanger geometry and material was extensively studied in [31]. The liquid piston is supplied a flow rate $Q(t)$ that varies in time with respect to the hardware limitations of the variable displacement pump ($0 \leq Q(t) \leq Q_{max}$ for all t). This flow rate was controlled using the methods shown in [9] to provide a thermal efficiency of 92% while minimizing compression time. The same flow rate, heat transfer material, and chamber geometries were used for both simulation techniques. A table of the initial parameters for both simulations can be seen in Table 2.1:

Table 2.1: Table of fixed parameters used in 1-D and 0-D simulations

Parameter	**Value**	**Unit**	**Parameter**	**Value**	**Unit**
Initial Pressure	7	bar	Initial Air Temperature	298	K
Final Pressure	200	bar	Initial Solid Temperature	298	K
Initial Air Volume	4	lit	Prandtl Number of Air	0.7	-
Porous Material Volume	0.8	lit	Heat Capacity of Solid	1600	J/Kg.K

The one-dimensional simulation results in Figure 2.3 show temperature trajectories for various partitions within the chamber. A gradient in temperature appears in these results. The direction of increasing temperature starts from the liquid-air

interface and ends towards the top cap of the chamber. This is due to the high air velocity near the liquid surface compared to the low air velocity near the top cap. The high velocity air has increased heat transfer capabilities due to the relation between the heat transfer coefficient and air velocity. Note that if the convective heat transfer through the top cap surface area were included, the end cap node would show a smaller temperature while adjacent nodes to the surface would show the highest temperature readings. A comparison of temperature trajectories between the zero-dimension lumped parameter model and the one-dimensional model can be seen in Figure 2.4. It should be noted that the final air temperature for the zero-dimensional case is about 370K whereas the final mass average air temperature of the one-dimensional case is 360K. There is also a notable lower average temperature throughout most of the compression cycle in the one-dimensional case when compared to the zero-dimensional case. This is due to the inclusion of the variable properties, such as thermal conduction and Reynolds number calculations, across all of the nodes. These properties have a nonlinear impact on the heat transfer, and results in augmentation of the heat transfer capabilities. The zero-dimensional model calculates the heat transfer as if there is only a single node within the chamber (lumped parameter), and therefore does not include these variations. If the model was extended to two dimensions, the inclusion of vortices within the air dynamics would be present [41]. Secondary flows such as this would further act upon the heat transfer insert surface area, enhancing heat transfer. Figure 2.3 shows the gas temperature versus time for a compression cycle using a chamber of constant cross-sectional area and porous media distribution.

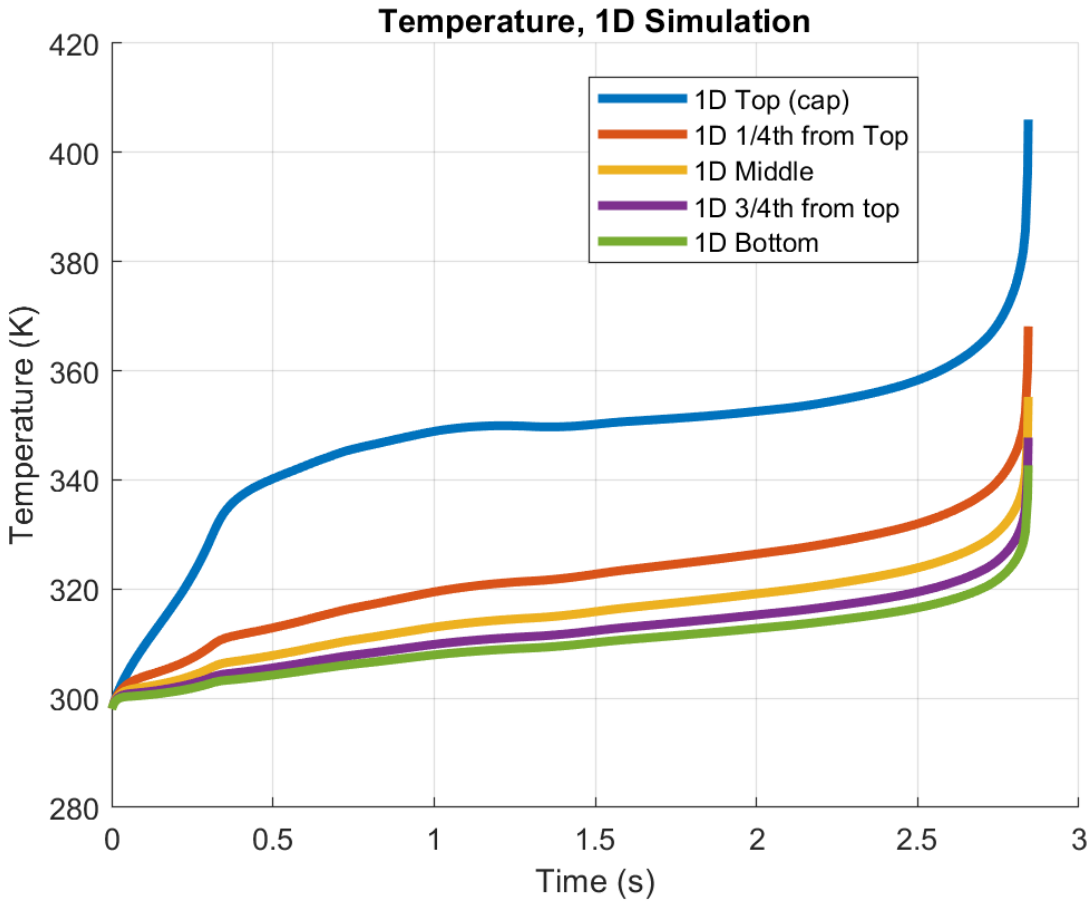

Figure 2.3: 1-D simulation temperature trajectory results for various nodes. “Bottom” corresponds to the liquid-air interface and “Top” corresponds to the chamber end cap.

The zero-dimensional model is calculated in a similar manner to the one-dimensional case, however now instead of n many nodes there is only a single node. With there being only one node, the heat transfer coefficient is still calculated by Nusselt number relationship in (2.12). For the sake of comparison, the porous media distribution and chamber cross sectional area where held constant in both models so the heat transfer coefficient for conduction was the same. Figure 2.4 shows the result temperature versus time results for both models for the same compression trajectory and chamber

parameters.

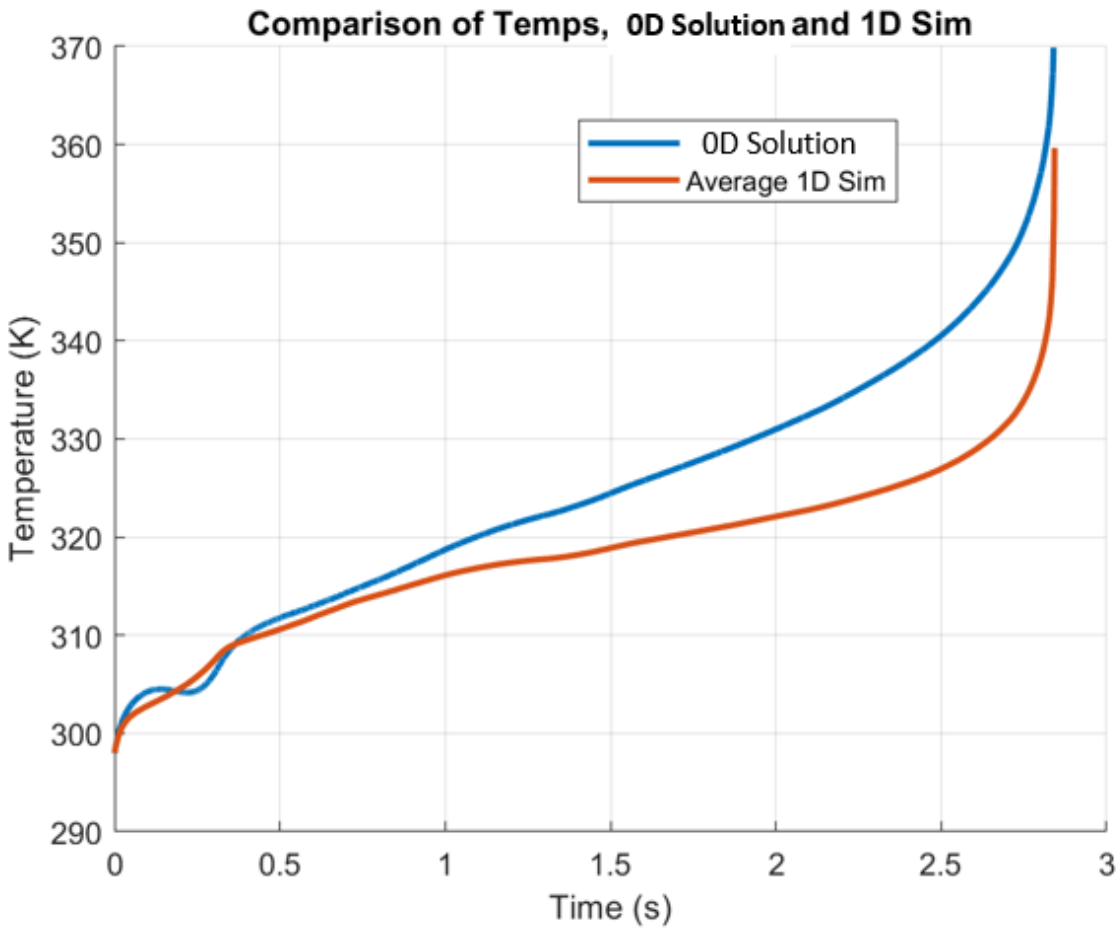

Figure 2.4: 0-D and 1-D temperature trajectories.

The results of the two simulation methods show a notable difference in average temperature between the two simulation methods. More complicated modeling of the heat transfer in the one-dimensional case accounts for the lower temperature change. Mitigating temperature rise during compression can greatly improve thermal efficiency. To see how the models compared in terms of compression performance, various simulations were conducted using both modeling approaches. The zero-dimensional model was simulated using various compression times in order to achieve a range of compression efficiencies. The same compression trajectories from the zero-dimensional case were then used in the one-dimensional model and the results compared. For the same thermal efficiency, a greater power density is achieved via the one-dimensional

model due to the model prediction discrepancies. The chamber parameters used in this test include a constant cross-sectional chamber of diameter 4.7cm and constant porosity distribution of 80%. Maximum pump flow rate was varied until each desired efficiency was achieved. Table 2.2 shows simulation results for a specified range of compression thermal efficiencies ($\eta_c = 89\%: 1\%: 93\%$) and the resulting power densities.

Table 2.2: Thermal compression efficiency and power density results for 0-D and 1-D simulation methods.

η_c 0-D	η_c 1-D	Power Density 0-D $[kW/m^3]$	Power Density 1-D $[kW/m^3]$
88.99%	90.29%	2760	2744
89.92%	91.03%	1995	1984
91.01%	91.91%	1247	1242
91.88%	92.61%	828	825
92.98%	93.52%	481	480

Results show good agreement between the modeling methods proposed. However, there is a notable increase in efficiency for the one-dimensional case. From these results it can be assumed that the zero-dimensional modeling method will be conservative with respect to thermal efficiency. Since the one-dimensional simulation is relatively computationally expensive, utilizing the zero-dimensional modeling approach for optimization is justified due to its conservative nature.

When examining the relationship between efficiency and power density for compression one can see the natural tradeoff that occurs. Increasing maximum pump flow rate will decrease the time required to compress a specified gas volume V_0 and therefore increases power density as seen in *Figure 2.5*.

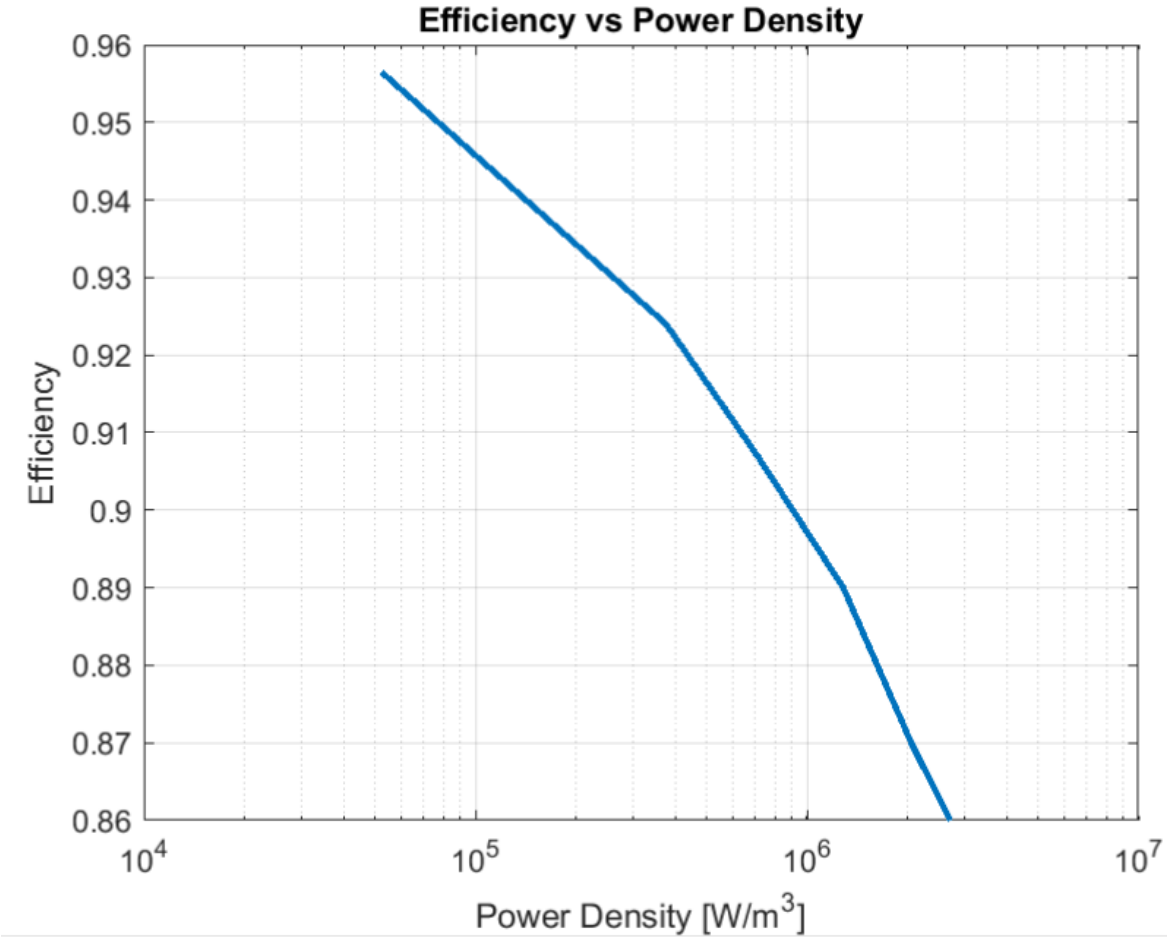

Figure 2.5: Compression efficiency (η_c) versus Power Density (PD_c). $V_0 = 4.5\ L$, $P_0 = 7\ bar$, $\eta_c = 86\%{:}\ 1\%{:}\ 96\%$.

Figure 2.5 shows the logarithmic relationship between efficiency and power density (an order of magnitude increase in power density will result in an efficiency decrease of about 5%). It is with this relationship that the design problems arise. Maximizing heat transfer capabilities should yield positive effects in both power density and efficiency, essentially translating the curve shown in Figure 2.5 to the right.

2.5 Summary

In this chapter, the inherent tradeoff between air compression/expansion efficiency and system power density was discussed. The discussion outlines the importance heat transfer has on air compression/expansion performance. For a given efficiency, achieving

greater heat transfer correlates to a reduction in compression time (thus increasing power density). Various methods have been introduced to augment the heat transfer capabilities of the compressor/expander design. One of these methods includes the introduction of heat transfer material into the chamber, which increases available heat transfer area by an order of magnitude. Improving the rate at which heat transfers from the air to the porous material will minimize the air temperature rise/fall during the compression/expansion process greatly improving efficiency. The liquid piston approach allows for the heat transfer material to reside inside of the compression/expansion chamber, a significant advantage of this design approach. Other advantages include improved sealing, variable chamber geometry, and infinitely variable liquid piston trajectories provided by a variable displacement pump/motor. To quantify each design iteration's performance, a one-dimensional air dynamic model was developed. The results of the one-dimensional model described in this chapter and the zero-dimensional modeling approach were compared. The zero-dimensional model proved to be a conservative description of chamber performance compared to the one-dimensional. Since optimization revolves around testing multiple design iterations, the quickly computed zero-dimensional case was deemed proficient for the optimization process. The resulting efficiencies of the designs optimized using this modeling method would only see theoretical improvement if modeled with greater complexity.

3. Cost Optimal Design of a Second Stage liquid Piston Compressor

3.1 Introduction

One of the most critical components of this CAES system is the second stage (7-200 bar) compressor/expander. This component is responsible for the process of converting between mechanical work and stored compressed air. In order for this conversion process to be worthwhile, a high thermal efficiency is required while also remaining power dense. For a fixed compression/expansion ratio, a high power density results in a shorter cycle time. When designing for a commercially viable CAES system, achieving a high power density will result in smaller/cheaper components for the same power capability. As described in chapter 1, there is a tradeoff between efficiency and compression/expansion cycle time. Allowing more time for heat transfer during the compression/expansion process will result in a higher efficiency but at the expense of reducing power density. If the resultant system power density is not sufficiently high, larger components will be required to reach the system power specifications.

The second stage compressor/expander architecture proposed here uses a liquid column to compress/expand air above it in the compression chamber. In effect, the liquid column acts like a mechanical piston which extends and retracts to compress the air. However, this poses another problem of the stability of the liquid-air interface as the liquid traverses through the heat transfer media. This is more prevalent at higher liquid piston velocities and is analyzed further in chapter 4 when used with the first stage liquid piston compressor. Instability of the liquid-air interface can cause mixing, which will lead to air bubbles becoming entrained in the liquid column. This is undesirable, as it will reduce the amount of compressed air that can be stored per cycle. For the second stage compressor/expander, the liquid-air interface can become unstable if the maximum deceleration of the liquid exceeds a certain value [17[18]. Since liquid can deform and

flow through a tortuous path, heat transfer material can be placed inside of the compression chamber to facilitate further heat transfer and provide heat capacitance [12[13]. Previous CFD analysis [19] and experiments [20[21] have shown that including heat transfer material inside of the compression/expansion chamber can improve thermal efficiencies by more than an order of magnitude when compared to chambers with no material present.

By designing a highly power dense system, there comes the added benefit of a reduction in component size/cost for a desired power level. Previous work has utilized a complex heat transfer correlation to optimize the compression trajectory, porosity distribution and shape of the compressor in order to achieve maximum power density. For a given maximum and minimum compression rate, the optimal compression trajectory was calculated via a Dynamic Programming approach and Lagrange multiplier method. The power density optimization also included system design parameters such as chamber geometry and distribution of heat transfer media. Findings show optimal chamber shape (when chamber height is constricted) to include a wider base with a narrow top, while the optimal heat transfer media distribution places no material in wide base section and all of the available material in the narrow top. These design parameters capitalize on the heat transfer benefits near the end of the compression cycle (when the heat transfer coefficient is large). The resulting power density optimized compressor/expander is further described in [9]. Achieving high power density can potentially reduce system cost per power level, however the resulting components of the compressor/expander can be more complex/expensive when optimizing power density. Therefore, optimizing for system power density does not necessarily also optimize for cost. This in turn creates a tradeoff between the cost and power density of the compressor/expander.

In this chapter, an investigation of a compressor/expander design optimized for power density and for cost is conducted. A cost function for the system is developed for a given set of system design parameters. The cost function is then optimized via a gradient search method while a Lagrange multiplier method ensures that the system achieves the desired thermal efficiency, similar to the calculations in [9]. System cost is then

minimized and the design scaled to the desired power level for this project. The scaled cost optimal system is then compared to the scaled power density optimized system.

3.2 Power Density Optimized Compressor/Expander Overview

The previous methods of optimizing power density applied by [9] are leveraged in this thesis to optimize for cost. A complex heat transfer correlation that utilizes instantaneous air properties, heat transfer material properties, and chamber geometry is used to calculate the convective heat transfer coefficient. This heat transfer coefficient is paramount to the calculation of the compression trajectory being optimized. The heat transfer coefficient relates the compressor/expander system geometry, heat transfer material insert distribution, and liquid piston trajectory to the ability to transfer heat from the gas. Without adequate heat transfer, the compressing gas will increase in temperature. Storing the gas in this state of increased internal energy will most likely result in the energy being lost to the storage vessel surroundings. However, facilitating good heat transfer during the gas compression will mitigate the rise in temperature, reducing the amount of wasted stored energy and therefore increasing efficiency. Only through an isothermal compression can all of the energy stored in the gas be recovered at a later time, however achieving that level of heat transfer would take a very long compression time. Because of the limited amount of heat transfer, there is an inherent trade-off between efficiency and power. The system power is characterized by the compression/expansion time, which can be found by starting with the first law of thermodynamics:

$$\Delta W = \Delta Q + \Delta E_{tot} \tag{3.1}$$

where the change in heat transfer from the air to the walls of the chamber ΔQ in addition to the change in internal energy of the air ΔE_{tot} produce the change in piston work ΔW. By choosing to define the air dynamic states in terms of pressure and density, the specific energy and temperature become dependent variables according to the real gas model [42] *E. W. Lemmon, R. T. Jacobsen, S. G. Penoncello, D. G. Friend, "Thermodynamic*

properties of air and mixtures of nitrogen, argon, and oxygen from 60 to 2000 K at pressures to 2000 MPa," Journal of Physical and Chemical Reference :

$$e = e(P, \rho) \tag{3.2}$$

$$T = T(P, \rho) \tag{3.3}$$

using this definition of air states, the differential equation for the first law of thermodynamics can be written as:

$$-PdV = \left[\overline{hA}(P, \rho, Q) \cdot (T - T_s)\right]dt + m\, de \tag{3.4}$$

where $\overline{hA}$ is the volume averaged heat transfer coefficient, T_s is the temperature of the heat transfer insert (assumed to be constant), m is the air mass (also assumed constant). $\overline{hA}$ is a function of the liquid piston flow rate Q as well as air pressure, P, and density ρ. With air mass assumed constant, the rate of volume change can be described by:

$$\frac{d}{dt}m = \frac{d}{dt}(\rho V) = 0 \Rightarrow \dot{V} = -\frac{m}{\rho^2}\dot{\rho} \tag{3.5}$$

combining (3.5) into (3.4), a model for zero-dimensional air dynamics can be written as:

$$m\frac{\partial e}{\partial P}\dot{P} = \left(P - \frac{\partial e}{\partial \rho}\rho^2\right)Q(t) - \left[\overline{hA}(P, \rho, Q) \cdot (T - T_s)\right] \tag{3.6}$$

$$\dot{\rho} = \frac{\rho^2}{m}Q(t) \tag{3.7}$$

where $Q(t)$ is the liquid piston flow rate into the compression/expansion chamber at time t. This formulation of the air dynamics within the chamber can describe the air specific energy e and temperature T as dependent variables calculated from air pressure P and density ρ. Since the liquid piston flowrate Q can be controlled during the compression/expansion process, this parameter can be used to calculate which flow trajectory would compress/expand the air to the desired state at a desired efficiency. The efficiency largely depends on the heat transfer during the process. The term governing heat transfer $\overline{hA}(P, \rho, Q)$, is calculated using the same methods as described in chapter 2 but with a few alterations. Recall the specific correlation for the Nusselt number (Nu) for the cross plate heat exchanger geometry used in this study, given by equation (2.12):

$$Nu = \frac{hD_H(v)}{k(T)} = c_1 + c_2 Re^{c_3} Pr^{c_4} \tag{2.12}$$

where h is the convective heat transfer coefficient, $D_H(v)$ is the hydraulic diameter of the porous insert at air volume v, and $k(T)$ is the air conductivity as a function of temperature. The Prandtl number $Pr = 0.7$ and Reynolds number of air at volume v is defined as:

$$Re = \frac{\rho D_H(v)|u(v)|}{\mu(T)} \tag{3.8}$$

this correlation given by (2.12) is valid for $Re < 5000$ according to [12]. In the Reynolds number calculation, $\mu(T)$ is the dynamic viscosity of air at temperature T, and $u(v)$ is the Darcian air velocity at volume v:

$$u = \frac{v}{V(t)\Phi(t)} Q(t) \tag{3.9}$$

here $Q(t)$ is the flow rate into the chamber, $V(t)$ is the gas volume, and $\Phi(t)$ is the chamber cross sectional area all at time t. As before, this formulation of Darcian air velocity is made under the assumption that the air flow rate at a given cross sectional area is linear to the volume of air above that section. Therefore, the air flow rate is equal to the liquid-air interface at the interface while it is zero at the top cap. From these equations, a formulation for the volume averaged heat transfer coefficient $\overline{hA}$ can be calculated as:

$$\overline{hA} = \int_0^{V(t)} h(P, \rho, Q)\Omega(v)dv \tag{3.10}$$

where the heat transfer area density at volume v is represented by $\Omega(v)$ and h is the convective heat transfer coefficient calculated via (2.12). $\Omega(v)$ represents the heat transfer area divided by the total air volume $V(t)$ (in units of $[m^2/m^3]$), when integrated over air volume, the result is the total area for heat transfer at time t. Reducing this equation into a simplified form yields:

$$\overline{hA} = c_1 k(T) M_{(V)} + c_2 k(T) \left(\frac{\rho}{\mu(T) \cdot V}\right)^{c_3} Pr^{c_4} Q^{c_3} N_{(V)} \tag{3.11}$$

where $M_{(V)}$ and $N_{(V)}$ are only functions of total air volume $V(t)$:

$$M_{(V)} = \int_0^{V(t)} \frac{\Omega(v)}{D_H(v)} dv \tag{3.12}$$

$$N_{(V)} = \int_0^{V(t)} \frac{\Omega(v)}{D_H(v)^{1-c_3}} \cdot \left(\frac{u(v)}{\Phi(t)}\right)^{c_3} dv \tag{3.13}$$

the history of air dynamic states (pressure and density) can be obtained for a given compression/expansion trajectory (with initial condition P_0 and ρ) by integrating (3.6) and (3.7) with respect to time. Combining the heat transfer coefficient expression (3.11) into (3.6), the required compression time can be calculated as a dependent variable that is a function of pressure:

$$\left(m\frac{\partial e}{\partial P}\right)\frac{dP}{dV} = \frac{\overline{hA}}{Q(t)}(T(P,\rho) - T_s) - \left(P - \rho^2\frac{\partial e}{\partial \rho}\right) \tag{3.14}$$

with compression time as a function a pressure being calculated by:

$$t_c = -\int_{P_0}^{P_f} \frac{1}{Q(P)}\frac{dV}{dp}dp \tag{3.15}$$

therefore, omitting the time differentiation required in (3.6). Formulating compression time in this manner allows us to control the liquid piston flow rate $Q(P)$ at pressure P to minimize compression time and therefore maximize power density. However, due to the limited heat transfer available, there is an inherent tradeoff between compression time and compression efficiency. Ensuring an equality constraint is satisfied will allow for the optimization of compression time given a desired efficiency:

$$-\int_{P_0}^{P_f} P\frac{dV}{dP}dP + P_f V_f - P_0 V_0 = \frac{E_{st}}{\eta^*} \tag{3.16}$$

the left side of (3.16) represents the required work to compress the gas given the compression trajectory and this is equated to the energy stored E_{st} divided by the desired efficiency η^* (essentially saying the work required to compress the gas is equal to the work required to compress the gas at the desired efficiency specified). The variable being

optimized $Q(P)$ is also limited to reside between a minimum and maximum available flow rate:

$$0 \leq Q(P) \leq Q_{max} \tag{3.17}$$

therefore, the optimal flow rate trajectory given the performance constraint (3.16) and the hardware limitations imposed on the optimization variable in (3.17) can be expressed as:

$$\tilde{Q} = \min_{Q(P)} \left\{ -\int_{P_0}^{P_f} \frac{1}{Q(P)} \frac{dV}{dP} dP \right\} \tag{3.18}$$

here $\tilde{Q}$ represents the flow rate as a function of pressure P (such that $P \in [P_0, P_f]$) that minimizes compression time t_c. Without the performance constraint, this flow trajectory would remain at Q_{max} for all pressures. In order to ensure that both constraints (3.16) and (3.17) are satisfied, the Lagrange Multiplier method for constrained optimization *[54*] is utilized by introducing a Lagrange multiplier (λ) and defining the Lagrangian as:

$$L = -\int_{P_0}^{P_f} \left(\frac{1}{Q(P)} + \lambda P \right) \frac{dV}{dP} dP + \lambda \left(P_f V_f - P_0 V_0 - \frac{E_{st}}{\eta^*} \right) \tag{3.19}$$

where now minimizing the Lagrangian for a given λ would yield the optimal flow trajectory $\tilde{Q}$ and then maximizing this over λ would yield the optimal flow trajectory that satisfies the equality constraint (3.16):

$$\{\tilde{\lambda}, \tilde{Q}\} = \max_{\lambda} \left\{ \min_{Q(P)} (L(\lambda, Q)) \right\} \tag{3.20}$$

Dynamic Programming (DP) was used to solve the minimization problem inner loop while a bisectional search was used to maximize over λ outer loop. The result is a very

computational efficient method for calculating the optimal compression trajectory given the desired efficiency equality constraint. The optimal flow trajectory optimization is calculated for a given chamber geometry and porous media distribution. To supply this inner optimization with an optimal chamber, an outer optimization must be solved to provide the complete chamber geometry and porous media distribution that yields the highest power density. For a given height constraint, there exists an optimal chamber cross sectional area ($\widetilde{\Phi}$) and porosity distribution ($\widetilde{\Psi}$) at each air volume that yields the maximum power density (for a given total chamber and porous media volume). Figure 3.1 shows a concept diagram of the chamber including varying shape and porous media distribution. Define Λ as the total cross sectional area minus the area occupied by heat transfer material as a function of air volume:

$$\Lambda(v) = \Phi(v) \times \Psi(v) \tag{3.21}$$

where porosity $\Psi \in [0,1]$, with $\Psi = 0$ describing complete total area consisting of heat transfer material and $\Psi = 1$ meaning there is no heat transfer material. This correlation can be used to calculate the chamber cross sectional area Φ given the porosity distribution and open area are known. By fixing the total porous material volume and total chamber volume (empty volume plus volume occupied by porous material) an optimization problem can be formulated.

$$\{\widetilde{\Lambda}, \widetilde{\Psi}\} = \min_{\Lambda,\Psi} \left(- \int_{P_0}^{P_f} \frac{1}{\tilde{Q}(P, \Lambda, \Psi)} \frac{dV}{dP} dP \right) \tag{3.22}$$

such that:

$$\int_0^{V_f} \frac{dV}{\Psi(v)} - \frac{V_0}{\overline{\Upsilon}} = 0 \tag{3.23}$$

$$l_{min} \leq \int_0^{V_0} \frac{dV}{\Lambda(v)} \leq l_{max} \tag{3.24}$$

where $\overline{\Upsilon}$ is the allowable total porosity of the chamber and l_{min} and l_{max} are the minimum and maximum chamber lengths respectively. Note that $\tilde{Q}(P, \Lambda, \Psi)$ is the optimal flow rate calculated from the inner optimization of flow rate trajectory. In order to capture the effects of the varying cross sectional area and porosity, the one-dimensional model derived in chapter 2 was used. The chamber open area and porosity distribution are discretized (each with 10 sections over the entire range of chamber volume) with piecewise linear functions in order to optimize these parameters. Note that while the outer optimization uses the one-dimensional model, the inner flow trajectory optimization uses the lumped air properties model for computation speed. This calculation procedure is repeated iteratively until the chamber geometry and porosity converge to their final optimal forms. Therefore, the resulting optimal flow rate found is for the corresponding optimal chamber design.

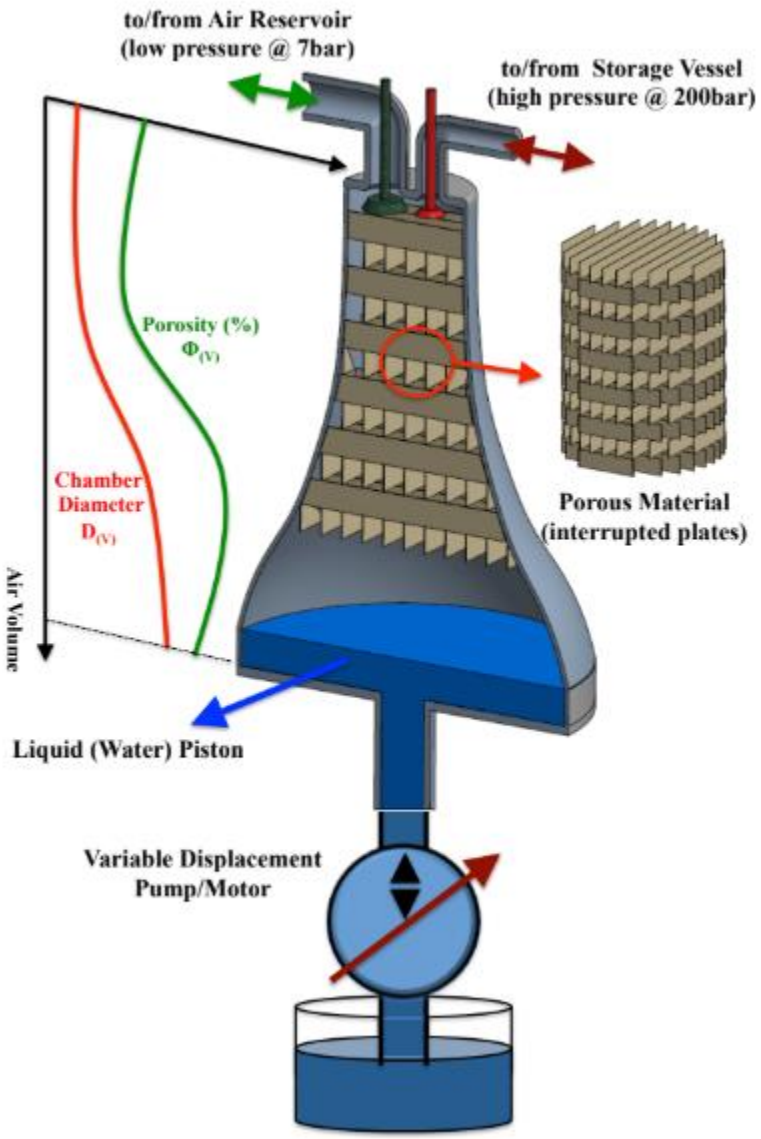

Figure 3.1: Proposed concept diagram of liquid piston air compressor/expander [9].

A number of case studies were conducted to determine how each design variable would affect the resulting power density. The results of the work produced by Saadat et al *[9, [13, [31[32,[*62]. for the optimization of power density for the proposed liquid piston compressor/expander can be summarized in the following table:

Table 3.1: Power density optimization results for different test cases. The thermal efficiency (92%) and total porosity (80%) is held constant for all cases. Here, the total chamber volume is 1875cc of which 375cc is occupied by heat exchanger material [9,[62].

Step	Porosity	Flow Rate	Shape	Chamber Length	Efficiency	Compression Time	Power Density (kW/m^3)
1	**uniform**	**constant (43cc/s)**	**uniform ($21.5cm^2$)**	70cm	**92%**	**33s**	**71.2**
2	uniform	optimal	uniform ($21.5cm^2$)	70cm	92%	10.8s	217.3
3	optimal	constant (149cc/s)	uniform ($21.5cm^2$)	70cm	92%	9.6s	245.6
4	optimal	optimal	uniform ($21.5cm^2$)	70cm	92%	3.5s	669.3
5	**optimal**	**optimal**	**optimal**	70cm	**92%**	**1.6s**	**1470**
N	optimal	optimal	narrowest ($7cm^2$)	214cm	92%	1.47s	1600
F	optimal	optimal	fattest ($78.5cm^2$)	19cm	92%	5.5s	423.6

The results produced by Saadat et al [[9,[62]. show a large increase in power density when all design variables are optimized. Please note that the narrowest chamber diameter case study showed a great increase in power density. This is due to the increased air velocity in the chamber which in turn increases heat transfer. In order for the optimization to not trend towards the trivial case of a very tall and narrow tube, a chamber height limit of 70cm was applied to the optimization. In contrast, the short and wide chamber produced the least power density when optimizing the other variables. The optimization results trend towards a wider chamber base with a tall narrow top, this can be seen in the resulting optimized design in Figure 3.2:

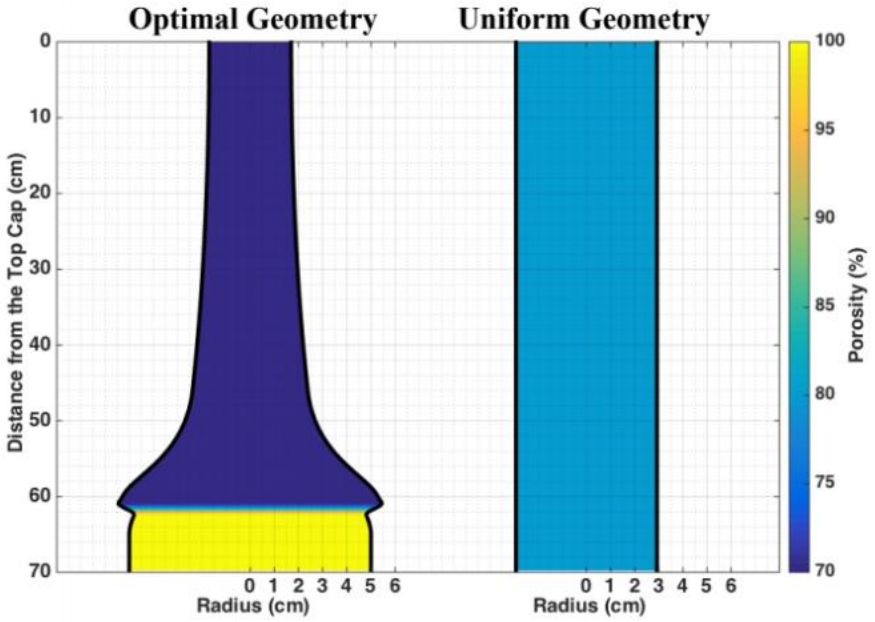

Figure 3.2: Optimal geometry of chamber with heat exchanger porosity distribution [9,[62].

The resulting porosity distribution also shows to have no heat exchanger material in the bottom of the chamber and almost all of the available heat exchanger material in the narrow chamber section. This is a result of the increased air velocity at the top of the narrow chamber section, where most heat transfer can occur. Interestingly, the bottom section requires no heat exchanger material to operate efficiently since the temperature gradient has not built up enough to facilitate heat transfer during this portion of the compression cycle. It should be noted that the optimization provided a power density increase of nearly 20 times the baseline case. The insight gained from the power density optimization provides an exceptional design to compare against when determining the most cost effective solution.

3.3 Cost Function Derivation for Optimization of Liquid Piston Compressor/Expander

In this section, a function for estimating system cost is developed for the cost optimization of the liquid piston compressor/expander. The two primary components for the variation of system cost are the chamber and the water pump/motor. The cost optimization calculates the minimum cost per system power. this will provide a design that can later be scaled to specified power levels for introduction to the market. In this study, a system power level of 5kW is specified to provide an appropriate scale for lab testing and design verification. In order to define our system, the following ratio is defined:

$$\alpha = \frac{Q_{max}}{V_{cham}} \tag{3.25}$$

here, ratio α is defined as the maximum flowrate of the water pump/motor Q_{max}, divided by the volume of compressible gas of the chamber V_{cham}. These two components of the system are what will define the performance and cost of each iteration of the optimization. Using this ratio, our cost function which determines the cost per power of each system defined by α is described as:

$$J(\alpha) = \frac{S_V + \alpha S_Q}{PD(\alpha)} \tag{3.26}$$

$$[J] = \left(\frac{[\$]}{[V]} + \frac{[Q]}{[V]}\frac{[\$]}{[Q]}\right)\frac{[1]}{\frac{[P]}{[V]}} = \frac{[\$]}{[P]} \tag{3.27}$$

the cost function J is determine by S_V, the cost per volume of the chamber, and S_Q the cost per maximum flowrate of the pump/motor. Adding the cost per volume of the

chamber to the term αS_Q will yield the cost per volume of the system defined by α. Dividing this expression by the resulting power density $PD(\alpha)$ will yield our desired system cost per power (see equation (*3.27*). The power density calculations are the same as described in section 2.2.

3.4 Estimation of System Cost

To perform a cost optimization of the proposed system, an estimation for the required cost of neccesary materials is needed. This estimate for the overall system cost is broken down into two separate cost factors. One factor pertains to the material cost of the pressure vessel itself, while the other pertains to the cost of the hydraulic pump/motor. The chamber cost per volume factor S_V incorporates the design of a pressure vessel given some design constraints. The resultant chamber geometry for each optimization iteration is calculated. This provides the total volume of the chamber material and porous insert material required to build this iteration of the system. Simple cost per volume (cost density) factors for the chamber material (stainless steel) and porous material insert (ABS plastic) are then used to calculate the total chamber cost. Note that this is purely material cost and does not incorporate manufacturing cost. The cost per maximum pump/motor flowrate term S_Q estimates the cost of the pump/motor given the maximum available flow of the component. This is calculated from an average value of pump/motor cost from hydraulic component manufacturers. The derivations for each of these terms are outlined in this section.

Derivation of chamber cost per volume factor - S_V:

The chamber cost per volume factor S_V was calculated by determining the amount of material needed for a pressure vessel consisting of S31600 stainless steel designed to withstand a maximum internal pressure, P_{max} (with a safety factor of 4), while containing both the volume of the compressible gas and the heat transfer material insert. To benefit

from the power density results shown in Table 3.1 with respect to narrow cross sectional chambers, a constant cross sectional area for the chamber is assumed while also relaxing the height constraint to a maximum of 3.3m (the height of the lab's ceiling). This height restriction was imposed since the goal is to eventually fabricate the resultant system in our lab for testing. However, the results of this analysis generalize to less restrictive situations such as larger MW power plants. The assumption of a thin-walled pressure vessel is also made for ease of calculation. This assumption is valid for a vessel radius that is greater than 5 times the thickness of the outer wall. Pressure vessel radius is calculated by using the specified height and volume (volume of gas and heat transfer material) enclosed. The primary mode of failure for a thin walled pressure vessel is the hoop stress, σ_h, created by the interal pressure pushing against the cylinder wall. Since the pressure vessel is assumed to include welded endcaps, the axial stress created by the pressure acting on the endcaps must also be included. Therefore, the thickness, t, of the pressure vessel must be sufficient to withstand the equivalent stress formulated from the two principle stresses within a safety factor. Following the von Mises criterion, a maximum equivalent stress given by the two principle stresses is described by:

$$\sqrt{{\sigma_1}^2 - \sigma_1\sigma_2 + {\sigma_2}^2} \leq \sigma_y \tag{3.28}$$

The criterion states that failure occurs when the energy of distortion produced by the hoop stress (σ_1) and the axial stress (σ_2) reaches the same energy for yield/failure in uniaxial tension. For a thin walled pressure vessel, the hoop stress and axial stress are described by:

$$\sigma_1 = \frac{P_{max} \cdot r_c}{t} \tag{3.29}$$

$$\sigma_2 = \frac{P_{max} \cdot r_c}{2t} \tag{3.30}$$

where notably the hoop stress, σ_1, produced by internal pressure P_{max} is twice the amount of axial stress, σ_2, produced. Substituting these stress definitions into the von Mises equation and rearranging, the required thickness t of the pressure vessel can be calculated:

$$\left(\frac{P_{max} \cdot r_c}{t}\right)^2 - \frac{{P_{max}}^2 {r_c}^2}{2t^2} + \left(\frac{P_{max} \cdot r_c}{2t}\right)^2 = \left(\frac{\sigma_y}{SF}\right)^2 \tag{3.31}$$

$$t = \sqrt{\frac{3}{4}\left[\frac{P_{max} \cdot r_c}{\left({\sigma_y}/{SF}\right)}\right]^2} \tag{3.32}$$

where SF is the safety factor for the calculation and with the radius subject to the thin walled pressure vessel restriction:

$$r_c > 5 \cdot t \tag{3.33}$$

the flat end caps considered for this pressure vessel also require calculation for the required thickness given by ASME code UG-34 from section VIII Division I:

$$t_{endcap} = 2r_c \cdot \sqrt{\frac{C \cdot P_{max}}{\left({\sigma_y}/{SF}\right) \cdot E}} \tag{3.34}$$

where E is the joint efficiency for the pressure vessel, this changes with how the endcap is attached to the cylinder (i.e. welded seam efficiency) and C is a constant ($C = 0.33$). The volume of the cylinder is calculated from the required thickness of the pressure vessel and the specified geometry from the optimization. The volume of the endcaps are also calculated to reach the outer diameter of the cylinder and to have the required thickness for pressurization. The total volume of the pressure vessel material for the specified system is then:

$$V_{cyl} = h_c \pi((r_c + t)^2 - {r_c}^2) \tag{3.35}$$

$$V_{endcap} = t_{endcap} \cdot (\pi(r_c + t)^2) \tag{3.36}$$

with total cost for the pressure vessel, $Cost_{Cham}$, obtained by calculating material volume, material density (ρ_{ABS} for heat exchanger and ρ_{Cham} for chamber material), and cost density of both materials ($\rho_{cost,Cham}$ for chamber and $\rho_{cost,ABS}$ for Heat exchanger material):

$$\begin{aligned} Cost_{Cham} = (V_{cyl} + 2 \cdot V_{endcap}) \cdot \rho_{Cham} \cdot \rho_{cost,Cham} \\ + V_{abs} \cdot \rho_{ABS} \cdot \rho_{cost,ABS} \end{aligned} \tag{3.37}$$

therefore, the chamber cost per volume term S_V [\$/m^3] is obtained by dividing this cost by the total amount of compressible gas:

$$S_V = \frac{Cost_{Cham}}{V_{cham}} \tag{3.38}$$

note that the amount of material needed to contain the internal pressure of the pressure vessel increases with the radius. This is due to increased surface area for the pressure to act on when increasing radius. To drive the cost of the pressure vessel down, the

geometry trends towards tall narrow tubes. This in combination with the increase in power density for narrow tubes make the cost optimal solution trend towards this type of geometry.

Derivation of pump/motor cost per maximum flow S_Q:

The last term relating to our system cost function has to do with the maximum flowrate of the pump/motor. Pump/motor cost can be estimated by using an average displacement density factor, ρ_{disp}, the operational speed, ω, and the average cost density $\rho_{cost,Q}$. The average displacement density factor ρ_{disp} is defined as the average pump/motor displacement per pump/motor volume for commercially available pump/motors. Similarly, the average cost density $\rho_{cost,Q}$ is the average cost of commercially available pump/motors per kilogram of mass. The factor $\rho_{cost,Q}$ was supplied via an industry partner and was obtained by averaging the pump/motor cost per kilogram across the industry partner's entire catalog of commercially available pump/motor products. These values were obtained via hydraulic manufacturers and can be used to calculate the cost per flowrate of the pump:

$$S_Q = \left(\frac{1}{\rho_{disp}}\right) \cdot \left(\frac{1}{\omega}\right) \cdot \rho_{cost,Q} \tag{3.39}$$

$$\left[S_Q\right] = \left[\frac{1}{\frac{m^3/_{rev}}{Kg}}\right]\left[\frac{1}{rev/_s}\right]\left[\frac{\$}{Kg}\right] = \left[\frac{\$}{m^3/_s}\right] \tag{3.40}$$

all constant values used in the cost function are shown below in Table 3.2.

Table 3.2: Constant parameter descriptions and values used in system cost function calculations.

Parameter	Description	Value	Unit
P_{max}	Final Air Pressure	200	bar
σ_{yield}	Yield Stress	205	MPa
E	Joint Efficiency Factor	0.8	-
SF	Pressure Vessel Safety Factor	4	-
ρ_{Cham}	Density of PV Material (316 Stainless Steel [S31600])	8027	Kg/m^3
$\rho_{cost,Cham}$	Cost (USD) per Kilogram of PV Material (316 Stainless Steel [S31600]) [60]	4.115	$/Kg
ρ_{ABS}	Density of Heat Transfer Material (ABS Plastic)	940	Kg/m^3
$\rho_{cost,ABS}$	Cost (USD) of Heat Transfer Material (ABS Plastic) [61]	20	$/Kg
ρ_{disp}	Pump/Motor Displacement per Kilogram (2cc/Rev/Kg)	2e-6	m^3/Rev/Kg
$\rho_{cost,Q}$	Pump/Motor Cost ($USD) per Kilogram	22	$/Kg
ω	Pump/Motor Speed (1800 RPM)	30	Rev/s

Now that the cost function is defined, the optimal α-value (maximum pump/motor flowrate normalized by chamber volume) that results in the minimum cost of the system can be found. To complete this, a simple blind search was conducted by calculating the cost/kW of a range of α-values to find which α-value correlated to the minimum cost. The ratio α was defined in equation (*3.25* as the ratio of maximum available flowrate of pump divided by the volume of compressible gas. A blind search was chosen for this method because the optimal flow calculator, which is responsible for generating the flow trajectory that results in the maximum power density (and thus minimum cost) for a given α-value, is computationally expensive. Therefore selecting a finite range of α-values will

reduce the number of optimal flow calculations compared to a gradient search method while still providing insight into the effect the α-value has on the cost function. Figure 3.3 shows the optimal flow trajectories for a range of α-values plotted against volume of air:

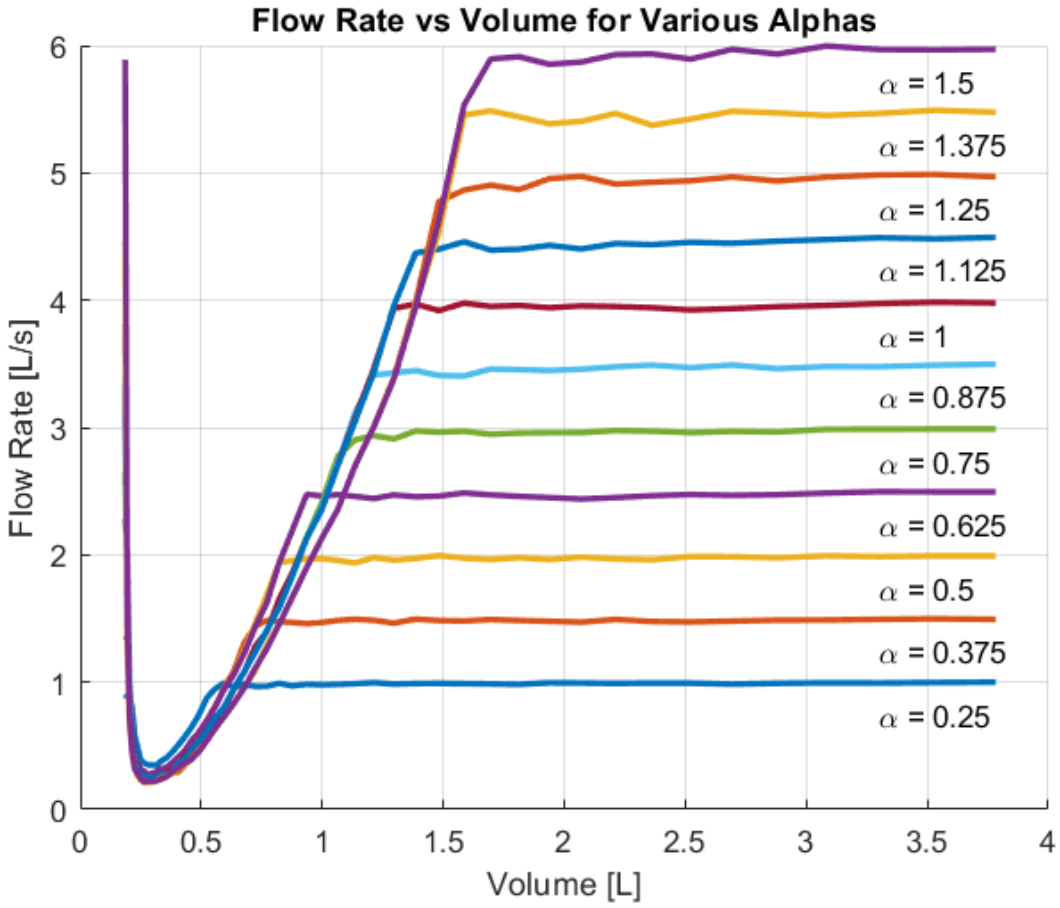

Figure 3.3: Optimal flow trajectories plotted against air volume for a range of α-values.

The optimal flow trajectories follow a similar path but with the key difference that the lower α-values are operating at maximum flowrate for a longer portion of the compression cycle. This is expected since the pump will have to operate at a higher average displacement when the maximum flowrate is small compared to the volume of comressible gas. However this will in turn take more time for the compression, which results in a lower power density for the lower α-values. Thus there is a trade off between

a high flowrate pump (increases cost) which allows a high power density (lowers cost) as compared to a low flowrate pump (decreases cost) but also decreases power density (increases cost). Figure 3.3 also shows how maximum flowrate of each trajectory dips as the volume becomes small, before rapidly increasing. As the α-value increases, this dip begins occuing at increasingly larger volumes. This occurs due to the fast compression rate of the large α-values (i.e. large maximum available flowrate) which causes the air to heat up quickly. The flowrate must then reduce to slow the compression rate to allow for heat transfer to occur. The cost function results of the blind search are shown in Figure 3.4. Here a constant volume of air (4 liters) is assumed while the pump maximum flowrate is increased to achieve different α-values. It shows that the system cost reduction at low α-values outweighs the increase in power density achieved at higher α-values.

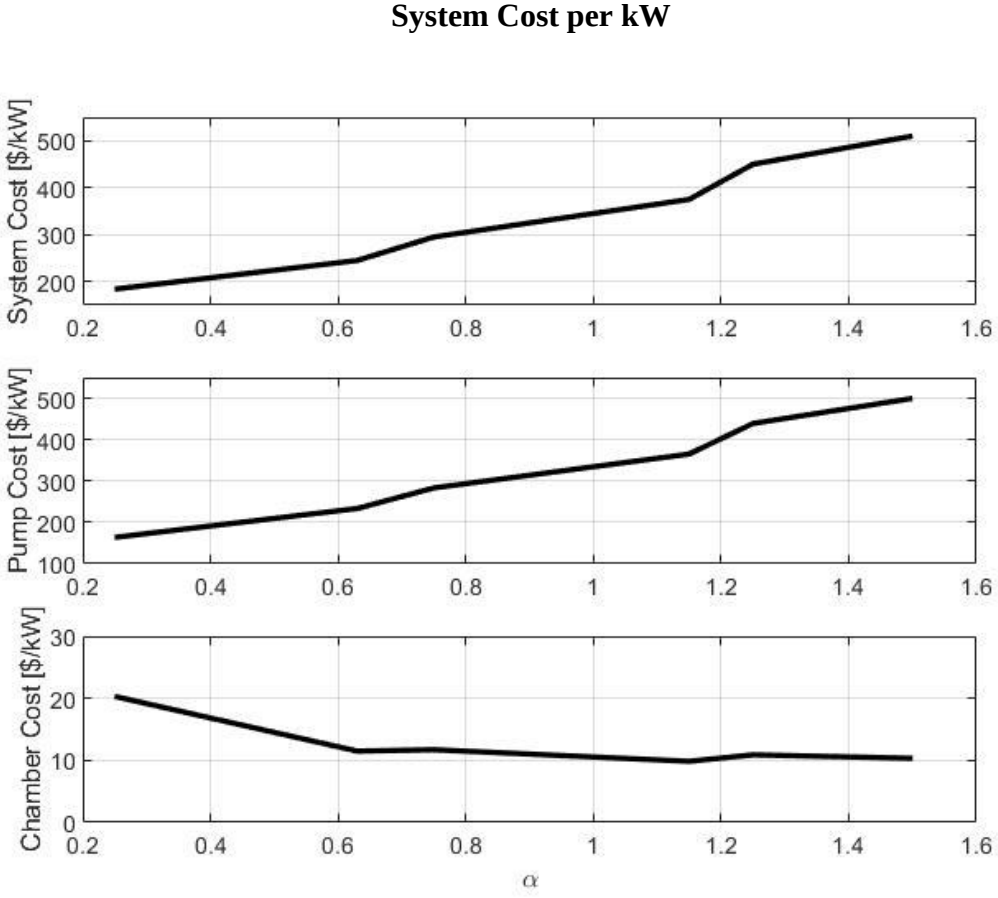

Figure 3.4: System cost/kW (top), pump cost/kW (middle), and chamber cost/kW (bottom) for a given α-value. Constant parameters include: volume of gas (4 L), chamber diameter (4.3 cm) and height (2.75 m), Minimum cost ($184) achieved at α = 0.25.

Table 3.3: Tabulated results of system cost for power density optimized design and cost optimized design.

Opt. Method	**Eff.**	**Power Density** $\boldsymbol{kW/m^3}$	$\boldsymbol{\alpha}$**-value**	**System Cost per kW** $\left[\frac{\$_{sys}}{kW}\right]$	**Pump Cost per kW** $\left[\frac{\$_{pump}}{kW}\right]$	**Chamber Cost per kW** $\left[\frac{\$_{cham}}{kW}\right]$
Power Density: Diameter = Opt. Height = 0.70 m $V_{gas} = 1500cc$ Pump Disp. = 36cc/rev	92%	1470	0.73	$248.89	$181.76	$67.13
Cost: Diameter = 4.7 cm Height = 2.3 m $V_{gas} = 4000cc$ Pump Disp. = 33cc/rev	92%	479	0.25	$227.53	$191.02	$36.51
Cost: Diameter = 4.3 cm Height = 2.75 m $V_{gas} = 4000cc$ Pump Disp. = 33cc/rev	92%	559	0.25	$183.99	$163.69	$20.30

The results shown in Figure 3.4 and Table 3.3 indicate a number of insightful properties of a more cost effective compressor/expander system:

1. Cost effective designs favor systems that obtain a small pump/motor flowrate relative to chamber volume (i.e. small α-values). However, this is at the expense of system power density. While driving down the chamber cost does help reduce the total system cost, the cost of the pump/motor is still the vast majority of the total system cost. Further reduction of the maximum pump/motor flowrate will result in large overall system cost reduction.

2. Tall, small diameter chambers are both cost effective (material wise) and greatly increase thermal efficiency.

3. The increase in thermal efficiency of slender chambers and increased compression time of small α-values allow the pump/motor to approach a constant maximum flowrate during the entire cycle. This means a fixed displacement pump (constant flowrate) can be substitued for the variable displacement pump without much change in efficiency, thus reducing cost.

It is important to note that our laboratory scaled system design has a target power level of 5kW and an imposed height restriction due to our specific laboratory dimensions. These restrictions enter into the results by limiting the achievable power density of the cost optimized system. For example, if the height restriction was relaxed, the system design would trend to a taller pressure vessel. This would increase efficiency (i.e. power density) while reducing pressure vessel material cost. In general, when scaling these results up to MW power plant scales, a similar height restriction (although much taller) would be imposed for practicality purposes. Therefore the design will still trend towards what the results in this section show when optimizing for sytem cost.

3.5 Integration of Flow Intensifier

The information gathered in section 3.3 has provided guidance towards a more cost effective compressor/expander system design. It was discovered that many benefits come with lower α-values and slender chambers. The cost benefit that comes with lower α-values greatly out weighs the increased cost caused by dropping system power density. This trend held true until the α-value was so low that the desired thermal efficiency could not be reached. When the α-value is significantly low, the pump/motor can run continuously at maximum flowrate and still achieve a thermal efficiency greater than our desired 92%. This implies that with the correct chamber geometry, a constant flow rate can be sufficient for achieving desired thermal efficiency. This is very beneficial since variable displacement pump/motors are much more costly than fixed displacement pump/motors. While this is a great step in reducing cost and complexity of the system, it comes at the price of decreasing power density. Table 3.3 shows that the power density decreased by 3 times while system cost is reduced by 25%. With the goal being to design an energy storage device, high power density is still a desired feature of the system. It is now desired to reach lower α-values while still maintaining a power dense system.

In the search for smaller pump size, an interesting system component came to light *[43*]. This component can effectively amplify a pump/motor output without increasing the physical maximum flowrate of the pump. This component, called a flow intensifier, would be an ideal addition to the cost optimization process as it effectively allows us to reach lower α-values while also decreasing compression time (thus increasing power density). The shaded region shown in Figure 3.5 depicts the implementation of a flow intensifier into the system:

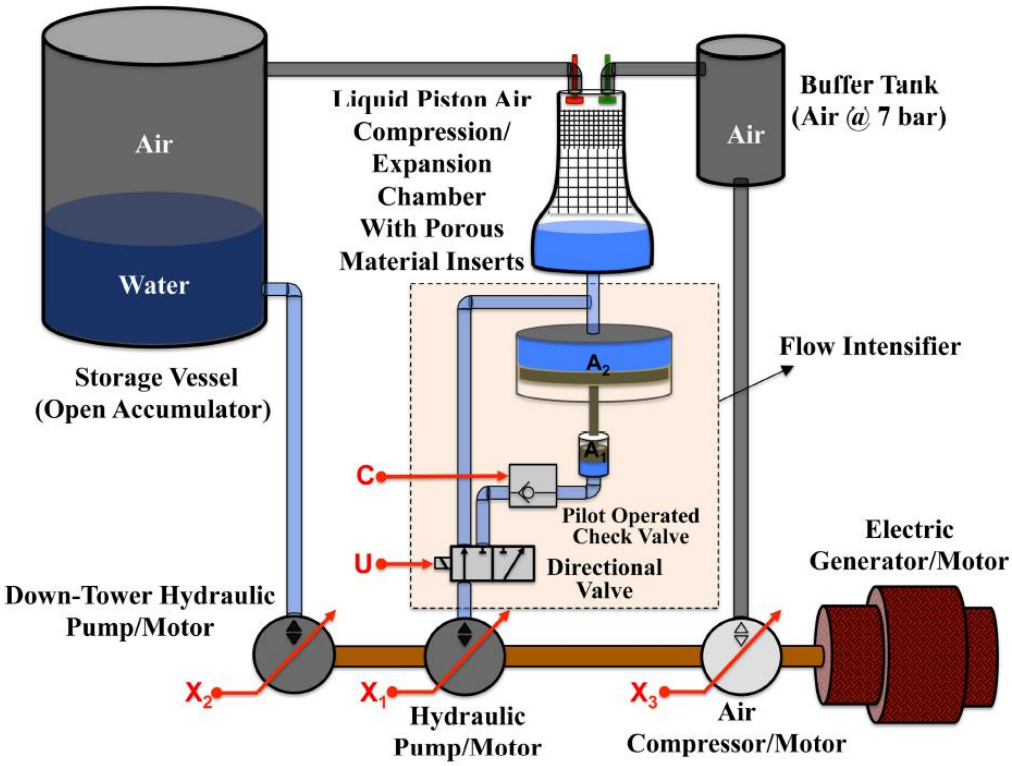

Figure 3.5: Flow intensifier (shaded region) integrated into CAES system [43].

the flow intensifier amplifies flow by diverting output flow from the pump/motor (X_1) through directional control valve (U) and into a hydraulic piston chamber with piston area (A_1) during intial compression. The end of the piston is a attached to a larger piston area (A_2) which then moves upwards when the smaller chamber is pressurized. Since $A_1 < A_2$, the volume change in the smaller chamber is amplified by the ratio of the piston head areas A_2/A_1. So during initial compression, the flowrate entering the compression chamber is $Q_2 = (A_2/A_1) \cdot Q_1$, where Q_1 is the output flowrate of the pump. However, since the pressure inside the compression chamber is acting on a larger piston area, this pressure is amplified on the pump outlet side. The pump will see a pressure $P_1 = (A_2/A_1) \cdot P_2$ where P_2 is the pressure inside the chamber. At some pressure P_{switch}, the directional valve (U) will stop diverting flow into the flow intensifier and switch to send flow directing into the chamber itself. The switching pressure determines how long the output flow of the pump will be amplified during the compression cycle. After this

switch occurs, the volume of liquid inside the smaller chamber is locked in place while the rest of the cycle completes [43].

During expansion, the operation is reversed. First liquid is drawn out of the compression chamber until pressure drops and the liquid level is slightly above the connection for the hydrualic line connecting to the pump/motor. Once the switching pressure is achieved, the flow is then directed out of the smaller piston area chamber and the flow intensifier recedes to the initial position, ready for the next cycle. Using this method, the output flowrate of the pump/motor can be amplified during the beginning/end of a cycle which decreases cycle time. The locking feature of the flow amplifier also ensures that the pump/motor never experiences pressures above the maximum chamber pressure. An expample compression flow trajectory can be seen in Figure 3.6:

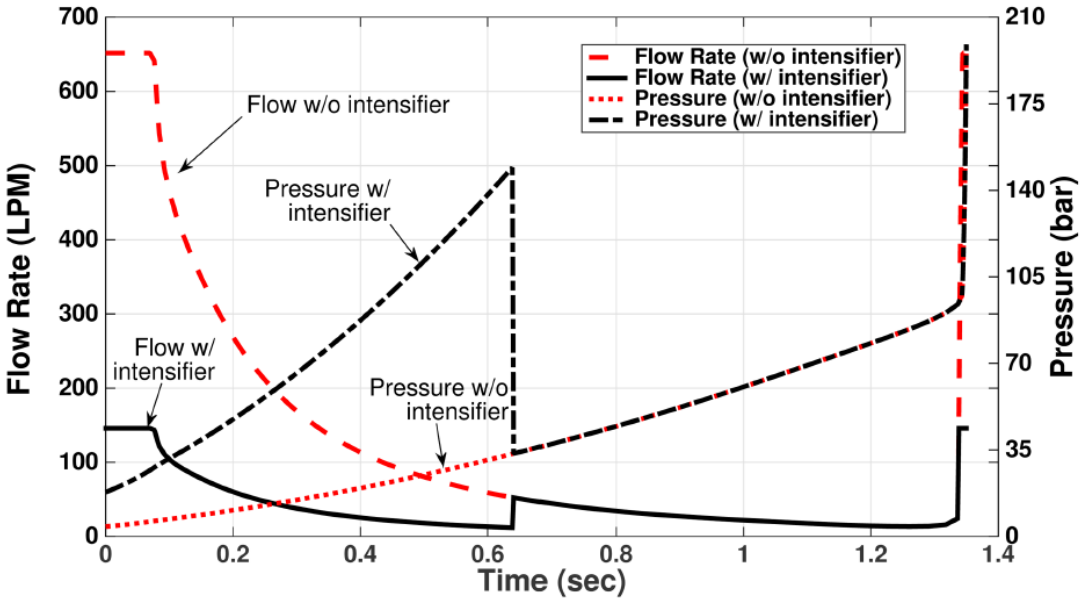

Figure 3.6: Effective pump output flow rate and pressure during compression cycle for optimal flow rate trajectory [43].

here you can see the flow intensifier amplify the flow rate of the pump during the initial compression stage while the pump side pressure builds. Once the switching pressure

reaches the specified value, the pump output flow diverts to entering the chamber and thus resumes the origianl optimal flow trajectory. Utilizing this technology, there is a possibility of increasing the power density of the system while maintaing a small α-value.

Incorporating the flow intensifier into the compressor/expander system will add additional parts and compexity. Figure 3.5 shows an additial double ended hydraulic piston and various valves in order to implement the flow intensifier. However, if you recall the optimal chamber shape depicted in Figure 3.2, there is a possibilty to merge the flow intensifier inside the flow intensifier. The optimal shape resembles a gourd, with the optimal porosity distrubution have all heat transfer material reside in the top narrow section. By combining the flow intensifier with the power density optimal shape and porosity (see Figure 3.7), a solution exists that utilizes all of the design benefits. Proposed in Figure 3.8 is a two stage compression/expansion chamber that integrates the power density optimization results with the flow intensifier concept.

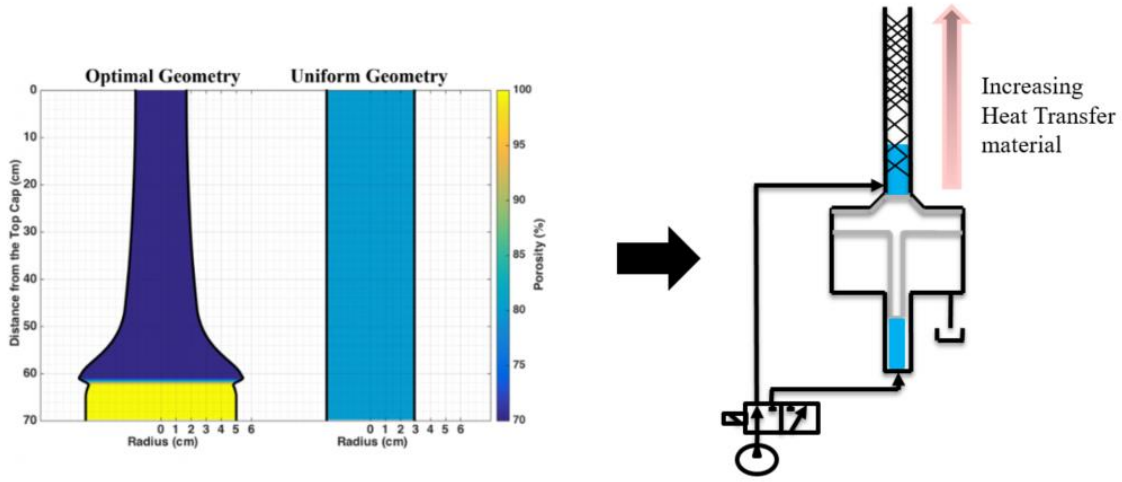

Figure 3.7: Combinition of power density optimization results with flow intensifer.

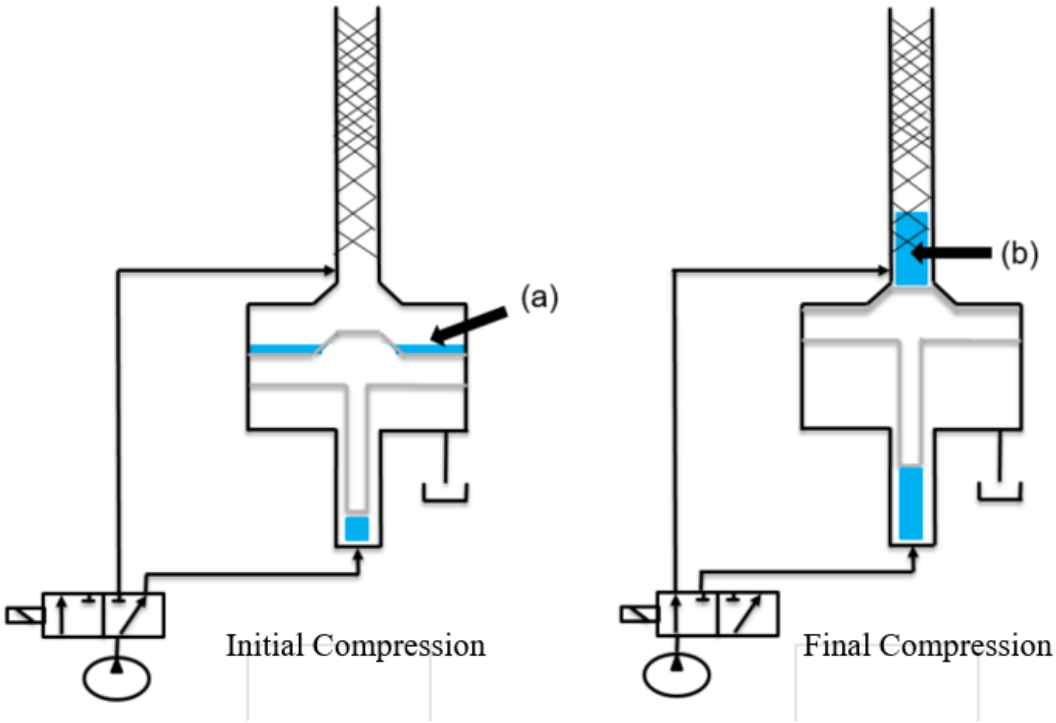

Figure 3.8: Integrated design part way through initial compression (left) and final compression (right).

The proposed compressor/expander design operates in a manner similar to the flow intensifer but with a few key differences. During the initial compression, the output flow from the pump is diverted into the smaller piston head area chamber of the double sided piston as before. This will then amplifiy the flow output of the pump by increaseing the rate at which the volume of gas in the compression chamber (large piston head area side of double sided piston) decreases by the ratio of the piston head areas. Notice at (a) in Figure 3.8 that there is a thin film of liquid covering the large piston head. This will act as a liquid seal during compression which greatly improves sealing quality compared to convential gas seals. One of the reasons for using a liquid piston was the ability for the liquid to traverse through the heat transfer material. However, leveraging the results of the power density optimization shows that the distrubution of heat transfer material is not neccesary during the intial stage of compression. Using this result allows us to distrubute the heat transfer material in the second stage of comrpession and utilize the empty volume in the initial compression stage to incorporate the flow intensifier mechanical

piston. Comparing the initial compression stage geomtry to the power density optimized geometry, a justification for the large cross sectional area of flow intensifier can be made since the previous study deemed the heat transfer insignificant during this compression stage. By designing the volume displaced by the initial compression to align with the switching pressure, the pump will begin to divert flow directly to the final compression stage once the mechanical piston has seated and sealed at the end of the stroke.

Once the flow intensifier piston is seated, the switching valve will then divert flow into the narrow tube section for final compression. Recall that the cost optimization for the chamber geometry favored smaller chamber radii. With this design, the piston will be locked in place and sealed after the initial compression stage, with the internal pressure only being the switching pressure divided by the area ratio of the intensifier. Thus the cost calculations for the initial compression stage pressure vessel will be significantly less as it only has to be design to withstand a fraction of the final pressure. Continuing with the cycle, point (b) shows the thin film of liquid on top the large piston head has rose into the narrow tube and is above the inlet orifice, ready for final compression. This will mitigate the liquid-air interface from experiencing undesirable mixing. The final compression stage then commences using the outlet flow of the pump, raising the liquid piston. In this stage, all available heat transfer material is distrubuted while also having the added benefit of the narrow tube for aditional heat transfer. This stage is when heat transfer is paramount to achieve the desired thermal efficiency.

Expansion will reverse this process by first depleting liquid volume from the final compression stage narrow tube until the liquid level is just above the inlet/outlet. The switching valve will trigger and then flow will be taken form the small piston head area chamber of the flow intensifier until the cycle is complete.

The possible benefits achieved by this design approach are numerous. In review, this design benefits from:

1. The ability to take advantage of the flow intensifier in order to reach lower α-values and drastically reduce cost of the pump/motor, the most expensive component.

2. Seperating the stages of compression allows for distrubution of heat exchanger material to reside where it matters most, increasing thermal efficiency.

3. Amplified output flow rate greatly increases power density at low α-values while maintaining power density for fast compression/expansion.

4. The high thermal efficiency capabilities paired with low α-values allow for constant flow rate pumps, greatly reducing cost and complicated optimal flow trajectories.

5. Lower initial compression stage chamber pressure reduces neccesary material cost for pressure vessel.

6. The large initial compression stage volume is short and fat, allowing all the benefits of a narrow tube for the final compression stage while remaining in a small package, reducing overall height.

3.6 Flow Intensifier Design Cost Optimization

This section details the modifications made to the cost function in order for a cost optimization to be conducted to optimize the design variables of the flow intensifier system. With the new addition of the flow intensifier into the system design, a new set of design variables must now be optimized. The cost function resembles the same form, however the chamber cost and the power density terms now vary with the design variables. Let $\bar{\sigma}$ be a set of design variables (see Figure 3.9) such that:

$$\bar{\sigma} = \{\alpha, P_{switch}, \gamma, Q_{max}\} \tag{3.41}$$

where α is the ratio of maximum pump flowrate Q_{max} (out of the pump) divided by the volume of compressible gas, V_{cham}, within the chamber, P_{switch} is the switching pressure of the flow intensifier, $\gamma = A_{FI}/A_{min}$ (such that $\gamma \geq 1$) is the area ratio of the flow

intensifier, and Q_{max} is the maximum flow rate of the pump/motor. The cost function is now defined as:

$$J(\bar{\sigma}) = \frac{S_V(\bar{\sigma}) + \alpha S_Q}{PD(\bar{\sigma})} \tag{3.42}$$

the addition of the flow intensifier will only affect the $S_V(\bar{\sigma})$ chamber cost per volume and the $PD(\bar{\sigma})$ power density terms in the cost function. The S_Q term is still constant and accounts for the cost of the pump/motor as before.

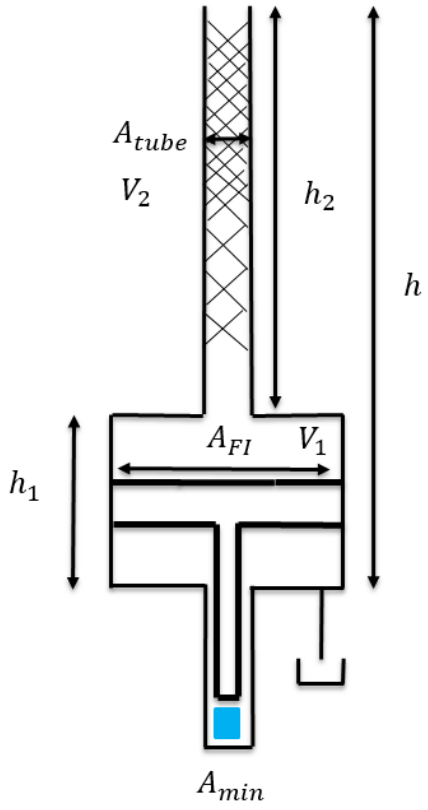

Figure 3.9: Flow Intensifier design diagram.

In order to evaluate and optimize the cost function $J(\bar{\sigma})$ in ((3.42), a complete description of the geometry and performance of a system defined by design variables $\bar{\sigma}$ must be derived. The geometry calculations regarding the amount of material neccesary

to build the chamber are similar to that in Section 3.3. However here, the chamber is split into two separate cylindrical pressure vessels for geometry calculations. The final pressure vessel will then be constructed by connecting the lower pressure vessel (containg the flow intensifier) to the upper pressure vessel (containing the heat echanger material). To begin, some assumptions must be made regarding the geometry calculations of the initial compression stage chamber. In order to calculate A_{FI}, which provides the radius of the intial compression stage pressure vessel, an assumption is made that A_{min} is constant. Therefore:

$$A_{FI} = \gamma \cdot A_{min} \tag{3.43}$$

where $A_{min}$was chosen to be the smallest available piston head area that did not suffer from sealing issues. This assumption is justified since it is desirable for the flow intensifier to operate effectively and still achieve a minimal pressure vessel radius for the sake of cost/size. Another assumption made is that the volume displacement required by the flow intensifier would be calculated using the isothermal compression of an ideal gas. For example, say the initial gas state was represented by P_0V_0, then the volume V_1 displacement required to achieve the specified switching pressure would be:

$$V_1 = V_0 - \frac{P_0V_0}{\left(\frac{P_{switch}}{\gamma}\right)} \tag{3.44}$$

this assumption allows for the estimation of the volume V_1, from which $h_1 = V_1/A_{FI}$. With these geometric parameters the cost can be calculated for the flow intensifier initial compression stage chamber. The second stage compression chamber is calculated as before by obtaining the chamber geometry required to compress the remaining gas volume to the maximum chamber pressure P_{max}. Once these values are calculated,summing the cost of both the initial compression stage chamber and the final

compression chamber with provide the total cost of the chamber. Dividing the total chamber cost by V_{cham} will provide the formulation of $S_V(\bar{\sigma})$.

The findings of the initial cost optimization are used to make an important assumption regarding the power density calculations. Previously, the optimization desired to maximize the power density by calculating an optimal flow trajectory. Increasing the power density was theorized to provide a significant cost benefit. However, the findings show that the increase in power density achieved by incorporating this type of flow control requires a high maximum flowrate variable displacement pump which adds significant cost. In fact, as the chamber geometry is refined and higher thermal efficiencies are reached, the optimal flow rate calculation converges to a constant maximum flowrate for the entire trajectory. This information allows us to make the assumption that the power density calculations will use a constant flow rate, therefore eliminating a very computationally expensive piece of the cost function calculation as well as an expensive variable displacement pump. Of course now with the implementation a flow rate intensifier, the maximum flowrate of the pump will be augmented by the flow intensifier ratio $\gamma = A_{FI}/A_{min}$. The increased flowrate will continue until the pressure inside the chamber reaches the switching pressure P_{switch}, at which point the flow rate will return to the specified value Q_{max}. A sample input for the power density calculations using this simplified flow input can be seen in Figure 3.10 below:

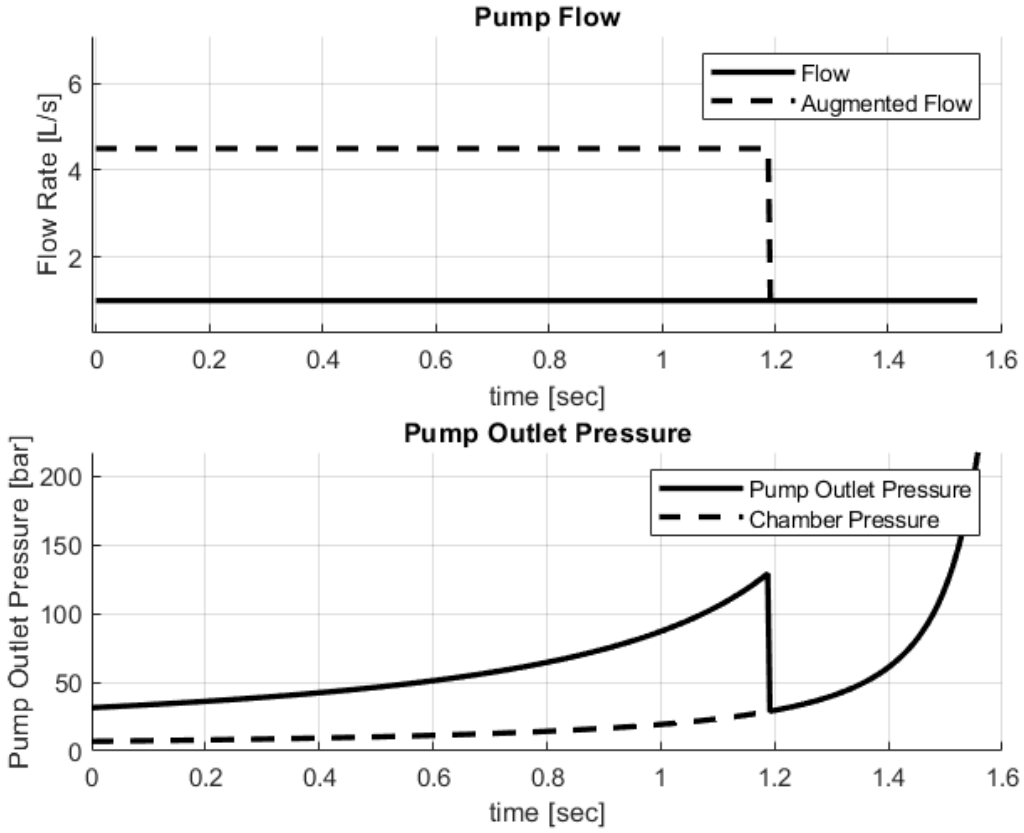

Figure 3.10: Constant flow rate trajectory (top) and pressure (bottom) with flow intensifier implementation. Design parameters: $Q_{max} = 1\ L/s$, $\gamma = 4.5$, $P_{switch} = 140\ bar$, $\alpha = 0.25$.

the simplification made to the flow trajectory omits the very costly optimal flow trajectory calculation and greatly reduces computation time for each iteration. Therefore, an improved optimization can be performed on the cost function in order to refine the system design variables. A gradient search method was used to minimize the cost function with respect to the set of design variables $\bar{\sigma}$. To perform this, the gradient of the cost function must be calculated numerically by perturbing each design variable and quantifying how the cost of the system was affected.

$$\bar{\nabla}J(\bar{\sigma}_i) \approx \begin{bmatrix} \dfrac{J(\bar{\sigma}_i) - J(\bar{\sigma}_{i-1})}{\sigma_{i,1} - \sigma_{i-1,1}} \\ \vdots \\ \dfrac{J(\bar{\sigma}_i) - J(\bar{\sigma}_{i-1})}{\sigma_{i,n} - \sigma_{i-1,n}} \end{bmatrix} \tag{3.45}$$

Here $\sigma_{i,1}$ represents the first design variable in the vector $\bar{\sigma}_i$, and $\sigma_{i,n}$ represents the last design variable in the vector $\bar{\sigma}_i$. This expression perturbs the cost function $J(\bar{\sigma}_i)$ in each direction of the design variables. $\bar{\nabla}J(\bar{\sigma}_i)$ represents a vector within the design space that deterimines how to change each design variables in order to increase the cost function. To do the opposite of this, the next iteration of the gradient calculation will have modified design variables obtained by:

$$\bar{\sigma}_{i+1} = \bar{\sigma}_i - \Gamma_i \bar{\nabla}J(\bar{\sigma}_i) \tag{3.46}$$

where Γ_i is a scaling factor that determines how much the design variables are changed in the direction of the gradient via its magnitude This term is then subtracted off the previous design variables to go in the direction of decreasing cost. The scaling method is known as the Barzilai-Borwein method of steepest decent [44] and is calculated via:

$$\Gamma_i = \frac{(\bar{\sigma}_i - \bar{\sigma}_{i-1})^T [\bar{\nabla}J(\bar{\sigma}_i) - \bar{\nabla}J(\bar{\sigma}_{i-1})]}{\|\bar{\nabla}J(\bar{\sigma}_i) - \bar{\nabla}J(\bar{\sigma}_{i-1})\|^2} \tag{3.47}$$

calculating the gradient each iteration requires one power density simulation for each design variable. This becomes quite costly especially as the cost function nears its minimum and the design variables scale less and less each iteration. In order to speed this up further, it is possible to reduce the amount of times the gradient is calculated by continuing to change the design variables in the direction of the gradient until the cost function derivative changes sign (i.e. has stopped decreasing and started to increase).

This only requires one power density simulation for each iteration until the gradient must be recalculated, reducing the number of time consuming simulations by four for as long as the cost function continues to decrease. The algorithm will continue this method of minimization until the cost function gradient is within a specified tolerance.

Just like in the precedure for optimizing power density, a constraint must be placed on the optimization that ensures that the thermal efficiency is close to our desired efficiency within a tolerance. This can be achieved through the use of the Lagrange Multiplier method that previously was used for the optimal flow calculation.
The results of the flow intensifier cost optimization design variables can be seen in Table 3.4 as well as the geometric variables refering to the diagram in Figure 3.9.

Table 3.4: Optimal design variables and resulting system geomtry specifications. Total height specified as $h = 120\ cm$.

Parameter	**Value**	**Unit**
α	0.5147	1/s
P_{switch}	161.63	bar
γ	4.685	-
Q_{max}	0.9	L/s
h_1	16.66	cm
h_2	103.34	cm
$dia(A_{FI})$	10.31	cm
$dia(A_{tube})$	2.95	cm
V_1	1.4	L
V_2	0.358	L

The optimized design parameters produced an α-value ($\alpha = 0.51, \$62.91/kW$) that is larger than the previous cost optimal case without the flow intensifier ($\alpha = 0.25, \$183.98/kW$). Increasing the apparent flowrate of the pump via the flow intensifier allowed the system to reach a high enough power density to reduce the effects of the

pump cost. Note that this α-value is still lower than the previous power density optimized case ($\alpha = 0.73, \$249.89/kW$). The switching pressure and flow intensifier ratio are close to the optimal values predicted in [43]. These correspond to the volume of the flow intensifier V_1 to consist of about 80% of the compressible gas volume while the high heat transfer capable volume V_2 makes up the remaining 20%. This result highlights the importance the final compression stage has on heat transfer while the initial stage can compress a large volume very quickly without much effect on efficiency. Due to the small diameter of the final stage, most of the available chamber height is located here, while the flow intensifier is relatively compact.

The resulting air temperature during the compression for the zero-dimensional model used in the optmization is plotted with the one-dimensional model for verification in Figure 3.11. Notice at time $t{\sim}0.3s$ that the temperature has a distinct decrease. This is attributed to the flow intensifier completing the initial compression and the flowrate then decreasing during the final stages of compression. Heat transfer is also greatly improved during the final stage of compression which also contributes to the drop in temperature. Overall good agreement is found between the two modeling methods.

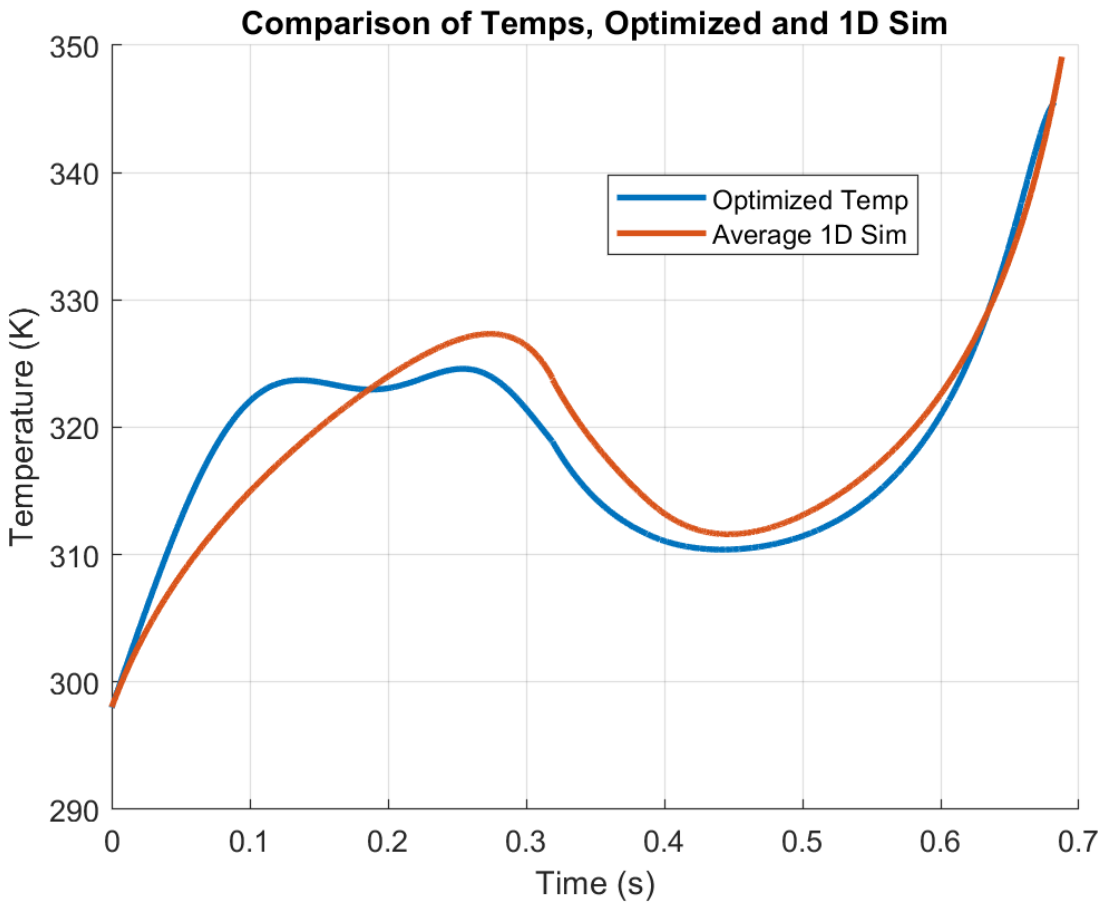

Figure 3.11: Average one-dimensional model and zero-dimensional model air temperature results.

The one-dimensional model shows the variation in temperature within the chamber. A subset of partitions are plotted in Figure 3.12 to show this variation. Note how most of the partitions are near the zero-dimensional model predictions with the exception of the chamber endcap. This node is significantly higher than the zero-dimensional model which is expected. Recall that this node does not include heat transfer to the endcap in the one-dimensional model. This temperature does briefly exceed the melting point for the ABS plastic material used for the heat exchanger insert. An alternative material with a higher melting point might be necessary for this small section of compression chamber.

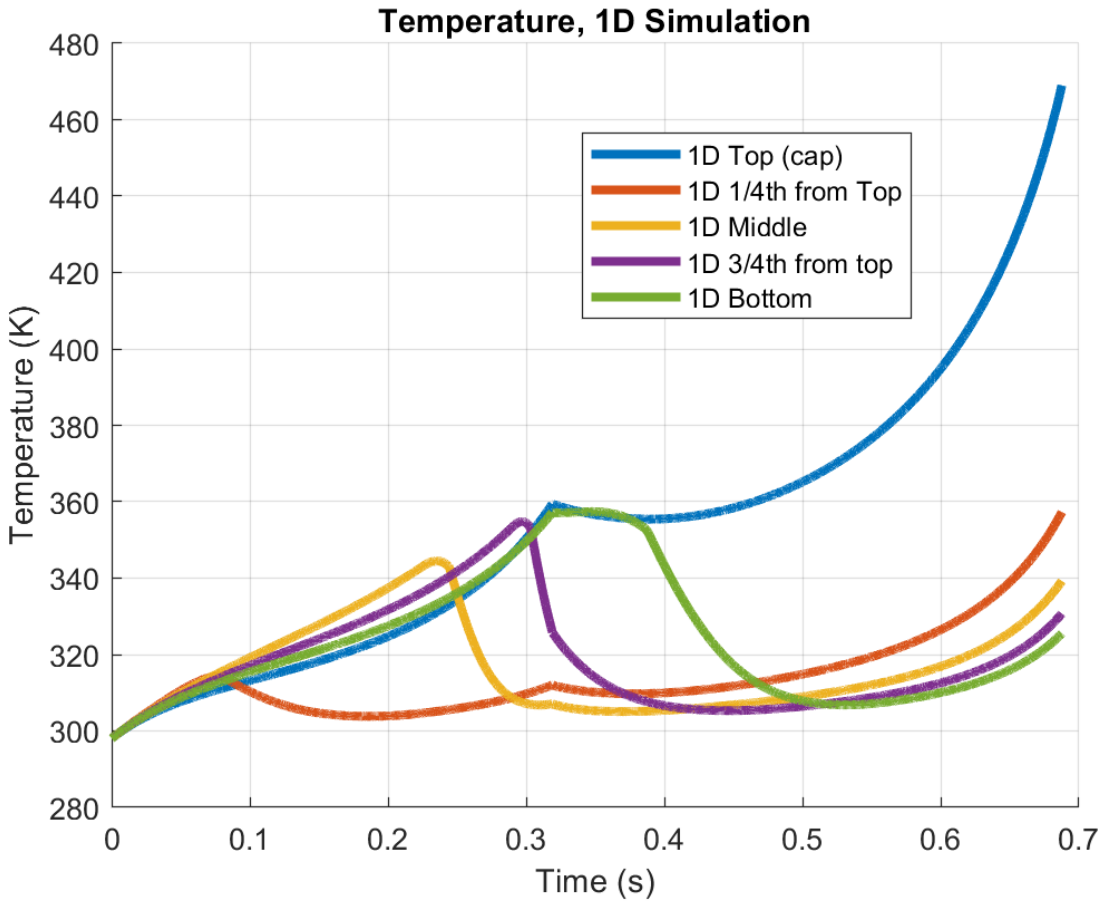

Figure 3.12: One-dimensional air simulation results for various partitions within the chamber for the cost optimal flow intensifier design.

3.7 Design Comparison of Various Optimization Techniques

In this chapter, an investigation of various design approaches of a highly efficient compressor/expander system was conducted. One design approach was to maximize the power density of the system while the other minimized system cost. Previous work has developed a power density optimal design from which a comparison of the cost optimal designs produced in this paper will be made. The cost progression of each design iteration can be viewed in Table 3.5 below:

Table 3.5: Cost progression of compressor/expander system design with performance specifications.

Opt. Method	**Eff.**	**Power Density** kW/m^3	**Compression Time** [sec]	α	$\frac{S_V}{PD} = \left[\frac{\$_{cham}}{kW}\right]$ $\frac{\alpha S_Q}{PD} = \left[\frac{\$_{pump}}{kW}\right]$	**System Cost/kW** $\left[\frac{\$_{sys}}{kW}\right]$
Power Density Dia. = Opt. h = 0.70 m	92%	1470	1.6	0.73	$\left[\frac{\$_{cham}}{kW}\right] = \frac{\$67.13}{kW}$ $\left[\frac{\$_{pump}}{kW}\right] = \frac{\$181.76}{kW}$	$248.89
Cost: Dia. = 4.3 cm h = 2.75 m	92%	559	4.21	0.25	$\left[\frac{\$_{cham}}{kW}\right] = \frac{\$20.30}{kW}$ $\left[\frac{\$_{pump}}{kW}\right] = \frac{\$163.69}{kW}$	$183.99
Cost: Flow Intensifier h = 1.2 m	92%	3446	0.68	0.51	$\left[\frac{\$_{cham}}{kW}\right] = \frac{\$8.75}{kW}$ $\left[\frac{\$_{pump}}{kW}\right] = \frac{\$54.16}{kW}$	$62.91

The results show that when considering a compressor/expander system without a flow intensifier component, a moderate decrease in cost, about 26%, can be achieved through reducing the α-value of the system. Unfortunately, this cost reduction comes with the hindrance of increasing the compression time, thus decreasing the system power density. Attempts were made to mitigate this effect by providing the system with the most efficient chamber geometry possible by relaxing the height constraint of the chamber. While the power density optimized case limited the height of the chamber to 70cm, the optimization over α allowed for a chamber height of 275cm. Increasing the

height allowed for a smaller cross sectional area for the chamber for a given chamber volume, a factor that greatly increases thermal efficiency as stated in section 3.2. Increased heat transfer properties allowed for smaller α-values to reach our specified desired efficiency. This trend continued until the α-value was small enough to where the pump would produce flow at a constant rate and yet the thermal efficiency would still meet requirements. At which point the system would benefit from both the large cost benefits of the small α-values and also the power density benefits of the narrow tall tube chamber geometry. Omitting the optimal flow trajectory from the system would allow for a fixed displacement pump to drive the liquid piston instead of a variable displacement pump, significantly reducing the cost of the pump further. Still, the cost of the pump was so large compared to the chamber cost that the cost benefits achieved from the pump size decrease outweighed the drawback of decreased power density.

The desire to now achieve a high power density while still remaining in the low α-value system regime led to the idea of somehow increasing pump flow rate output while still keeping the physical size of the pump relatively small by comparison. Thus the flow intensifier component was introduced into the design in order to augment the flow rate of the pump while still benefiting from the cost reductions of the low α-value pump sizes. The introduction of the flow intensifier allowed the compressor/expander system to benefit from both design optimization techniques by combining the benefits of each into a single design. This design recieves the flow augmentation of the flow intensifier, the heat transfer benefits of the optimal shape and heat transfer material distribution, and can remain in the low α-value regime with a much cheaper fixed displacement pump/motor. All of these benefits accumulate to an impressive cost savings of 75% and a power density *increase* of 234% when compared to the power density optimized design. These cost calculations include the additional raw material cost associated with the flow intensifier in the S_v term (described in section 3.6) with some exceptions. The additional cost in S_v is purely the raw material cost associated with the additional material needed to construct the pressure vessel and the mechanical piston geometry shown in Figure 3.9. The S_v term does not inlcude additional cost associated to manufacturing costs (i.e. new

sealing surfaces). It should be noted that in the cost optimized designs, the height contraint was relaxed which benefits both chamber cost and system thermal efficiency.

3.8 Summary

A method for predicting system cost given a set of design variables was introduced and used to systematically decrease system cost in order to find an optimal cost solution. These methods used insight gained from the previous power density optimized design and incorporated them with an iterative cost optimization to produce two new design concepts. The first design concept derived in section 3.3 found that a small pump flow rate compared to the volume of compressible gas in the compression/expansion chamber yielded the most cost effective solution. Furthermore, decreasing the cross sectional area of the chamber by increasing the chamber height provided that heat transfer neccesary to omit the optimal flow trajectory all together. This reduced system complexity and allowed for a much cheaper fixed displacement pump to drive the liquid piston. Continuing forward with this design philosophy, a flow intensifier was introduced into the system to further augment pump flow rate without increaseing pump size. Implementing the flow intensifier showed great improvements to all design performace metrics including cost, power density, and compression time as seen in Table 3.5. This design facilitated the use of design traits that showed benefits in both power density system and cost reduction of the system. Results show a cost reduction of 75% while maintaining an impressive power density increase of 234%. Some underestimation of the performance may be attributed to use of the a zero-dimensional air dynamic model. Therefore, a one-dimensional heat transfer model was developed and used to verify the efficiencies calculated in this study. Results show good agreement was achieved between the zero-dimensional and one-dimensional models. However, the flow intensifier assumes an instantaneus switching valve which will not be the case in the physical prototype implementation. Diverting flow from the initial compression stage compressor/expander to the final compression stage will take time, which in turn will increase compression time effectively decreasing power density slightly. Nevertheless,

great improvements have been made when comparing the performance metrics used by the previous power density optimization study.

4. Liquid-Air Interface Stability of the Inverted Liquid Piston Compressor

4.1 Introduction

The compression of gas often comes at the expense of a rise in temperature of the gas. Temperature increase of the gas corresponds to an increase in internal energy of the gas itself. This internal energy is often wasted when the gas is stored for later use and eventually cools to ambient temperatures. To minimize the addition of internal energy to the gas, heat must be transferred out of the system before storage. If this heat transfer can occur during the compression stroke, the rise in temperature of the gas will reduce and therefore reduce the amount of work required to compress the gas to the same pressure. Compressing gas utilizing a high heat transfer compression stroke will therefore increase the efficiency of the CAES system.

The CAES system proposed in chapter 1 requires a two-stage air compression in order to achieve a more efficient compression. Having two stages for the compression cycle allows the air to cool in between each compression. Intercooling between compression stages allows the air to reach the final pressure at a much lower temperature than would be possible if the air was compressed in a single process. The 1st stage compression will take air at atmospheric pressure (~1 bar), compress it to about seven times atmospheric pressure (~7 bar), and store the pressurized air in a storage vessel. This pre-compressed air is supplied to the 2nd stage compressor described in chapter 3 to reach the final storage pressure. The liquid piston compressor approach can also be used for the 1st stage compressor which provides many benefits over traditional air compressors.

A benefit of using liquid as the compression surface is a liquid's ability to deform around objects during a compression stroke. To increase heat transfer, a porous media may be inserted into the compression chamber. The porous media would contain a large surface area to volume ratio, providing many surfaces for heat created by gas compression to transfer into the material. The heat then transfers to the liquid as the

porous media is submerged during the compression cycle. The gas can then be stored while maintaining its energy density and the heat recirculated out of the liquid in preparation for the next compression cycle. A previous study aimed to determine what type of geometry would yield the highest heat transfer capabilities [31]. Through CFD simulations, an interrupted cross plate design was found to be the most promising geometry. The study showed that the interrupted cross plate geometry of the heat exchanger forced new boundary layers necessary for heat exchange to be created as liquid passed over the plates. Interrupted cross plate designs can be reduced to a smaller representative elemental volume (REV) to reduce the computation time of evaluating heat transfer capabilities. Further study was conducted to test different geometry parameters shown Figure 4.1 (left) of the interrupted cross plate design shown in Figure 4.1 (right).

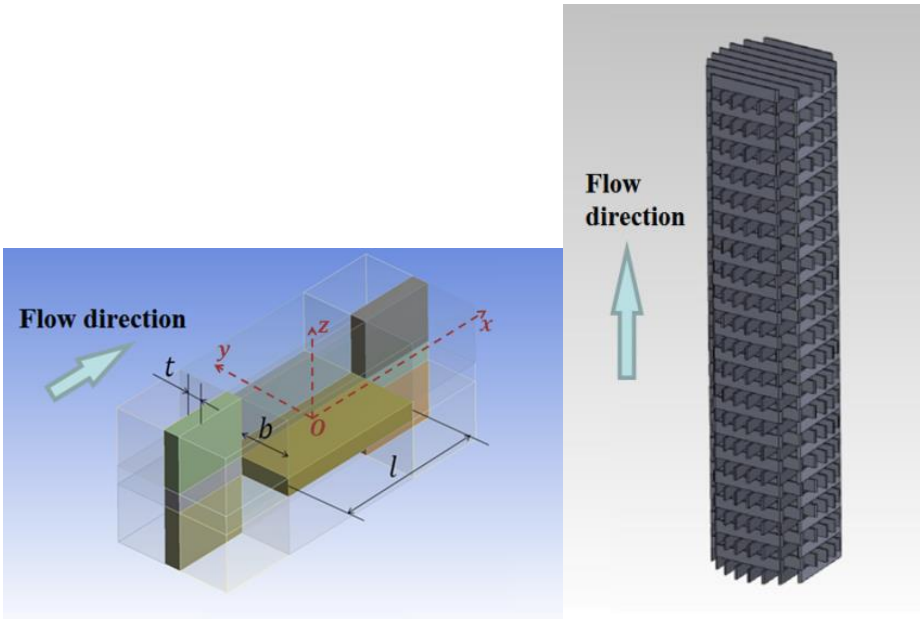

Figure 4.1: Representative elemental volume of porous media (left) and full cross-plate heat exchanger porous media insert (right) [31].

Traditional liquid piston compressors must pump the liquid into the compression chamber, causing the liquid surface to rise and compress the gas above. The compression

cycle has a frequency limitation created by liquid separation when rapidly cycling the liquid in and out of the compression chamber. Disruption of the liquid-air interface is undesirable as air becomes entrained in the liquid reducing compression capability. Liquid droplets can also become ejected into the outflow of pressurized gas. It was shown in [45] that the undesirable mixing was primarily caused by the acceleration of the liquid-air interface. The acceleration of the interface is a function of the operation frequency of the compression cycle. To increase the frequency of compression cycles, the traditional liquid piston was inverted. The Inverted Liquid Piston Compressor (ILPC) allows the liquid piston to remain stationary while reciprocating the compression chamber itself. Reciprocation of the compression chamber subjects the liquid-air interface to rapid perturbation by the porous media insert creating undesirable instabilities. A previous study detailed the general trend of liquid interface stability degradation as the Reynold's number increased [46]. The study utilized high speed footage of the ILPC during operation and qualitatively determined the liquid interface stability of various porous media inserts for a range of Reynold's numbers. Different Reynold's numbers were achieved by increasing the operation frequency of the ILPC. Recall the conceptual model of the inverted liquid piston introduced in chapter 1 shown in Figure 1.6.

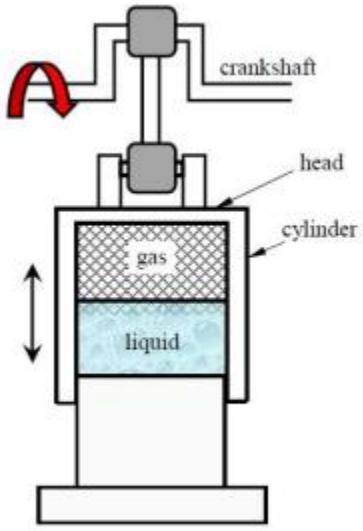

Figure 1.6: Inverted liquid piston compressor conceptual diagram.

This chapter aims to quantify the interfacial stability effects the interrupted cross plate heat exchanger design creates during operational cycling frequencies. A 2-D infinite depth liquid-gas interface model was developed using Marker and Cell (MAC) CFD code. The model used a subset of geometry parameters of the heat exchanger REVs to model how the liquid moves during operation. The primary metric for the quantification of interfacial stability is the resultant liquid wave amplitude for a given operational frequency and heat exchanger geometry parameters. The interrupted cross plate design was simplified to non-interrupted parallel plates in order to reside within the limitations of the 2-D model. Rapid prototyping of different plate separation, an important design variable in the REV heat exchanger study, were created for experimental validation of the CFD model. Experiments were conducted that collected high-speed footage of the parallel plates oscillating up and down within the liquid domain. Edge detection software was developed to systematically collect wave amplitude data from the data videos in order to determine how operational frequency and plate separation affects the surface stability. CFD models were run under the same parameters and the results were compared with the experimental data.

4.2 ILPC Model Description

The ILPC consists of a stationary liquid column over which a chamber can move up and down in order to compress the air. During operation, the chamber's oscillating motion is driven by a crankshaft rotating at a set frequency. As the crankshaft rotates, the oscillating chamber compresses the air as it moves downward over the liquid piston, and intakes atmospheric air as the chamber moves up away from the liquid piston. Fixed to the top end cap of the chamber is the porous material. During each compression stroke the porous material is in contact with the air, but dips into the liquid piston as the volume of air decreases. It is this reciprocating motion of the heat transfer material dipping in and out of the liquid piston that is being modeled in this chapter.

Computational Fluid dynamics (CFD) simulations were used to model the behavior of the liquid-gas interface during ILPC operation. The primary goal of the model was to develop a predictive tool to calculate liquid wave amplitude based on the porous media insert geometry parameters. The geometry parameter of greatest interest is the separation distance of the porous media plates. In order to model the effects of plate separation distance on the liquid-air interface, the simplification of using long parallel plates that are uninterrupted was made. This simplification to the geometry was made so that the system could be modeled in two dimensions yet still reveal valuable information about interface motion due to the plate separation distance. The 2-D computational domain of the interface and parallel plates can be seen in Figure 4.2 (left).

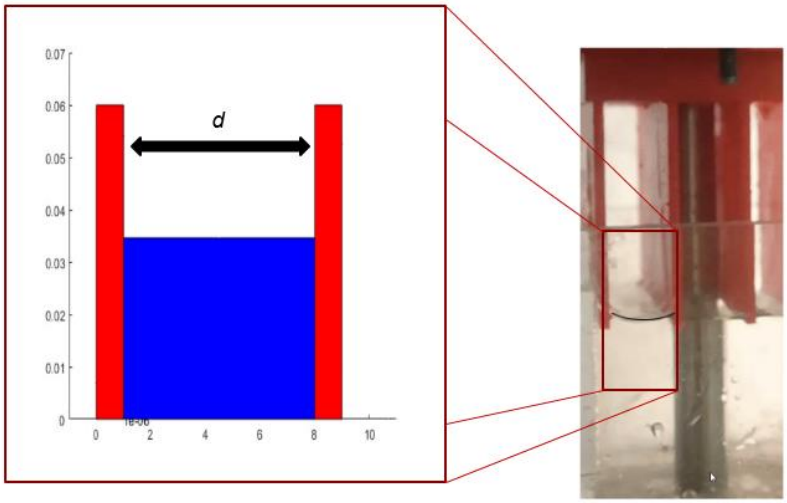

Figure 4.2: Model fluid domain (left) and experimental system fluid domain (right)

The 2-D computational domain is defined in the Cartesian plane with the fluid surface at the position y = 0 and is shown in blue. The red rectangles on either side of the fluid symbolizes the porous media insert plates and are separated by a separation distance *d*. Figure 4.2 (right) shows the experimental fluid domain the model is approximating. The CFD code implemented solved the Navier-Stokes equations in velocity/pressure form by using a control volume approach. Marker and Cell (MAC) method was used to discretize the domain into separate control volume cells. The MAC method was used

since this method has long been used for modeling surface interface problems [47]. This method uses a control volume approach to track the momentum and mass of the fluid. The fluid motion is governed by the well known Navier-Stokes equation which in the integral form for 2-D cartesian plane consists of the following:

$$\frac{\partial}{\partial t}\int_V udV = -\oint_S u\boldsymbol{u}\cdot\boldsymbol{n}dS - \frac{1}{\rho}\oint_S pn_x + \nu\oint_S \nabla u\cdot\boldsymbol{n}dS \tag{4.1}$$

$$\frac{\partial}{\partial t}\int_V vdV = -\oint_S v\boldsymbol{u}\cdot\boldsymbol{n}dS - \frac{1}{\rho}\oint_S pn_y + \nu\oint_S \nabla v\cdot\boldsymbol{n}dS \tag{4.2}$$

here u is the fluid velocity in the x direction, v is the fluid velocity in the y direction, $\boldsymbol{u} = (u, v)$ represents the velocity vector comprised of these components,ρ is the density of the fluid, and ν is the kinematic viscosity. Each control volume has a surface normal vector $\boldsymbol{n}$ that consists of a $\hat{x}$ component n_x and a $\hat{y}$ component n_y. The Navier-Stokes equations are subject to the conservation of mass equation:

$$\oint_S \boldsymbol{u}\cdot\boldsymbol{n}dS = 0 \tag{4.3}$$

This condition implies that the amount of mass entering a control volume must equal the amount of mass leaving. This general form of the equations of motion for the fluid being modeled can be simplified through imposing boundary conditions.

4.3 Boundary Conditions

Boundary conditions for the fluid interface model included a no-slip velocity condition on fluid-plate interfaces. The velocity boundary condition for the plate was calculated via the well know equation for the piston velocity of a crank slider mechanism [48]:

$$v = -r_{cr}\omega\left[sin(\omega t) + \frac{r_{cr}}{2l_{cr}}\frac{sin(2\omega t)}{\sqrt{1-(r_{cr}sin(\omega t))^2}}\right] \tag{4.4}$$

here r_{cr} is the crank radius, ω is the angular velocity of the crank, l_{cr} is the length of the connecting rod, and t is time. This condition was imposed at each vertical plate contact with the fluid. The model assumes that there is no horizontal plate motion and therefore the horizontal velocity on the fluid-plate contact is set to zero.

Another boundary condition imposed on the model was the jump condition of stress on the fluid-gas interface. The boundary condition is derived from the principle that the forces on an element of interfacial area must be in equilibrium since the interface is assumed to have zero thickness and therefore zero mass [49]. This can be described by:

$$n \cdot \overline{\overline{T_{air}}} \cdot n - n \cdot \overline{\overline{T_{liquid}}} \cdot n = \sigma_w(\nabla \cdot n) \tag{4.5}$$

where $\overline{\overline{T_{air}}}$ represents the stress tensor of the air, T_{liquid} represents the stress tensor in the liquid, n is the normal vector of the surface, and σ_w is the surface tension property of the fluid. Assuming that air has negligible effects on the interface compared to the much heavier liquid, the condition can be written as:

$$n \cdot \overline{\overline{T_{liquid}}} \cdot n = \sigma_w(-\nabla \cdot n) \tag{4.6}$$

notice here that -$\nabla \cdot n$ is the curvature of the surface, and therefore multiplying the surface curvature by the surface tension constant yields the surface tension force. (4.6) represents the normal stress balance at the interface. The jump in normal stress across the interface must balance the surface curvature force per unit area. With these boundary conditions in place, the governing equations can now be discretized for computation.

4.4 Discretization of Governing Equations

The CFD method used consisted of the Marker and Cell approach to discretize and solve the Navier-Stokes equations [50]. A staggered MAC grid was used with each cell containing a pressure p, defined at its center. The velocity of the cell $\boldsymbol{u} = (u, v)$ must satisfy the continuity equation (4.3) at the end of each time step. The cell shown in Figure 4.3 depicts the control volume necessary to apply the conservation of mass condition. This is a square cell with a side length h and pressure node $P_{i,j}$ at its center.

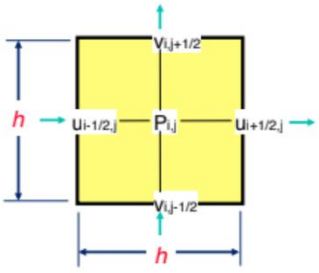

Figure 4.3: MAC cell control volume architecture [50].

To conserve momentum, two other cells must be defined which are depicted in Figure 4.4. These cells select a control volume centered around each velocity component.

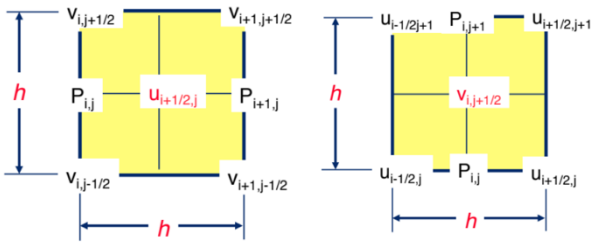

Figure 4.4: MAC cell control volume centered around $u_{i+1/2,j}$ (left) and $v_{i,j+1/2}$ (right) [50].

Velocities at the edges can be found directly by utilizing these two extra cell architectures centered around each velocity component, whereas only utilizing the cell shown in Figure 4.3 would limit the solving of the edge velocities by interpolation only.

By overlaying all three cell types, a staggered grid of control volumes is constructed. The staggered MAC grid can be seen in Figure 4.5.

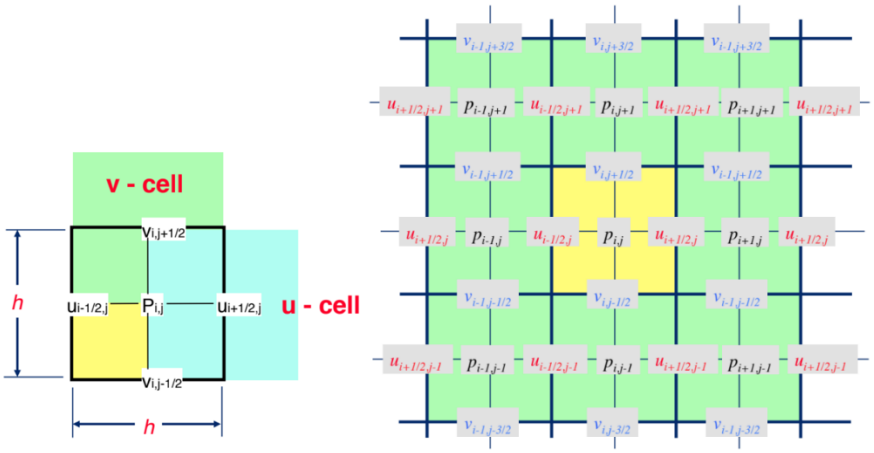

Figure 4.5: Overlain control volume cells (left) and staggered MAC grid (right) [50].

With the staggered MAC grid in place, discretization of the control volumes can be derived. This is accomplished by breaking down the conservation of momentum equations (4.1) and (4.2) into the unsteady, advective, pressure, and viscous terms. The rate of change of x and y-momentum can be described by equations (4.7) and (4.8) below:

$$\frac{\partial}{\partial t}\int_V udV \approx \frac{u_{i+1/2,j}^{n+1} - u_{i+1/2,j}^{n}}{\Delta t} h^2 \tag{4.7}$$

$$\frac{\partial}{\partial t}\int_V vdV \approx \frac{v_{i,j+1/2}^{n+1} - v_{i,j+1/2}^{n}}{\Delta t} h^2 \tag{4.8}$$

the notation $u_{i+1/2,j}^{n}$ refers to the nth x-component velocity in cell i,j (and $u_{i-1/2,j}^{n}$ refers to cell $i-1,j$) since fractional indexing numbers are not allowed in a computer program. This notation is used to explain the staggered MAC grid but is slightly modified to use integers in the actual code. As momentum travels between cells, the flux in and out of the

cells needs to be accounted for. To find the fluxes across the boundary, the advective term can be integrated over the boundary:

$$\oint_S u\boldsymbol{u}\cdot\boldsymbol{n}dS \approx \left((u^2)^n_{i+1,j} - (u^2)^n_{i,j} + (uv)^n_{i+1/2,j+1/2} - (uv)^n_{i+1/2,j-1/2}\right)h \tag{4.9}$$

$$\oint_S v\boldsymbol{u}\cdot\boldsymbol{n}dS \approx \left((uv)^n_{i+1/2,j+1/2} - (uv)^n_{i-1/2,j+1/2} + (v^2)^n_{i,j+1} - (v^2)^n_{i,j}\right)h \tag{4.10}$$

the pressure term in the x and y-momentum equations can be written as:

$$\frac{1}{\rho}\oint_S pn_x dS \approx \frac{1}{\rho}\left(p_{i+1,j} - p_{i,j}\right)h \tag{4.11}$$

$$\frac{1}{\rho}\oint_S pn_y dS \approx \frac{1}{\rho}\left(p_{i,j+1} - p_{i,j}\right)h \tag{4.12}$$

lastly, expanding the viscous diffusion term in the momentum balance equations (4.1) and (4.2) shows the dot product of the surface normal vector and the partial derivatives of the velocity components:

$$v\oint_S \nabla u\cdot\boldsymbol{n}dS = v\oint_S \left(\frac{\partial u}{\partial x}n_x + \frac{\partial u}{\partial y}n_y\right)dS \tag{4.13}$$

$$v\oint_S \nabla v\cdot\boldsymbol{n}dS = v\oint_S \left(\frac{\partial v}{\partial x}n_x + \frac{\partial v}{\partial y}n_y\right)dS \tag{4.14}$$

computing the derivatives at the boundary and integrating over the surfaces yields the final viscous diffusion terms for the x-momentum (4.15) and the y-momentum (4.16).

$$v\left(u^n_{i+3/2,j} + u^n_{i-1/2,j} + u^n_{i+1/2,j+1} + u^n_{i+1/2,j-1} - 4u^n_{i+1/2,j}\right) \tag{4.15}$$

$$v\left(v^n_{i+3/2,j} + u^n_{i-1/2,j} + u^n_{i+1/2,j+1} + u^n_{i+1/2,j-1} - 4u^n_{i+1/2,j}\right) \tag{4.16}$$

Combining all these terms together provides the complete solution strategy. The discretized equation of the conservation of moment equations (4.1) and (4.2) can be written as (4.17) and (4.18) respectively:

$$\begin{aligned} \frac{u^{n+1}_{i+\frac{1}{2},j} - u^n_{i+\frac{1}{2},j}}{\Delta t} = \\ -\frac{1}{h}\left((u^2)^n_{i+1,j} - (u^2)^n_{i,j} + (uv)^n_{i+\frac{1}{2},j+\frac{1}{2}} - (uv)^n_{i+\frac{1}{2},j-\frac{1}{2}}\right) \\ + \frac{v}{h^2}\left(u^n_{i+\frac{3}{2},j} + u^n_{i-\frac{1}{2},j} + u^n_{i+\frac{1}{2},j+1} + u^n_{i+\frac{1}{2},j-1} - 4u^n_{i+\frac{1}{2},j}\right) \\ -\frac{1}{h}\left(P_{i+1,j} - P_{i,j}\right) \end{aligned} \tag{4.17}$$

$$\frac{v_{i,j+\frac{1}{2}}^{n+1} - v_{i,j+\frac{1}{2}}^{n}}{\Delta t} =$$
$$-\frac{1}{h}\left((uv)_{i+\frac{1}{2},j+\frac{1}{2}}^{n} - (uv)_{i-\frac{1}{2},j+\frac{1}{2}}^{n} + (v^2)_{i,j+1}^{n} - (v^2)_{i,j}^{n}\right)$$
$$+\frac{\upsilon}{h^2}\left(v_{i+\frac{3}{2},j}^{n} + u_{i-\frac{1}{2},j}^{n} + u_{i+\frac{1}{2},j+1}^{n} + u_{i+\frac{1}{2},j-1}^{n} - 4u_{i+\frac{1}{2},j}^{n}\right) \quad (4.18)$$
$$-\frac{1}{h}\left(P_{i,j+1} - P_{i,j}\right)$$

where $P = \frac{p}{\rho}$. Furthermore, we can write the conservation of momentum and mass equations (4.17) and (4.18) in a compact vector equation:

$$\frac{\boldsymbol{u}_{i,j}^{n+1} - \boldsymbol{u}_{i,j}^{n}}{\Delta t} = -\boldsymbol{A}_{i,j}^{n} - \nabla_h P_{i,j} + \boldsymbol{D}_{i,j}^{n} \quad (4.19)$$

$$\nabla_h \cdot u_{i,j}^{n+1} = 0 \quad (4.20)$$

here $\boldsymbol{A}_{i,j}^{n}$ are the advective terms from (4.9) and (4.10), $\nabla_h P_{i,j}$ are the pressure terms (4.11) and (4.12), and $\boldsymbol{D}_{i,j}^{n}$ are the diffusive terms (4.15) and (4.16). Equation (4.19) represents the evolution of velocity while equation (4.20) represents the constraint on the velocity (conservation of mass). By using the projection method, we introduce a temporary velocity which is calculated using only the advection and diffusive terms. This allows us to split $\boldsymbol{u}_{i,j}^{n+1}$ into a pressure term and a temporary velocity term.

$$\boldsymbol{u}_{i,j}^{n+1} = \boldsymbol{u}_{i,j}^{t} - \Delta t \nabla_h P_{i,j} \quad (4.21)$$

$$\boldsymbol{u}_{i,j}^{t} = \boldsymbol{u}_{i,j}^{n} + \Delta t\left(-\boldsymbol{A}_{i,j}^{n} + \boldsymbol{D}_{i,j}^{n}\right) \tag{4.22}$$

With $\boldsymbol{u}_{i,j}^{t}$ being the temporary velocity which can also be referred to as a predicted velocity. Now the velocity constraint equation (4.20) is used to derive an equation for pressure by calculating the divergence of equation (4.21).

$$\nabla_h^2 P_{i,j} = \frac{1}{\Delta t}\nabla_h \cdot \boldsymbol{u}_{i,j}^{t} \tag{4.23}$$

Now with all the governing equations discretized, the stage is set to acquire a solution. Using the no-slip velocity boundary condition (4.4), we can calculate the temporary velocity (4.22). Then the pressure field needed to make the velocity field incompressible is calculated such that it also satisfies the fluid-gas interface boundary condition (4.6). Adding this pressure field to the temporary velocity will result in the true fluid velocity field for that time step as seen in equation (4.21). Figure 4.6 shows a flowchart of the computational method described.

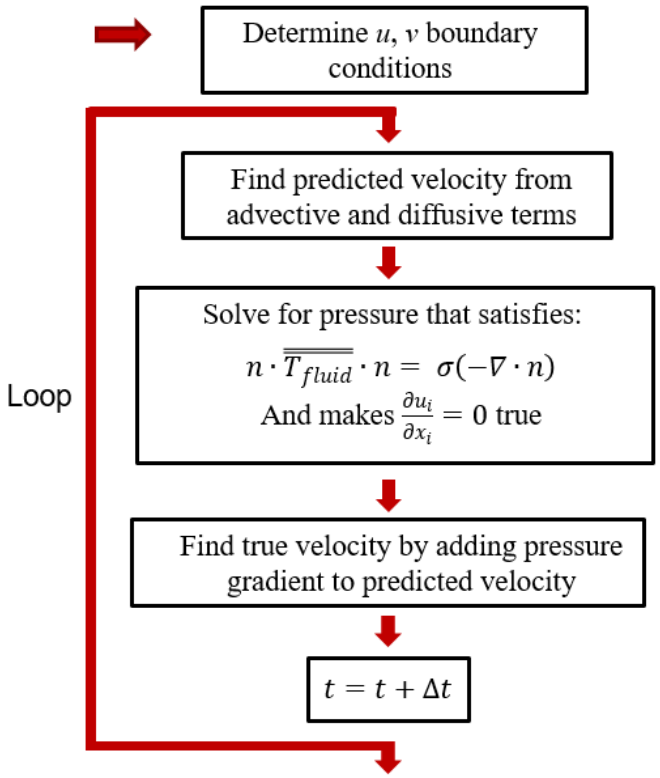

Figure 4.6: Computational flow chart.

For each simulation, the plate separation distance d was defined along with the frequency of operation f (rotational frequency $\omega = 2\pi f$). The side length of each square MAC cell, h, was determined by the plate separation distance divided by the number of nodes, n, in the simulation:

$$h = \frac{d}{n} \tag{4.24}$$

Since the simulation is in two dimensions, the number of nodes n creates a MAC grid that is $[n + 2 \times n + 2]$. The two extra nodes for each axis are a result of the staggered MAC grid architecture. The computational domain must reside in cells that contain the pressure marker $P_{i,j}$ however there are boundary cells around the computational domain that are necessary to impose boundary conditions and allow calculation of the momentum equations. Depending on how small the time step is for each calculation, the simulation

can get very computational expensive and also increasing exponentially as the number of nodes increases. For this reason, a computational domain of $n = 20$ nodes is chosen due to the time step required for the simulation to remain stable at higher operating frequencies. While this domain reduced resolution of the interface the overall interface amplitudes were consistent for higher numbers of nodes.

Table 4.1: Simulation Physical Properties

Property Description	**Value**	**Unit**
Density (Water)	$\rho = 1000$	$\frac{kg}{m^3}$
Dynamic Viscosity (Water)	$\upsilon = 8.9 \times 10^{-4}$	$\frac{kg}{m \cdot s}$
Surface Tension (Water)	$\sigma_w = 0.072$	$\frac{N}{m}$
Acceleration of Gravity	$g = 9.8315$	$\frac{m}{s^2}$
Simulation Time Step	$\Delta t = 1 \times 10^{-5}$	s

4.5 Experimental Approach

The experimental setup used was a modified version of the prototype ILPC (see Figure 4.7) originally built by Steven Thomalla, a PhD candidate in the Mechanical Engineering Department at the University of Minnesota. Modifications to the ILPC were necessary to gather fluid interface data in an environment that matches the CFD model conditions as close as possible. These modifications, as seen if Figure 4.8, include a clear fluid box, a Nikon J1 camera mount, and a parallel plate manifold with multiple rapid prototype parallel plate separation inserts.

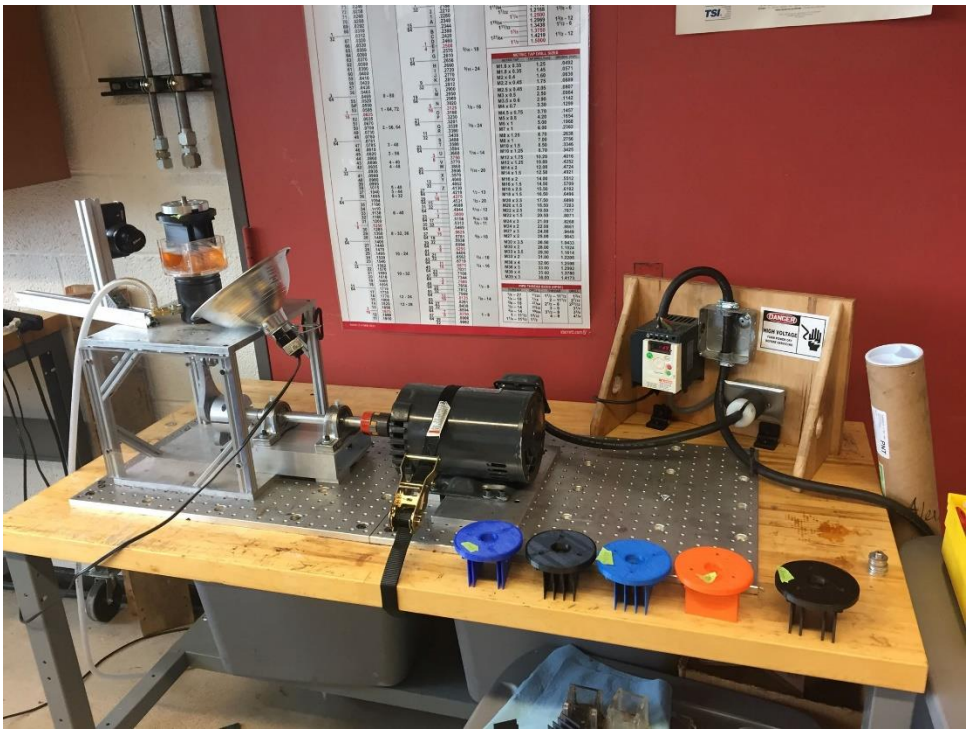

Figure 4.7: Experimental setup of ILPC

Figure 4.8: Modified ILPC used for porous media experiments

The Dayton Model 4THV8 motor drives the crankshaft, which then drives a crank slider mechanism transferring the rotation of the crankshaft into oscillatory linear travel of the center rod. Attached to the center rod is the parallel plate manifold from which different parallel plate inserts can be attached. As the center rod oscillates up and down, the parallel plates dip up and down in the fluid box. The fluid box is made of clear acrylic so easy capturing of high speed data videos can be obtained via the Nikon J1 camera. Orange coloring was added to the experimental fluid, which was room temperature water for this experiment. Backlights were used to increase the contrast between the orange fluid and the air, allowing for more accurate edge tracking during data video processing. In order to test different operating frequencies, the Dayton motor was controlled by a Schneider Electric ATV12 2HP 3 phase variable frequency drive (VFD).

The data collection process of this experiment consisted of capturing high speed video footage of the parallel plates perturbing the liquid-gas interface. Parallel plates of separation distances 5 mm, 7.5 mm, and 10 mm were recorded at frequencies 1-8 Hz in one Hz intervals. The VFD was configured to run at a specified operating frequency and data videos were captured once steady state was achieved. This totaled 24 data videos captured at 400 fps for a duration of five seconds each. The height of the fluid interface within the box was also recorded with the plates fully submerged at bottom dead center as well as nearly unsubmerged at top dead center. Since the experimental fluid domain was finite, the plates displaced fluid as they submerged. Fluid interface elevation levels caused by this displacement were taken into account when determining fluid wave amplitude during video processing. The Nikon J1 camera was positioned to view down the length of the plates and be able to capture the entire stroke.

Footage was processed using developed edge detection code which tracked the wave amplitudes created by the oscillating plates. This code tracked the edge of the fluid by utilizing a color gradient created by the contrast between the RGB values of the fluid and the air. Orange food coloring was added to increase the contrast and therefore increase the accuracy and robustness of the edge tracking. By using a known distance reference within the footage, a conversion between number of pixels and distance in millimeters was achieved. Fluid wave amplitude was tracked and the maximum value was recorded for four consecutive cycles of the oscillating parallel plates. Removing the fluid interface height change contributed to the submersion of the plates resulted in the final values of wave amplitudes for each data video. A sample of the edge tracking code can be seen in Figure 4.9.

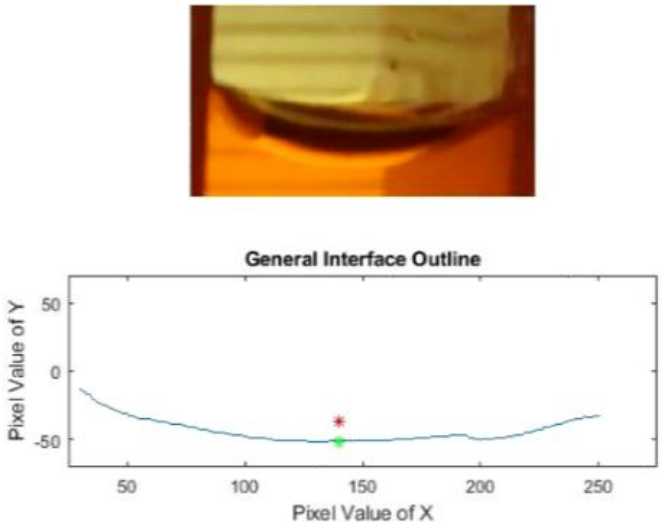

Figure 4.9: Edge tracking of liquid interface

4.6 Results

CFD models were run for each plate separation tested for the frequencies of 1-8 Hz for a total of 24 runs. Each model ran for five seconds, except for the 1 Hz frequency runs, which ran for eight seconds to ensure steady state was achieved before wave amplitudes where collected. An example output of the model has been overlaid upon an experimentally obtained video of the plates in motion when under the same operating conditions as the model. Figure 4.10 shows the example model results at different key times during the operation cycle. These times occur when the interface reaches an inflection point (Figure 4.10 left), when the plates are falling (Figure 4.10 middle), and when the plates are rising (Figure 4.10 right). The model results show a similar wave form to what was captured experimentally.

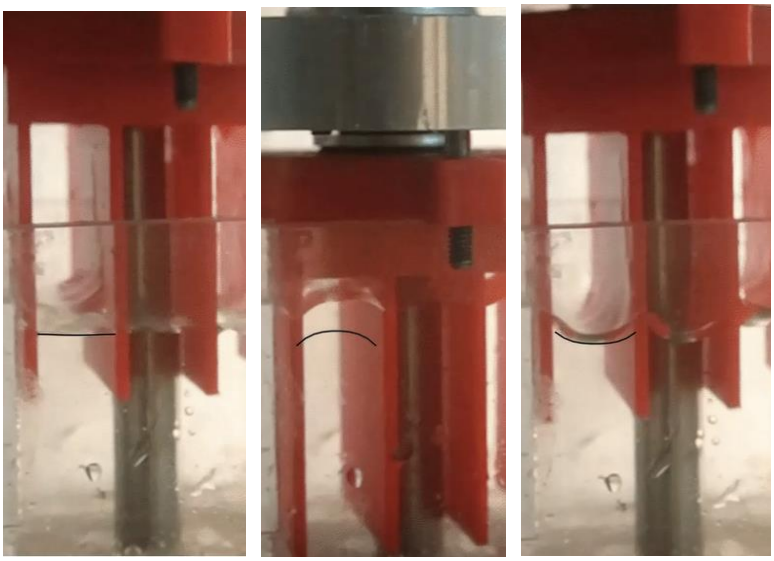

Figure 4.10: Experimental video overlain with model results at different times.

Results of the experimental testing where gathered and plotted along side the simulated results. The primary metric of interest was the maximum amplitude of the wave formed on the liquid-air interface. Wave amplitude was defined as the maximum height of the wave with respect to the height of the interface at rest. This calculation took into account the volume of liquid that was displaced by the parallel plates dipping into the liquid which caused the baseline interface level to rise. Wave amplitudes were gathered via the edge tracking software and recorded for four consecutive cycles. The standard deviation of the data set for each operating frequency was then calculated and this spread in the data is represented by the error bars on the plots. The figures show that the wave amplitude is largely influenced by the operating frequency. As the system reached higher operating frequencies, the camera began shaking, which created higher uncertainties in the wave amplitudes. The uncertainties in experimental wave amplitudes are depicted by the gradually increasing error bar magnitudes as the frequency increases.

Looking at the how the plate separation distance affected the wave amplitudes is less distinguishable than the operating frequency, but still recognizable in the data. Larger plate separation correlated to smaller overall wave amplitudes for the tested frequencies.

Figure 4.11 and Figure 4.12 show all the plate separations model data and experimental data respectively.

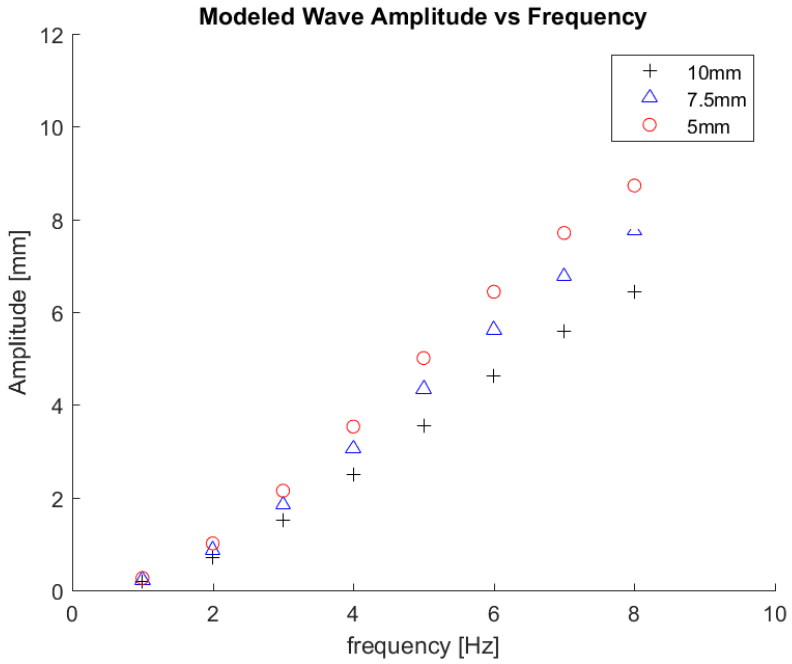

Figure 4.11. Model wave amplitudes for different plate separations.

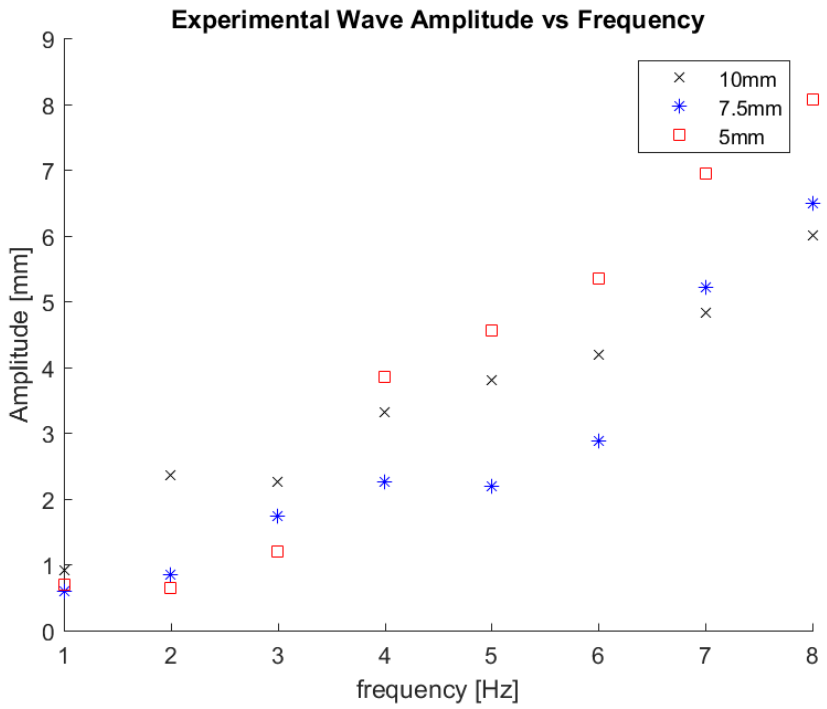

Figure 4.12: Experimental wave amplitudes for different plate separations

The model shows a clear trend of increased wave amplitude for smaller separation distances; however, the experimental results show this only for higher frequencies (7-8 Hz). The lower operating frequencies (1-3 Hz) appear to show a larger wave amplitude for the larger plate separations while the middle frequencies (4-6 Hz) seem to be in a state of transition bridging the gap between the lower and higher operating frequencies. Experimental and model data for plate separation distances of 10mm, 7.5mm, and 5mm are shown in Figure 4.13, Figure 4.14 and Figure 4.15 respectively.

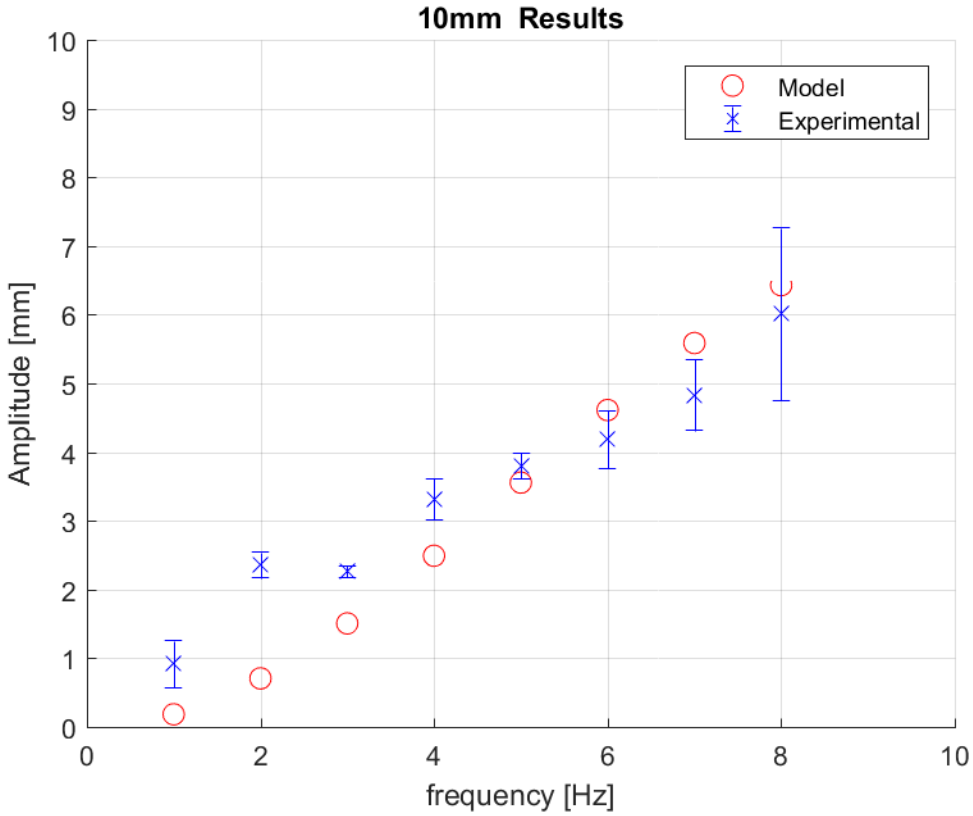

Figure 4.13: 10mm plate separation model and experimental results comparison.

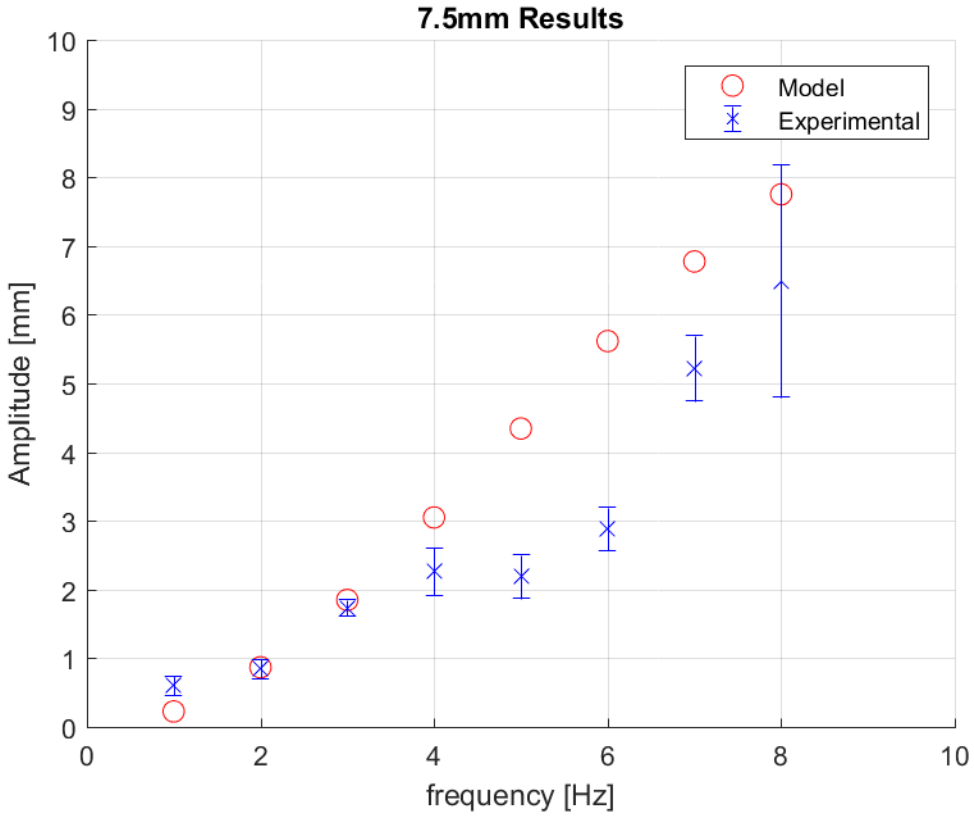

Figure 4.14: 7.5mm plate separation model and experimental results comparison.

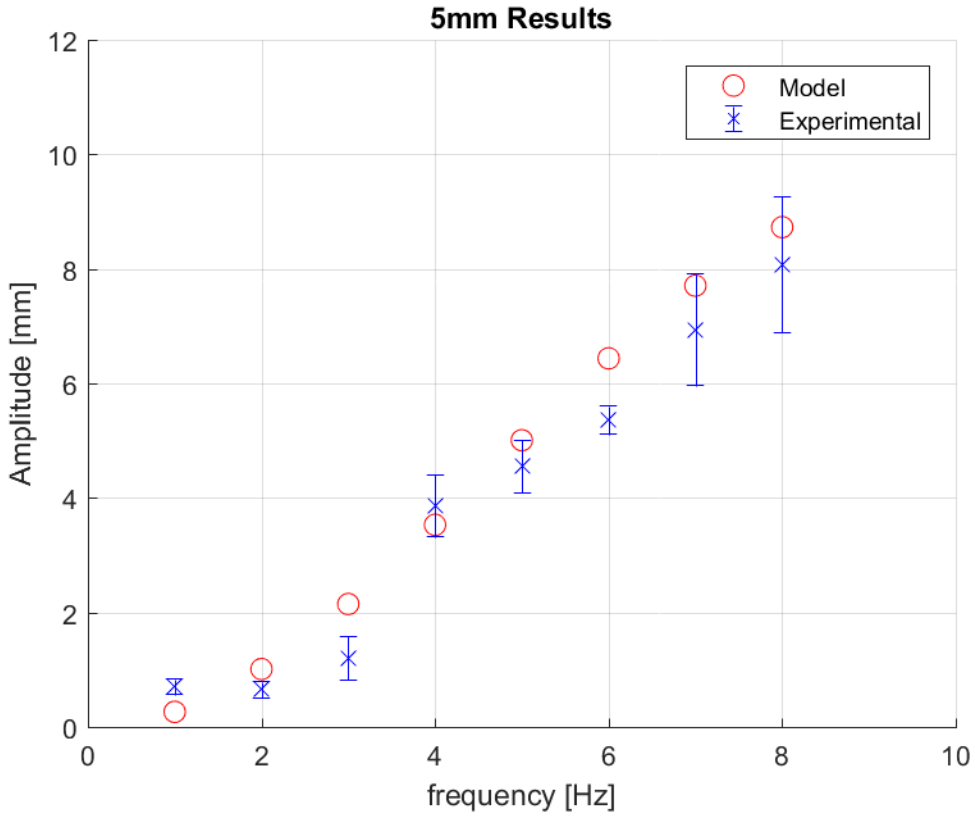

Figure 4.15: 5mm plate separation model and experimental results comparison.

4.7 Discussion

The CFD results show a consistent data formulation of wave amplitude that is dependent on both operational frequency and plate separation distance. Greater plate separation correlates to a smaller wave amplitude, which was expected. Theory suggests that increasing the frequency of oscillation of the plates would decrease the penetration depth of the waves created [49]. However, when dealing with small separation distances, the viscosity of the fluid allows for the momentum to be transferred from the boundary towards the center of the fluid domain. There is noticeable variation in data gathered experimentally. This is due to a few contributing factors including excessive shaking due to the physical limitation of the prototype, the fluid being a finite volume, and cylindrical secondary waves to form due to the oscillating center rod.

Shaking was evident during the data recording process and contributed to varying conditions when compared to the CFD model. A shaking force caused by the unbalanced reciprocating mass led to shaking of the fluid in the horizontal domain. This caused "sloshing" waves to form which made the wave amplitudes hard to distinguish. A counterbalance was fabricated to balance the reciprocating mass and this helped reduce the shaking immensely. However, some shaking still remained and became more evident at higher operational frequencies. Experimental data reflects this uncertainty as can be seen by the increasing error bars in proportion with the increase in operational frequency.

The experimental fluid domain was a 3-D finite volume and therefore showed discrepancies when compared with the 2-D infinite depth model. Most notably, the finite volume could be displaced. The plates would raise and lower the original fluid interface height as the plates dipped down into the fluid. Because the volume attributed to the plates displaced the fluid, it became difficult to determine where to mark the fluid interface position in order to measure wave amplitude. While this variation was accounted for, it still remains a significant source of error when attempting to extract data from the high-speed footage. Lastly, the 3-D fluid domain introduces some variation in boundary conditions. The front and back sides of the fluid box still adhered to the no-slip boundary condition and remained stationary during testing. Since the plates were also of finite length in the z-direction, the wave amplitude varied across the length of the box. Wave amplitudes were smallest at the fluid box walls and greatest about midway down the length of the plates. Modeling assumptions suggest that using the maximum wave amplitude would be nearest to the model prediction.

The center rod used to dip the plate inserts up and down in the fluid also provided another source of fluid momentum. Secondary waves began to form due to the cylindrical rod oscillating within the fluid. These waves appeared axisymmetric and traveled radially outwards from the no slip boundary on the center rod. Both the primary waves caused by the plates and the secondary waves were superimposed creating chaotic effects not captured in the model. A stationary sheath was put in place around the oscillating center rod to remove this moving boundary from the fluid domain. This method removed the

secondary waves leaving only a much smaller subset of waves caused by moving fluid interacting with the cylindrical sheath.

4.8 Conclusion

The present study has investigated the effects of three different parallel plate heat exchangers on a liquid-gas interface during normal ILPC operating conditions through CFD. Wave amplitude results obtained through CFD were compared to experimental data gathered via high speed video recordings. Edge tracking software was utilized to record consecutive experimental wave amplitude data and then compared with CFD results.

Parallel plate heat exchanger performance in regards to surface stability was based on surface wave amplitudes created during operation. The study shows that increasing plate separation decreases surface wave amplitudes while increasing operating frequency increases wave amplitudes. Plots of wave amplitude vs. operating frequency have been obtained.

Further study is needed to determine how the interrupted cross plate effects the fluid surface. Future work for this project could include a 3-D CFD model to study the effects of the interrupted cross plate heat exchanger design. Further optimization of the heat exchanger inserts could be achieved by providing the surface stability effects for the given geometry parameters of the heat exchanger.

5. Conclusion

5.1 Summary

As power consumption in the modern era continues to rise, utilizing clean energy sources has become paramount to the planet's future. Renewable energy sources are readily available, however not so easily integrated into the current United States power grid infrastructure. This is due to the unpredictability and intermittency of such renewable energy sources availability often not corresponding to power demand. Because of this disadvantage, much of the available renewable energy is lost when such a mismatch between power demand and power availability occurs. The development of a renewable energy storage system is therefore necessary to effectively integrate renewable energy sources onto the electrical grid. The energy storage system studied in this thesis takes advantage of both the high energy density of compressed air as well as the high power density of hydraulic power transmission. Integrating the open accumulator concept as the energy storage vessel further increased the energy density of this energy storage system. As with most compressed air systems, the air compressor is of vital importance to the overall efficiency and effectiveness of the system. Previous work has discovered the optimal compressor/expander design for maximum power density. The work conducted under this thesis focuses on two aspects of system design: the cost optimal design of the second stage compressor/expander for the future commercialization of the system; and liquid-air interface stability of the liquid piston in the first stage compressor.

The primary component of the proposed energy storage system is the second stage compressor/expander. Since the system depends on this unit to store and retrieve energy, the compression/expansion efficiency is very important. Compressing/expanding a gas to 200 times atmospheric pressure will greatly heat/cool the air, resulting in poor efficiency, unless the cycle takes a long time which in turn reduces power. Increasing the heat transfer capability of the system will greatly improve the cycle efficiency. The main benefit of a liquid piston compressor is the ability to augment heat transfer a number of ways including: Introducing heat transfer media inside of the chamber, changing the

shape of the compressor chamber, and varying the compression/expansion trajectory. Proper implementation of these advantages can greatly improve heat transfer and thus cost per power of the system. Various techniques were used to find the proper design parameters that would achieve a cost optimal design. The main contributions in this area achieved in this thesis are summarized below:

1. A method for optimizing key design parameters of a liquid piston compressor/expander was developed that minimized system cost while maintaining performance. The results of this study provided insight into the optimal flow rate calculations for compression/expansion trajectory. The knowledge gained from this work justified the variable displacement pump to be changed to a fixed displacement pump, further reducing cost and complexity of the system. This work also provided insight into how chamber volume and maximum pump flow rate affect system cost.

2. The integration of a flow intensifier into the compression/expansion chamber itself produced a novel design approach. This design approach was also optimized for cost using additional design parameters necessary to describe the new system concept. The introduction of the flow intensifier provided an *improvement* to system power density while *reducing* system cost when compared to the power density optimized case without the flow intensifier. System design variables were acquired and documented for future prototype production.

The other research thrust of this thesis focused on the inverted liquid piston compressor (ILPC), the first stage compressor of the system. Breaking up the compression into two stages provides advantages to system efficiency since the gas would show less temperature rise when compared to a single compression stroke. Since the first stage compression ratio is a fraction of the second stage compression ratio, this provided the opportunity to compress the gas quickly. By inverting the liquid piston, all the positive heat transfer benefits of the conventional liquid piston can be achieved while

keeping the denser fluid stationary. Keeping the denser fluid stationary is important for the stability of the liquid-air interface. It has been shown that the acceleration of the denser fluid is the primary cause of interface instabilities. However, the introduction of porous media inside of the ILPC chamber creates many moving boundary conditions to transfer momentum to the fluid thus creating instabilities. The work conducted in this thesis aimed to provide insight into the cross plate heat exchanger geometry's (porous media) effects on liquid-air interface stability. The main contributions in this area achieved in this thesis are summarized below:

1. A two-dimensional liquid-air interface CFD model was developed and used to simulate interface motion. The model was used to determine a relationship between plate separation distance of the porous media insert and liquid-air interface wave amplitude. The model also was used to determine the relationship between interface wave amplitude and operating frequency of the ILPC.

2. Experiments were conducted with rapid prototyped porous media inserts of varying plate separation distances. These inserts were attached to a prototype ILPC and high speed footage of the liquid-air interface was recorded. Edge tracking software was produced and used to track the amplitude of the interface during operation and calculate average maximum amplitude for consecutive cycles. Experiments agreed with simulations showing a decrease in wave amplitude with increasing plate separation distances and an increase in amplitude with an increase in operating frequencies.

5.2 Recommendations for Future Work

Further investigation is needed on many fronts for the continuation of this project. Primarily, the general mechanical design of the prototype compressor/expander with integrated flow intensifier produced in this thesis must be fleshed out with detail design. Once detail design is complete, fabrication of an experimental prototype system can begin. The resulting compressor/expander can be used to verify simulation predicted

results. This step is crucial to proceeding towards commercialization, as it will show a functioning scaled system of the novel CAES system presented in this thesis. Further commercialization strategies target carbon dioxide sequestration as a possible application of this system. Therefore, simulating and testing CO2 compression cycles is of great interest. CO2 is not an ideal gas, therefore the modeling methods used in this thesis must be modified to handle such gases.

References

[1] “Inventory of U.S. Greenhouse Gas Emissions and Sinks: 1990-2017,” Environmental Protection Agency, 2012. Available at: https://www.epa.gov/ghgemissions/draft-inventory-us-greenhouse-gas-emissions-and-sinks-1990-2017

[2] K. Palmer, A. Paul, and M. Woerman, “The Variability of Potential Revenue from a Tax on Carbon," Considering Carbon Tax (Resources for the Future), May 2012. Available at: https://www.rff.org/publications/issue-briefs/the-variability-of-potential-revenue-from-a-tax-on-carbon/

[3] K. M. Powell, J. D. Hedengren, T. F. Edgar, “Dynamic optimization of a solar thermal energy storage system over a 24 hour period using weather forecasts," Proceedings of the American Control Conference, Washington, USA, June 2013.

[4] C. Jaworsky and K.Turitsyn, “Effect of Storage Characteristics on Wind Intermittency Mitigation Effectiveness," Proceedings of the American Control Conference, pp. 3655-3660, Washington, USA, June 2013.

[5] H. M. Kim, J. Rutqvist, D.W. Ryu, B. H. Choi, C. Sunwoo, W. K. Song, “Exploring the concept of compressed air energy storage (CAES) in lined rock caverns at shallow depth: a modeling study of air tightness and energy balance," Applied Energy, Vol. *92, pp. 653-667, 2012.*

[6] M. Raju, S.K. Khaitan, “Modeling and simulation of compressed air storage in caverns: a case study of the Huntorf plan," Applied Energy, Vol. 89, pp. 474-481, 2012.

[7] P. Y. Li, E. Loth, T. Simon, J. D. Van de Ven and S. D. Crane, “Compressed Air Energy Storage for Offshore Wind Turbines," International Fluid Power Exposition, *Las Vegas, USA, March 2011.*

[8] F. D. Gonzleza, A. Sumpera, O. G. Bellmunta, R. V. Roblesb, “A Review of Energy Storage Technologies for Wind Power Applications," Renewable and Sustainable *Energy Reviews, Vol. 16, pp. 2154-2171, 2012.*

[9] Saadat M. (2016). “Modeling, Control and Optimization of a Novel Compressed Air Energy Storage System for Off-Shore Wind Turbines”. Phd Dissertation. University of Minnesota. Minneapolis, MN.

[10] P. Y. Li, J. D. Van de Ven, C. Sancken, “Open Accumulator Concept for Compact Fluid Power Energy Storage," Proceedings of the ASME International Mechanical *Engineering Congress, Seattle, USA, November 2007.*

[11] J. D. Van de Ven, P. Y. Li, “Liquid piston gas compression," Applied Energy, Vol. *86, pp. 2183-2191, 2009.*

[12] M. Sozen, T. M. Kuzay, “Enhanced heat transfer in round tubes with porous inserts," International Journal of Heat Fluid Flow, Vol. 17, pp. 124-129, 1996.

[13] C. Zhang, T. W. Simon, P. Y. Li, “Optimization of the axial porosity distribution of porous inserts in a liquid piston gas compressor using a one-dimensional formulation," *International Mechanical Engineering Congress and Exposition, San Diego, USA, November 2013.*

[14] C. J. Yang and R. B. Jackson, “Opportunities and barriers to pumped-hydro energy storage," Renewable & Sustainable Energy Reviews, Elsevier, pp. 839-844, 2011.

[15] S. Rehmana, L. M. Al-Hadhramia, M. M. Alam, “Pumped hydro energy storage system: A technological review," Renewable and Sustainable Energy Reviews, Vol. *44, pp. 586-598, April 2015.*

[16] “Global Energy Storage Database," United States Department of Energy, DOE, *2019. Available: http://www.energystorageexchange.org/*

[17] Moran, M. J., Shapiro, H.N., Fundamentals of Engineering Thermodynamics, 5th edition

[18] West, C. D., Liquid Piston Stirling Engine, Van Nostrand Reinhold Company Inc., New York

[19] G. F. Hohenberg, "Advanced Approaches for Heat Transfer Calculations," Diesel Enginer Thermal Load, pp. 61-79, 1979.

[20] A. Mohammadi, M. Yaghoubi and M. Rashidi, "Analysis of Local Convective Heat Transfer in a Spark Ignition Engine," International Communications in Heat and Mass Transfer, vol. 35, pp. 215-224, 2008.

[21] E. L. Pereira, C. J. Deschamps and F. A. Ribas, "Numerical Analysis of Heat Transfer inside the Cylinder of Reciprocating Compressors in the Presence of Suction and Discharge Processes," in International Compressor Engineering Conference at Purdue, West Lafayette, IN, 2010.

[22] U. Lekic and B. W. Kok, "Heat Transfer and Fluid Flows in Gas Springs," The Open Thermodynamics Journal, vol. 4, pp. 13-26, 2010.

[23] Joyce, N.G., Humphrey Pump - Internal Combustion Pump, Conference of Small Engines and Their Fuels In Developing Countries, p 31-44, Sept 1984

[24] M. Niikanjam and R. Greif, "Heat Transfer during Piston Compression," Journal of Heat Transfer, vol. 100, pp. 527-530, 1978.

[25] R. Grief, T. Namba and M. Nikanjam, "Heat Transfer during Piston Compression Inclusing Side Wall and Convective Effects," International Journal of Heat and Mass Transfer, vol. 22, pp. 901-907, 1978.

[26] J. Polman, "Heat Transfer in a Piston-Cylinder System," International Journal of Heat and Mass Transfer, pp. 184-187, 1980.

[27] D. R. Buttsworth, "Heat Transfer during Transient Compression: Measurements and Simulations," Shock Waves, vol. 12, no. 1, pp. 87-91, 2002.

[28] W. Hirt and B. D. Nichols, "Volume of Fluid (VOF) Method for Dynamics of Free Boundaries," Journal of Computational Physics, vol. 39, pp. 201-225, 1981.

[29] M. Isshii, Thermo-Fluid Dynamic Theory of Two-Phase Flow, Paris: Eyrolles, 1975.

[30] Rice, A. T., Li, P. Y., & Sanckens, C. J. (2017). “Optimal Efficiency-Power Tradeoff for an Air Compressor/Expander” Journal of Dynamic Systems, Measurement, and Control, 140(2), 021011.

[31] Zhang, Chao & Shirazi, Farzad & Yan, Bo & Simon, Terrence & Li, Perry & Van de Ven, James. (2013). “Design of an Interrupted-Plate Heat Exchanger Used in a Liquid-Piston Compression Chamber for Compressed Air Energy Storage” 10.1115/HT2013-17484.

[32] Zhang, Chao & Simon, Terrence & Li, Perry. (2013). “Optimization of the Axial Porosity Distribution of Porous Inserts in a Liquid-Piston Gas Compressor Using a One-Dimensional Formulation” ASME International Mechanical Engineering Congress and Exposition, Proceedings (IMECE). 8. 10.1115/IMECE2013-63862.

[33] Taylor, G, “The Instability of Liquid Surfaces when Accelerated in a Direction Perpendicular to their Planes. I,” Proceedings of the Royal Society of London. Series A, Mathematical and Physical Sciences, Vol. 201, No. 1065, 1950, pp. 192-196.

[34] Lewis, D.J., “The Instability of Liquid Surfaces when Accelerated in a Direction Perpendicular to their Planes. II,” Proceedings of the Royal Society of London. Series A, Mathematical and Physical Sciences, Vol. 202, No. 1068, 1950, pp. 81-96.

[35] Valha, J. and Kubie, J., “Stability of a gas-liquid interface in a periodic vertical motion,” Chemical Engineering Science, Volume 51, Issue 22, November 1996, Pages 4997-5006

[36] B. Yan et al. “Experimental Study of Heat Transfer Enhancement in a Liquid Piston Compressor/Expander Using Porous Media Inserts”. In: Applied Energy 154 (2015), pp. 40–50.

[37] J.D. Lewins. “Optimizing an Intercooled Compressor for an Ideal Gas Model”. International Journal of Mechanical Engineering Education 31.3 (2003), pp. 189–200.

[38] J. D. Van de Ven, P. Gagnon, and M. Saadat. 2017. “Inverted Liquid Piston Compressor/Expander”. US Patent 20170002803A1. Filed June 30, 2016, and issued in January 5, 2017.

[39] A. Nakayama, F. Kuwahara and T. Umemoto, "Heat and Fluid Flow within an Anisotropic Porous Medium," Transactions of ASME, vol. 124, pp. 746-753, Aug. 2002.

[40] F. L. Dullien, Porous Media: Fluid Transport and Pore Structure, Academic Press, 1979.

[41] R. J. Tabaczynski, D. P. Hoult and J. C. Keck, "High Reynolds Number Flow in a Moving Corner," Journal of Fluid Mechanics, vol. 42, pp. 249-255, 1970.

[42] E. W. Lemmon, R. T. Jacobsen, S. G. Penoncello, D. G. Friend, “Thermodynamic properties of air and mixtures of nitrogen, argon, and oxygen from 60 to 2000 K at pressures to 2000 MPa,” Journal of Physical and Chemical Reference Data, Vol. 29, pp. 331-385, April 2000.

[43] Saadat, Mohsen & Li, Perry. (2016). “An approach to reduce the flow requirement for a liquid piston air compressor/expander in a compressed air energy storage system”, IET Renewable Power Generation.

[44] Barzilai, J. (1988). Two-Point Step Size Gradient Methods. IMA Journal of Numerical Analysis, 141–148.

[45] Wong L.K. 2011. “Computational fluid dynamics analysis on the liquid piston gas compression”, Master’s Thesis. University of Minnesota. Minneapolis, MN.

[46] Brooks R. 2017. “Liquid-gas interface stability in inverted liquid piston air compressor” Undergraduate Honor’s Thesis. University of Minnesota. Minneapolis, MN.

[47] McKee, S., Tome, M.F., and Ferreira, V.G. 2007. “The MAC method”. Computers & Fluids, Vol. 37, October 2007.

[48] Norton, R. L. (2012). Design of machinery: An introduction to the synthesis and analysis of mechanisms and machines. New York: McGraw-Hill.

[49] Kundu, P. K., Cohen, I. M., & Hu, H. H. (2004). Fluid mechanics. 6th Edition.

[50] Tryggvason, G. 2013. “A code for the Navier-Stokes equations in velocity/pressure form”. Retrieved from Notre Dame, Computation Fluid Dynamics course.

[51] Srivatsa, A., Li, P. Y. (2018). “How Moisture Content Affects the Performance of a Liquid Piston Air Compressor/Expander”. Journal of Energy Storage 18 (2018) 121-132.

[52] Qin, C., Loth, E., Li, P., Simon, T., Van de Ven, J., Crane, S., and Pourmousa, A., 2013, “Spray-Cooling for Wind-Based Compressed Air Energy Storage,” 49th AIAA/ASME/SAE/ASEE Joint Propulsion Conference & Exhibit and 11th International Energy Conversion Engineering Conference, San Jose, CA, July 2013.

[53] C. Zhang, B. Yan, J. Wierberdink, P. Y. Li, J. D. Van de Ven, E. Loth, T. W. Simon, “Thermal analysis of a compressor for application to compressed air energy storage”, Applied Thermal Energy 73 (2) (2014) 1402– 1411.

[54] S. Boyd and L. Vandenberghe, “Convex Optimization,” Cambridge University Press, U.K., 2004

[55] Patil, Vikram; Acharya, Pinaki; and Ro, Paul, "Experimental Investigation of Aqueous Foam based Heat Transfer in Liquid Piston Compressor for Improvement in Compression Efficiency" (2018). International Compressor Engineering Conference. Paper 2636.

[56] F. D. Gonzleza, A. Sumpera, O. G. Bellmunta, R. V. Roblesb, “A Review of Energy Storage Technologies for Wind Power Applications,” Renewable and Sustainable Energy Reviews, Vol. 16, pp. 2154-2171, 2012.

[57] M. Saadat, A. Srivatsa, P. Y. Li and T. W. Simon, "Air Compression Performance Improvement Via Trajectory Optimization: Experimental Validation", ASME DSC Conference [DSCC2016-9825], Minneapolis, MN, October, 2016.

[58] Rice A. (2011). “Heat transfer enhancement in a cylindrical compression chamber by way of porous inserts and the optimization of compression and expansion trajectories for varying heat transfer capabilities”. MS Thesis. University of Minnesota. Minneapolis, MN.

[59] Wieberdink J. (2014). “Increasing efficiency and power density of a liquid piston air compressor / expander with porous media heat transfer elements”. MS Thesis. University of Minnesota. Minneapolis, MN.

[60] “Global Composite Steel Price and Index (USD/tonne)," MEPS International Ltd., 2018. *Available: https://worldsteelprices.com/*

[61] “Global Market Forecast of ABS Material” Plastic Insight, *2019. Available: https://www.plasticsinsight.com/resin-intelligence/resin-prices/abs-plastic/*

[62] M. Saadat and P. Y. Li, ″Combined Optimal Design and Control of a Near-isothermal Liquid Piston Air Compressor/Expander for a Compressed Air Energy

Storage (CAES) System for Wind Turbines", 2015 ASME-DSCC, Columbus, OH., October, 2015.